December 2014

Laboratory Studies of Gas-Grain Processes on Cosmic Dust Analogues

Jiao He
Syracuse University

Recommended Citation

He, Jiao, "Laboratory Studies of Gas-Grain Processes on Cosmic Dust Analogues" (2014). *Dissertations - ALL*. 195.
https://surface.syr.edu/etd/195

Abstract

The formation of molecules in the interstellar medium (ISM) takes place both in the gas phase and on surfaces of cosmic dust grains. Gas phase reactions alone are found to be insufficient to account for the observed abundance of molecules such as molecular hydrogen, water, carbon dioxide, methanol as well as many other complex molecules; grain surfaces must be involved as catalysts to explain their formation. In this thesis we study the physical and chemical processes on surfaces of cosmic dust grain analogues in simulated ISM environments. Oxygen is the third most abundant element in the universe and is present in many astrobiologically important molecules. The desorption energy of atomic oxygen is a fundamental parameter that enters ISM models because it controls the residence time of this atom on a surface. However, it has not been measured in the laboratory. In this thesis, this parameter is measured by using both an indirect and a direct method. The measured value agrees with model predictions based on astronomical observations. The formation of two oxygen-containing molecules, water and hydroxylamine, is studied next. Water is the main component of ice mantles in dense clouds and is indispensable for the origin of life. Its formation via ozone hydrogenation on an analog of a warm dust grain is studied experimentally. The desorption energy of an important intermediate product in the reaction, the OH radical, is also inferred. Hydroxylamine is a precursor to the formation of glycine, which is the simplest amino acid. The formation of hydroxylamine via the oxidation of ammonia is studied by sequential deposition of ammonia and atomic oxygen and is followed by temperature programmed desorption experiments. The measured high reaction efficiency predicts that ammonia oxidation on grain surfaces could be an important route to hydroxylamine formation. The last chapter of this thesis introduces a rate equation model to simulate surface kinetics, including diffusion and desorption, of atoms and molecules on non-uniform surfaces.

Laboratory Studies of Gas-Grain Processes on Cosmic Dust Analogues

by

Jiao He

B.S., Nanjing University 2009

DISSERTATION

Submitted in partial fulfillment of the requirements for the
degree of Doctor of Philosophy in Physics
in the Graduate School of Syracuse University

December 2014

To my parents

Acknowledgments

First and foremost, I would like to express my appreciation to my thesis advisor, Professor Gianfranco Vidali. He is a knowledgeable scientist who has a deep understanding of both the details of scientific instrumentation and the big picture of astronomy. He is patient enough to teach me how each component of the apparatus works, and insightful enough to find the most promising project for me to work on. Whenever I encountered problems in the lab he is always ready to offer help and suggestions. What I learned from him will benefit me for the rest of my scientific career.

My thanks also go to my lab-mates. Paul and DJ taught me the experimental skills and helped me to carry out measurements. I learned a lot from them. I wish to thank Jianming and Zhirou, for taking over some of the overnight experiments. Without their help I wouldn't have accompanied so much just near my graduation. Zhirou, wish you good luck in the graduate school application. Tyler, thanks for proof-reading my thesis draft and fixing the language problems. You have been my best non-Chinese friend in SU.

I also thank the physics machine shop for helping me with countless technical problems. Lou, Charlie, Lester, and Phil, they are all very nice to work with, and really helpful. Shortly after I moved to University of Hawaii, I started to miss the SU physics machine shop. I also wish to thank Patricia Whitmore, Cindy, Penny and other staff of the physics department, for their administrative support.

In SU physics, I had a lot of good friends. Liu Jiaming, Chen Yu, Ma Xu, Chen Huangye, Cao Liang, Zhao Hui, Gui Bin, Xu Shiliyang, Xiao Bo, Song Chunhua, Hao Yu, Wan Duanduan, Zhang Tao, Jiang Wei (list not complete), life at SU physics has been more enjoyable with you.

I also wish to thank my thesis committee for taking the time to read the draft carefully and suggesting improvements. Thank Prof. LaHaye for writing recommendation letters for my job application.

Finally, I would like to thank my family. My parents, grandparents, and sister supported me to study abroad and are always proud of me, encouraging me to pursue my goal. Thanks to Kai for being with me all these years when I was working toward my PhD, for the love and support.

Contents

1 Introduction 1

1.1 The origin of life on Earth 1
1.2 Molecules in the interstellar medium 2
1.3 Classification of interstellar clouds 4
1.4 Gas phase reactions 5
1.5 The role of cosmic dust 8
1.6 Important physicochemical processes on grain surfaces 10
1.7 Rate equation model 14
1.8 This thesis 15

2 Experimental 17

2.1 Overview 17
2.2 Main chamber 17
2.3 Molecular beam 21
2.4 TPD experiments 27

3 Atomic Oxygen Desorption from Dust Grain Surfaces 30

3.1 Introduction 31
3.2 Indirect measurement of O desorption energy 35
  3.2.1 Experimental 35
  3.2.2 Results and analysis 38

3.3 Direct measurement of O desorption energy 47
    3.3.1 Experimental 47
    3.3.2 Results and analysis 49
3.4 Conclusions 53

4 Water Formation on Warm Dust Grains 55

4.1 Introduction 56
4.2 Experimental 59
4.3 Results 60
4.4 Analysis and discussion 62
    4.4.1 H/D gas-grain reaction mechanism 62
    4.4.2 Water formation and OH/OD desorption 64
4.5 Astrophysical implications 69

5 Formation of Hydroxylamine on Dust Grains via Ammonia Oxidation 71

5.1 Introduction 71
5.2 Experimental 73
    5.2.1 Beam flux calibration 73
    5.2.2 Experimental procedures 75
5.3 Results and analysis 77
    5.3.1 Multilayer NH_3 + O 77
    5.3.2 Submomolayer NH_3 + O 79
    5.3.3 Reaction efficiency of NH_3 + O 80
    5.3.4 Control experiments 82
5.4 Discussions 82
5.5 Conclusions 84

6 Diffusion-Desorption Rate Equation Model 85

6.1 Introduction 86

6.2 Rate equation model 89

6.3 The diffusion-desorption rate equation model 91

6.4 Simulations and discussion 94

  6.4.1 CO on MgO(100) 94

  6.4.2 H_2/D_2 adsorption-desorption 99

  6.4.3 HD on an amorphous silicate 101

  6.4.4 Limitations and suggestions for experimental investigations 102

6.5 Conclusions 103

List of Figures

1.1 A schematic showing the formation of molecular hydrogen on a dust grain. . . 10

1.2 Schematics illustrating the three mechanisms of reactions on the surface, i.e., Eley-Rideal (ER), hot atom (HA) and Langmuir-Hinshelwood (LH) mechanisms. 13

2.1 A schematic of the main apparatus. 18

2.2 Top view of the QMS, the cone and the sample, in both exposure stage and TPD stage. 19

2.3 A drawing of the radio frequency dissociation source. 22

2.4 QMS measured beam counts versus gas flow for NH_3, O_2, D_2, He. In measuring NH_3 beam, there are both mass 17 amu and mass 16 amu, where mass 16 amu is due to the fragmentation of NH_3 in the ionizer. 22

2.5 A schematic of the direct beam measurement using MCS and chopper. . . . 24

2.6 MCS recorded spectra of H_2 with RF on and RF off. The H_2 gas flow is 0.3 sccm. 25

2.7 Dissociation rate for O_2, H_2, and D_2 at different gas flow rate. 26

2.8 Measured time delays between the photodiode signal and the MCS peak versus the inverse of chopper frequency for both molecular oxygen and atomic oxygen. The parameters for a linear fitting are also included in the figure. 27

2.9 Schematic of a TPD experiment. In the exposure stage of a TPD experiment, sample surface stays at low temperature and atoms/molecules are sent to the sample. In the TPD stage, the sample surface is heated up to thermally desorb atoms/molecules from the surface, and a desorption peak shows up in the mass spectrometer signal. 29

2.10 CO_2 adsorption-desorption TPD experiments on an amorphous silicate surface. During exposure stages, the CO_2 gas flow was 0.3 sccm. The exposure durations were 0.5 minute, 1 minute, 1.5 minutes, 2 minutes, 2.5 minutes, 3 minutes, and 4 minutes, respectively. The surface temperature during exposure was 50 K; the heating ramp rate during the TPD stage was 1 K/s. 29

3.1 Adsorption-desorption of O_2 from an amorphous silicate surface kept at 20 K for different coverages. The heating ramp rate during the TPD stage is about 1 K/sec. 37

3.2 Distribution of E_{des} for O_2 on an amorphous silicate surface obtained from direct inversion of TPD data shown in Figure 3.1. 40

3.3 TPD traces of O_2 and O_3 after O/O_2 exposure for the indicated times; the surface temperatures during exposure are 30 K, 40 K and 50 K. 42

3.4 TPD traces of mass 16, 32, 48 amu after depositing 8 minute O/O_2 at 48 K on porous amorphous water ice. The heating ramp is 10 K/minute. The dashed line shows a fitting of the mass 16 amu peak using $E_{\mathrm{des}}(\mathrm{O}) = 1660$ K (see text). 49

3.5 TPD traces of 16, 32, 48 amu after depositing 8 minutes of O/O_2 at 48K on an amorphous silicate that has been pre-coated with 0.2 ML of ozone.The heating ramp is 30 K/minute. The inset shows the temperature ramp. 51

3.6 TPD traces of mass 16 amu (blue) and mass 48 amu (green) after deposition of 0 minute, 4 minutes, and 8 minutes of O/O_2 on 0.2 ML, 0.4 ML, 0.6 ML, and 0.8 ML of O_3 pre-coated amorphous silicate. The heating ramp is 0.5 K s^{-1}. The top row of each panel has the original TPD traces while in the bottom row the contribution of O_3^+ fragmentation to the signal of mass 16 amu has been subtracted. 52

3.7 Fitting of the mass 16 amu TPD traces after subtraction in the top-right panel (4 min O_3 + 0, 4, 8 min O) of Figure 3.6 using $E_{\mathrm{des}} = 1850$ K. 53

4.1 A schematic of the water formation routes on grain surfaces. 57

4.2 Illustration of a typical experimental procedure. The temperature curve is taken from a typical experiment of ozone hydrogenation. In the first stage (T = 30 K) the sample surface is exposed to $^{18}O/^{18}O_2$ beam for 20 minutes. In the second stage the sample is kept at 50 K for 2 minutes with no beam exposure to desorb the residual $^{18}O_2$. In the third stage the sample is cooled down to below 30 K in order to obtain a reproducible heating ramp rate. The last stage is the TPD stage in which the sample is heated up to about 190 K. 61

4.3 A typical TPD spectrum after $^{18}O_3$+D sequential deposition as illustrated in Figure 4.2. Masses 20, 21, 22, and 36 amu are OD, HDO, D_2O, and O_2 (ozone fragmentation) respectively. The surface temperature during D deposition was 50 K. 63

4.4 TPD yields of masses 19, 20, and 36 amu for $^{18}O_3$+H sequential deposition experiments as illustrated in Figure 4.2. The H exposure lengths were 0 min, 4 min, 8 min, 12 min, 16 min, 24 min, 32 min, and 48 min, respectively. The surface temperature during H deposition was 50 K. 64

4.5 Log scale plot of TPD yields of masses 20, 21, 22 and 36 amu for sequential deposition experiments ${}^{18}O_3$+D as illustrated in Figure 4.2. The D exposure lengths are 0 min, 5 min, 10 min, 15 min, 20 min, 30 min, 45 min, 60 min, 75 min, and 90 min, respectively. The mass 20 amu contribution from the beam line ($D_2\,{}^{16}O$) has already been subtracted from the yields, although there is still some contamination from the vacuum chamber background, as can be seen from the fact that the mass 20 amu trace does not start from 0. 65

4.6 Log plot of the ozone (mass 36 amu) TPD yields as a function of H/D exposure time. The two straight lines show linear fits. 66

5.1 TPDs with different exposure of NH_3 at 70 K. The exposure times are from bottom to top, 0.5, 1, 2, 4, and 8 minutes, respectively. The desorption energy distribution of NH_3 calculated from the 2 minutes exposure curve (1 ML deposition) is in the inset. 75

5.2 A typical TPD of a NH_3 + O sequential exposure experiment at 70 K in which the QMS records simultaneously multiple signals. The temperature ramp (black line) shows that after the exposure is terminated, the sample is cooled to 40 K before the heating is started. 76

5.3 Mass 17 QMS signal of the TPD from an ice consisting of NH_3 (4 minutes) followed by exposure to various doses of O at 70 K. 78

5.4 QMS mass 33 amu signal of the TPD from an ice consisting of NH_3 (4 minutes) followed by various doses of O at 70 K. 79

5.5 QMS signal of the TPD from 2 ML of NH_3 + 8 (left) and 16 (right) minutes of O exposure. 80

5.6 Mass 16 QMS signal in the TPD from a deposit of NH_3 (0.5 minute) + various doses of O at 70 K. 81

5.7 Integrated TPD signs mass 16 amu from a deposit of NH_3 (0.5 minutes or 1/4 of a ML) + various exposures of O at 70 K. 82

5.8 Mass 33 QMS signal in the TPD from NH_3 + O_2 and O_3 + NH_3 deposited at 70 K compared with that of NH_3 + O at 50 K. Curves are offset for clarity. . 83

6.1 Diagram of surface adsorption sites and transition states. 93
6.2 CO TPD spectra for monolayer and submonolayer coverages of CO/MgO(100) (θ = 0.09, 0.16, 0.23, 0.32, 0.42, 0.48, 0.58, 0.71, 0.90, 1.00, 1.14, 1.27). Replotted from Dohnálek et al. (2001). 95
6.3 Desorption energy barrier distribution for CO on MgO(100) obtained using data of Dohnálek et al. (2001) 96
6.4 Simulation of TPD spectra for different initial coverages using the desorption energy distribution obtained from direct inversion of CO on MgO(100) TPD spectra of Dohnálek et al. (2001), see Figure 6.3. 97
6.5 Fractional occupation of adsorption sites at different temperatures: 22 K, 40 K, 45 K, 50 K, 55 K, 60 K, 65 K, 70 K and 75 K. No desorption is assumed and only the diffusion process is simulated. The initial coverage and ΔE are 0.3 ML and 30 meV, respectively. As the temperature increases, molecules move from shallow adsorption sites to deeper ones. 98
6.6 Simulation of Dohnálek et al. (2001) experimental data using different ΔE values, based on the diffusion-desorption rate equation model. The experimental data are shown in the first panel. 99
6.7 TPD spectra for D_2 adsorption-desorption from non-porous amorphous water ice; the surface temperature during exposure with D_2 is 10 K. Data from Amiaud et al. (2007) 101
6.8 Two model desorption energy distribution sharing the same tail. 102
6.9 Simulated TPD spectra using the desorption energy distribution #1 in Figure 6.8 103
6.10 Simulated TPD spectra using the desorption energy distribution #2 in Figure 6.8 103

6.11 HD desorption from amorphous silicate ($FeMgSiO_4$) surface. The exposure doses are 30 sec, 1 minute, 2 minutes, 4 minutes and 8 minutes. The surface temperature during exposure with HD is 10.5 K. 104

6.12 HD desorption energy distribution obtained from direct inversion of the TPD spectra in Figure 6.11. 104

List of Tables

1.1 Approximate cosmic abundances of some elements normalized to hydrogen. Table adapted from Hama & Watanabe (2013) 3

1.2 Gas phase molecular abundances in Taurus Molecular Cloud-1, normalized to H_2 Table adapted from Hama & Watanabe (2013) with an updated value for O_2 (Hincelin et al., 2011) 3

3.1 Integration of TPD traces from Figure (3.3). The last row is the TPD yield ratios of mass 36 amu to mass 54 amu. 41

3.2 Calculation of O coverages $\theta(\mathrm{O})$ and O_2 coverages $\theta(\mathrm{O_2})$ at 30 K, 40 K, and 50 K, and of the O desorption energy $E^{\mathrm{O}}_{\mathrm{des}}$, assuming different α values. The units for coverages and desorption/diffusion energies are ML and meV respectively. 43

3.3 Desorption energy of atomic oxygen from porous amorphous water ice and from an amorphous silicate surface. 53

4.1 Masses recorded for given experiments. In the column "Origin", the source of the molecule is indicated; "frag." indicates it comes from fragmentation in the QMS ionizer. The oxygen isotope ^{18}O was used unless specified. In the origin of mass 21(OD+H_2), the H_2 is from the vacuum background. 62

Chapter 1

Introduction

1.1 The origin of life on Earth

The quest to find the origin of life has attracted tremendous attention in both the scientific community and the general public. Biologically relevant macromolecules, such as proteins, sugars, fats, DNA, and RNA, all assemble from fundamental building blocks such as amino acids, monosaccharides, and glycerol. One of the most important steps towards unraveling the origin of life is to find out the prebiotic origin of these molecules. Concerning the origin of prebiotic molecules there are two leading hypotheses. One is called "Primordial Soup Theory" that was proposed by Alexander Oparin in the 1920s and later on experimentally studied by Harold Urey and Stanley Miller in the 1950s (Miller, 1953). The other hypothesis is called the panspermia hypothesis; it proposes that prebiotic molecules as well as other organic molecules came from extraterrestial sources, such as the infall of meteorites, comets, and interplanetary dust particles (Brack, 1999). This hypothesis is supported by an analysis of the Murchison meteorite which fell in Australia in 1969 (Glavin & Bada, 2001; Cooper et al., 2001). The meteorite was found to contain 19 of the 20 amino acids used in living organics, several sugars along with other complex organic molecules. The history of comets, meteorites, and interplanetary dust particles can be further traced back to the protoplanetary disk when the Solar System was formed. In reality, complex organic molecules are observed in protoplanetary disks and star-forming regions. To date, nearly 180 molecular species have been confirmed in the interstellar space and most of them are complex organic molecules. Reactions in the gas phase are successful in explaining the formation of some molecular species, but many of them can not be explained by gas phase reactions alone. They are believed to be formed on the surface of some tiny particles—cosmic dust (Herbst & van Dishoeck, 2009; Tielens, 2013). Therefore, the physical and chemical processes happening on cosmic dust grain surfaces and the interplay of gas phase and grain-surface reactions are the keys to explaining the origin of prebiotic molecules.

1.2 Molecules in the interstellar medium

Interstellar space is not empty, but instead it is occupied by a sparse ensemble of atoms, molecules, and tiny dust particles (see Section 1.5). The elemental composition of the interstellar medium (ISM) is assumed to be very similar to the Sun's, with some corrections (Jenkins, 2009). Table 1.1 shows the abundances of the most abundant elements. It is worth mentioning that oxygen is the third most abundant element; it plays a fundamental role in astrochemistry. Chapter 3 studies the kinetics of atomic oxygen on grain surface analogues.

The first molecules found in the ISM were CH and CN radicals (Swings & Rosenfeld, 1937; McKellar, 1940), and were detected via their electronic transitions in the visible wavelength range by ground based telescopes. These findings were revolutionary, since they were in contradiction to the beliefs of traditional chemistry. In the ISM, even the most dense regions have a gas density typically of 10^8 cm^{-3}, which is still 11 orders of magnitude lower than the molecular density at sea level on Earth ($\sim 10^{19}$ cm^{-3}). In addition, the ISM is under extremely harsh conditions such as ultra-low temperature, ultraviolet (UV) light irradiation, and cosmic ray irradiation. Traditional chemistry would predict that almost no molecules would form in the ISM (van Dishoeck, 2014). However, observational results showed the

H	1
He	1×10^{-1}
O	5×10^{-4}
C	2×10^{-4}
N	7×10^{-5}
Fe	3×10^{-5}
Mg	3×10^{-5}
Si	2×10^{-5}
S	1×10^{-5}
Ca	2×10^{-6}
Ni	1×10^{-6}

Table 1.1: Approximate cosmic abundances of some elements normalized to hydrogen. Table adapted from Hama & Watanabe (2013)

H_2	1
CO	8×10^{-5}
OH	3×10^{-7}
H_2O	$< 7 \times 10^{-8}$
O_2	$< 3.9 \times 10^{-8}$
C_2	5×10^{-8}
CN	3×10^{-8}
CH	2×10^{-8}
C_4H	2×10^{-8}
NH_3	2×10^{-8}
H_2CO	2×10^{-8}

Table 1.2: Gas phase molecular abundances in Taurus Molecular Cloud-1, normalized to H_2 Table adapted from Hama & Watanabe (2013) with an updated value for O_2 (Hincelin et al., 2011)

opposite to be true. During the past few decades, thanks to the improved sensitivity of both ground and space based telescopes, nearly 180 molecular species have been confirmed to be in the ISM[1]. Table 1.2 lists the most abundant gas phase molecules in a dense cloud (TMC-1). These molecules are observed via their electronic, vibrational, and/or rotational transitions in the UV, visible, infrared, (sub)millimeter, and radio wavelengths. Among these ∼ 180 molecules, more than half are complex organic molecules(Herbst & van Dishoeck, 2009). They are found ubiquitously in the ISM, including dense molecular clouds, that are the birth place of stars, and protoplanetary disks, that are the origin of planetary systems. Among these detected molecules, some are of obvious astrobiological relevance. Glycolaldehyde, which is the simplest sugar molecule and an important precursor to RNA formation, has been detected in a protostellar core (Bacmann et al., 2012). The simplest amino acid glycine was claimed to have been detected (Kuan et al., 2003), however, a more recent analysis (Snyder et al., 2005) of the observational results does not support the conclusion by Kuan et al. (2003). One of the precursors to glycine is hydroxylamine, which has not been detected either. With the Atacama Large Millimeter Array (ALMA) telescopes, it should be possible

---

[1] A full list of ISM molecular species can be found at:
http://en.wikipedia.org/wiki/List_of_interstellar_and_circumstellar_molecules

to find glycine and hydroxylamine. Chapter 5 is devoted to the study of the formation of hydroxylamine in the ISM.

These observational results indicate the possibility that organic molecules, including the prebiotic molecules on Earth and in the Solar System, might have been formed in the ISM. How molecules are formed in the ISM depends on the physical condition of various interstellar clouds. The next section introduces the classification of interstellar clouds and describes their physical conditions.

1.3 Classification of interstellar clouds

Interstellar clouds can be classified into four main regions, namely, diffuse atomic clouds, diffuse molecular clouds, translucent clouds, and dense molecular clouds (Snow & McCall, 2006)[2]. In the simplest picture, interstellar clouds are assumed to have onion like structures (though in reality they are not spherical). The outer shell is a diffuse atomic cloud in which ultra-violet (UV) irradiation from nearby stars is only partly attenuated. The UV light breaks up molecular hydrogen into atomic hydrogen. Carbon is mostly ionized (C^+) because it has a lower ionization energy than hydrogen. Molecules in this region are few, because most molecules break up in the UV light. The next shell is called a diffuse molecular cloud in which UV irradiation is further attenuated. Molecular hydrogen begins to dominate over atomic hydrogen. In both diffuse atomic and diffuse molecular clouds, the gas density is lower than a few hundred per cm^3. Volatile molecules are in the gas phase; only molecules that bind strongly enough to a grain surface without being photodissociated/photodesorbed reside on the surface for a limited duration. In order for the abundance of a molecular species to be in steady state, the formation rate and destruction rate should be equal. This steady state assumption is the basis of some diffuse clouds models (e.g.,Glassgold & Langer (1974)).

---

[2] Note that the physical and chemical condition of interstellar clouds are not constant, instead, they are changing all the time. A cloud may span through all the four categories in its life time. In addition, there are no clear cut distinction between different clouds, the categorization is only a convenience for astronomical studies.

In diffuse molecular clouds, molecular hydrogen is destroyed mostly by photodissociation. However, how molecular hydrogen is formed in the diffuse molecular clouds is still under debate. Gas phase reactions alone are not sufficient to explain the observed abundances. Reactions on the cosmic dust grain surface have to contribute to the H_2 formation, though the mechanism is still unknown (Vidali, 2013). In the next shell, the translucent clouds, because of the self shielding of molecular hydrogen, UV light is attenuated to an extent that carbon is mostly in neutral atomic form. The inner-most cloud is a dense molecular cloud. A dense molecular cloud is sometimes called a dark cloud because this region is opaque to UV and visible light; it appears dark in visible light telescopes. Only radio waves and, to a lesser extent, infrared, can penetrate the dark clouds. Because of the lack of external energy sources, the dense molecular core is cold, with a typical gas temperature of 10-50 K. Cosmic rays are almost the only energy source available in dark clouds and drive a rich chemistry (see Section 1.4). Most nonvolatile molecules are condensed onto cosmic dust grain surfaces, forming ice mantles. The major component of ice mantles is water, which is detected in the absorption spectrum by the 3 μm band due to stretching of the O-H bond. Ice mantles provide a medium for the chemical enrichment of many space environments from dense clouds to protoplanetary disks (Kristensen & van Dishoeck, 2011; Hogerheijde et al., 2011). In Chapter 3 we study the desorption of atomic oxygen from a porous amorphous water ice and an amorphous silicate surface. In Chapter 4 we discuss how water is formed on grain surfaces.

1.4 Gas phase reactions

To study the formation and destruction rates of molecules in different regions of the ISM, both experimental measurements of reaction rates and quantitative modeling of chemical networks are required. In the earlier years of astrochemistry, only gas phase reactions were measured in the laboratory and included in astrochemical models; thus, much more is known about gas phase reactions than about grain surface processes. Pure gas phase models are successful in explaining the abundances of molecules such as CO, which after H_2, is the second most abundant molecule in the ISM. However, the gas phase route fails to account for the most abundant molecule, H_2, as well as for other important molecules such as water and methanol. As the element hydrogen is at least three orders of magnitude higher in abundance than other elements except for the inert element helium, hydrogen chemistry strongly affects the chemistry of all the other molecular species, either directly or indirectly.

In the gas phase, the neutral-neutral reaction

$$\mathrm{H} + \mathrm{H} \rightarrow \mathrm{H}_2 + h\nu \tag{1.1}$$

is not efficient because in this reaction the transition from the ${}^3\Sigma_u^+$ state to the ground state $X^1\Sigma_g^+$ is forbidden (Vidali, 2013). Another possible H_2 formation route is by ion-neutral reactions. The reactions start with

$$\mathrm{H} + e \rightarrow \mathrm{H}^- + h\nu \tag{1.2}$$

with a reaction rate

$$k = 10^{-18}\ T\ \mathrm{cm}^3\mathrm{s}^{-1} \tag{1.3}$$

where T is the gas temperature. The H^- ion then reacts with atomic hydrogen to form molecular hydrogen

$$\mathrm{H}^- + \mathrm{H} \rightarrow \mathrm{H}_2 + e \tag{1.4}$$

Based on this route, the formation rate of H_2 is not sufficient to account for the observed H_2 abundance because in molecular clouds the fraction of charged particles is low ($\sim 10^{-7}$). Thus, there must exist other more efficient formation routes, as discussed in the next section.

After H_2 and CO, OH and H_2O are the next most abundant molecules. Gas phase formation of OH and H_2O are initiated with the cosmic ray (c.r.) ionization of H_2:

$$H_2 + c.r. \rightarrow H_2^+ + e \tag{1.5}$$

H_2^+ then reacts with another H_2 to form H_3^+

$$H_2^+ + H_2 \rightarrow H_3^+ + H \tag{1.6}$$

In the gas phase, neutral-neutral reactions are much slower than their ion-neutral counterparts. Since in the ISM H_3^+ is after C^+ the second most abundant ion in molecular clouds, it plays an important role in gas phase chemistry. The reaction of H_3^+ with atomic oxygen leads to the following reactions:

$$O + H_3^+ \rightarrow H_2O^+ + H \tag{1.7}$$

$$H_2O^+ + H_2 \rightarrow H_3O^+ + H \tag{1.8}$$

$$H_3O^+ + e \rightarrow \begin{cases} H_2O + H \\ OH + H_2 \\ OH + 2H \\ O + H_2 + H \end{cases} \tag{1.9}$$

Both water and OH can be formed through this route. The bottleneck of this gas phase route is the fraction of H_3^+ ions and the density of electrons. Based on laboratory measurement of the rate constants and quantitative modeling, it is found that this route alone is insufficient to account for observed abundances of H_2O and OH (van Dishoeck et al., 2013). At a high gas temperature (> 300 K), neutral-neutral reactions start to dominate the water formation rate (van Dishoeck et al., 2013). But in the intermediate temperature range, it is still unclear via which mechanism water is formed. In Chapter 4 the water formation routes on warm grains are investigated.

Gas phase reactions are unable to account for the abundance of many molecules such as CO_2, CH_3OH, and other complex organic molecules (Tielens, 2013; Herbst & van Dishoeck, 2009). Alternative formation routes must be responsible for the chemistry in the ISM. It was found out that some tiny dust particles play an important role in the chemical evolution of the ISM. The next section discusses the role of cosmic dust.

1.5 The role of cosmic dust

Cosmic dust particles are ubiquitous, both in the solar system (called interplanetary dust), and in the ISM. Here we focus on cosmic dust in the ISM. The discovery of them began with Wilhelm Struve's analysis of star counts in the middle 17th century. Struve found that the apparent number of stars per unit volume decreases in all directions. He hypothesized that the star light is absorbed between stars. The existence of cosmic dust was not confirmed until the first half of the 20th century by Trumpler (1930a,b,c) and Stebbins et al. (1939) through analysis of the observed reddening of stars. Stebbins et al. (1939) found out that the dust particles absorbing the star light should have a dimension similar to the wavelength of visible light.

While cosmic dust samples in the solar system have already been collected and analyzed (Sandford & Walker, 1985), those from ISM are still unavailable so far. Tentative collection has been reported recently, but contraversy still exist concerning the origin of those particles (Westphal et al., 2014). Most information available about dust is obtained by remote observations using telescopes. A detailed analysis shows that the diameter of cosmic dusts can be as small as in the nanometer scale, and up to about one micrometer, with a size distribution following an empirical law $N_a \sim a^{-3.5}$, where a is the radius of the grain (Mathis et al., 1977). The temperature of dust is typically in the 10-20 K range in dense molecular clouds and 15-30 K in diffuse molecular clouds. The composition of dust is inferred indirectly from the depletion of heavy elements from the gas phase, and directly from infrared emission of the dust. There are two main types of dust, amorphous silicates that are formed in the outflows of oxygen-rich stars and carbonaceous particles, which are formed in the outflows of carbon-rich stars. Amorphous silicates are more abundant ($\sim 70\%$) than carbonaceous particles ($\sim 30\%$), therefore, in this thesis we use a sample of an amorphous silicate as an analog of the dust.

Although the dust contains only 1% of the total mass of the ISM and its number density is only 10^{-12} of hydrogen atoms, it plays an important role in the evolution of the ISM. Dust absorbs and scatters UV and visible light, and dissipates the energy away in form of infrared, thus affecting the overall thermal balance of the ISM. Dust also provides a place for atoms/molecules to accrete, diffuse and react, thus making a rich grain surface chemistry possible.

The importance of grain-surface reactions can be illustrated with the example of molecular hydrogen formation. A schematic is shown in Figure 1.1. A hydrogen atom hits the dust grain surface, and sticks to it (accretion). In thermally activated diffusion or tunneling, atomic hydrogen random walks on the surface. The diffusion rate depends both on surface temperature (in the case of thermal diffusion) and on the surface structure (in both thermal diffusion and tunneling). When a hydrogen atom meets another hydrogen atom, they form molecular hydrogen. The reaction rate on the grain surface increases significantly over gas phase reactions for two reasons: 1) The forbidden neutral-neutral gas-reaction H + H is allowed in the presence of a third body—the grain surface. 2) In the gas phase the density is low, and two hydrogen atoms have only one chance in the ample space to meet one another; it is a meet-or-lose scenario. However, on the grain surface, hydrogen atoms can be trapped for a long time and wait for the arrival of another hydrogen atom. Thus the reaction rate is enhanced significantly. After a hydrogen molecule is formed, it can desorb from the surface and go back to the gas phase. Other grain surface reactions work in a similar way. In the next section we discuss in more detail the important surface processes that take place on cosmic dust grains.

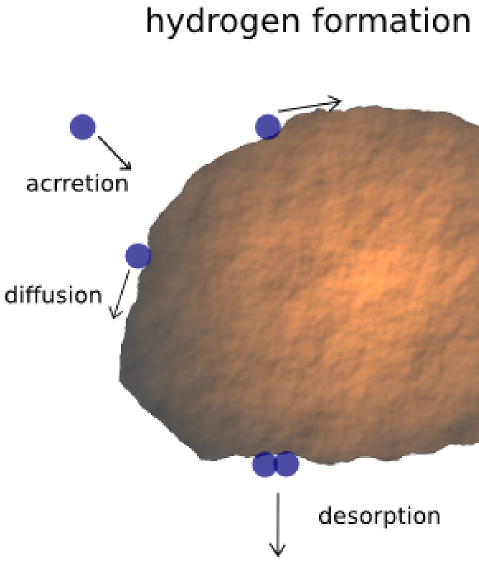

Figure 1.1: A schematic showing the formation of molecular hydrogen on a dust grain.

1.6 Important physicochemical processes on grain surfaces

Adsorption/desorption and diffusion are the two most important surface processes in the study of gas-grain chemistry. Adsorption is the process in which atoms/molecules (in the following we call them particles for convenience) land on and remain on the surface. The kinetic energy of the incoming particle is transferred to the grain surface. There is a binding energy between the incoming particle and the surface to keep the particle on the surface. The binding energy is equal to the desorption energy since this is also the energy required to desorb particles from the surface if the process is not activated. The strength of the binding energy depends on the interaction between the adsorbed particle and the underlying surface. In a typical gas-grain model, the surface provides a fixed number of adsorption sites to hold particles that land on it. The density of adsorption sites is usually taken to be 10^{15} cm^{-2}. For a non-uniform surface, the binding energies of the adsorption sites are not the same but instead differ for each site. In reality, the desorption energy should be a continuous distribution. We call the sites with a lower desorption energy the shallow sites and those with a higher desorption energy the deep sites. When the grain surface is heated up, adsorbed particles gain thermal energy from the underlying surface and may leave the surface (desorb). The probability of leaving the surface increases with the grain surface temperature and decreases with the desorption energy. Quantitatively, the desorption rate can be expressed by an Arrhenius type expression:

$$\frac{\mathrm{d}N(t)}{\mathrm{d}t} = -\nu N(t)\exp(-\frac{E_{\mathrm{des}}}{k_{\mathrm{B}}T}) \tag{1.10}$$

where $N(t)$ is the number of adsorbed particles on the surface at time t; ν is a prefactor, that is also called the attempting frequency. Though disagreement exists on the value of ν, in this thesis I adopt the most widely used value 10^{12} s^{-1} (Kolasinki, 2008). k_{B} is the Boltzmann constant; E_{des} is the desorption energy; T is the surface temperature. Based on the above expression, the residence time can be calculated as $\nu^{-1}\exp(E_{\mathrm{des}}/k_{\mathrm{B}}T)$. Since the desorption energy and the temperature are in the exponential term, small changes in temperature and/or desorption energy can significantly affect the residence time, thus affecting the relative number of particles on the grain surface compared with that in the gas phase. Because gas phase chemistry and grain surface chemistry are fundamentally different, the desorption energies of ISM related particles have a significant impact in the chemical evolution of the universe. Observationally, most molecules are found in the gas phase instead of on the grain surface. The desorption rate of particles determines the fraction in the gas phase versus the fraction locked in the solid state. Therefore, desorption rates strongly affect the amount of molecules available for observations.

Among the most abundant elements, oxygen is especially interesting, because most of the biologically important molecules as we know contain oxygen. The desorption energy of atomic oxygen from a cosmic dust grain surface is an important parameter in astrochemistry, because it controls the availability of oxygen atoms on grains that can be involved in reactions. However, its value has not been measured in the laboratory. In Chapter 3 we present the measurement of this value using both an indirect method and a direct method.

When particles are already on the surface, there is a possibility that they react and form new molecules. There are three major mechanisms of surface reactions: the Langmuir-Hinshelwood (LH) mechanism, the Eley-Rideal (ER) mechanism, and the hot atom (HA) mechanism, although the distinction between them is not clear cut. Schematics of these three mechanisms are illustrated in Figure 1.2. In the LH mechanism, a particle sticks on the surface, does a random walk, or in other words, diffuses around the surface, until it finds a reaction counterpart and forms a chemical bond—if the reaction has no activation energy. To diffuse on the surface, it needs to overcome a diffusion energy barrier. The energy required for diffusion is obtained from the thermal energy of underlying surface. The diffusion rate can also be expressed in Arrhenius form:

$$\text{diffusion rate} = \nu_{\text{diff}} \exp(-\frac{E_{\text{diff}}}{k_{\text{B}}T}) \tag{1.11}$$

where ν_{diff} is the diffusion prefactor, which is not necessarily identical to the desorption prefactor. We label it with a subscript to distinguish it from the desorption prefactor. However, in reality, because of the lack of experimental measurement of this prefactor, it is usually assumed to be of the same value as the desorption prefactor. E_{diff} is the diffusion energy barrier. In the ER mechanism, a particle from the gas phase directly strikes another particle already on the surface and forms a chemical bond. This mechanism is the dominant one when the surface coverage is relatively high so that a direct strike is likely, or the residence time of the incoming particle is so short that the LH/HA mechanisms are inoperative.

In the HA mechanism, a particle from the gas phase lands on the surface but does not thermalize with the surface immediately. Instead, it moves with superthermal energy and

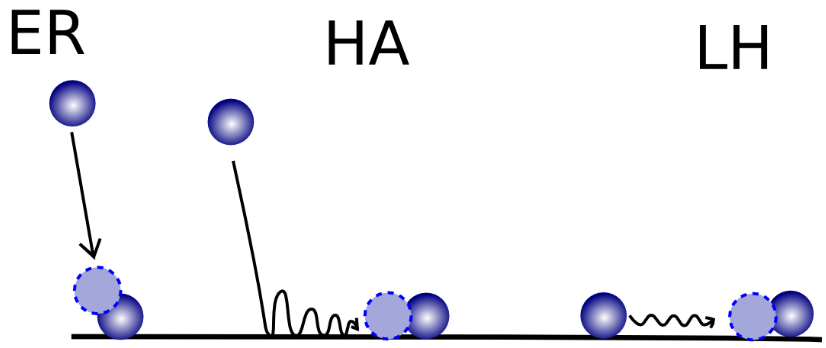

Figure 1.2: Schematics illustrating the three mechanisms of reactions on the surface, i.e., Eley-Rideal (ER), hot atom (HA) and Langmuir-Hinshelwood (LH) mechanisms.

loses energy as it goes. After a certain number of steps, it has lost most of its kinetic energy and gets trapped in an adsorption site or, if the temperature of the surface is high enough, it might leave the surface. Compared with the ER mechanism, the cross-section area for the HA mechanism is enhanced significantly. However, experimentally distinguishing between ER and HA mechanisms is difficult.

The coverage of species A on the surface exposed to species B from the gas phase, assuming a barrier-less reaction A + B→ AB, should decay exponentially

$$\mathrm{A(t)} = \mathrm{A(0)}\exp(-\sigma\phi \mathrm{t}) \tag{1.12}$$

where A(0) is the initial coverage of A; σ is the cross-section area; ϕ is the flux of B. By fitting the experimental data, the cross-section area σ can be obtained. Typically, if σ is about of the size of the A atom/molecule or smaller, the mechanism is ER, otherwise the mechanism is HA. However, there is no clear cut way to separate them, and the attribution of a reaction to one or the other mechanism is sometimes controversial (Vidali, 2013).

For simplicity, no reaction barrier was assumed in the above discussions. In reality, most reactions have a barrier. The barriers for surface reactions are not necessarily the same as the gas phase counterparts. Some reactions that have very low rates in the gas phase could be very efficient on the surface (e.g., H + H). To study the barrier of astrophysics/astrochemistry related surface reactions is an important topic in experimental astrophysics/astrochemistry. In gas-grain models, these reaction energy barriers enter as key parameters; however, most of them have not been measured in the laboratory. Some of them are "borrowed" from gas phase reactions, which are not necessarily correct.

In Chapter 5 we discuss the formation of hydroxylamine via the surface reaction NH_3 + $O \rightarrow NH_2OH$. Hydroxylamine is a precursor to glycine, the simplest amino acid. No efficient gas route has been found for hydroxylamine and surface reaction routes could be efficient. Grain surface reactions should contribute to its formation. We found that the reaction of NH_3 oxidation can efficiently form hydroxylamine and thus could be the mechanism of hydroxylamine formation in the ISM.

1.7 Rate equation model

Rate equation models are widely used in astrochemistry to study the chemical evolution of the ISM, both in the gas phase and on the grain surface. A typical model starts from certain initial conditions (temperature, elemental abundance, etc.), takes the rates for different physical and chemical processes obtained from laboratory measurements or theoretical calculations, and uses parameters (such as cosmic ray flux and UV radiation strength) to calculate the abundance of different species as a function of time. Here, we focus on the rate equation model for processes on grain surfaces. Experimentally, temperature programmed desorption (TPD) (Yates, 1985; Kolasinki, 2008) has been widely used as a tool to study gas-surface interactions in astrochemistry, such as adsorption-desorption and surface diffusion (He et al., 2011; Amiaud et al., 2006, 2007; Collings et al., 2004; Bisschop et al., 2006; Burke & Brown, 2010; Dohnálek et al., 2001; Hornekaer et al., 2005). A typical TPD experiment consists of two stages: the exposure stage, in which the substrate surface at low temperauture is exposed to adsorbate particles, and the warm-up stage (also called TPD stage), in which the substrate surface is warmed up to desorb adsorbate material. A mass spectrometer is placed in the vacuum chamber to monitor particles desorbing from the surface. Interpretation of TPD spectra is generally carried out using the Polanyi-Wigner rate equation; assuming first order desorption, the desorption rate can be written as:

$$R(t) \propto -\frac{\mathrm{d}\theta(t)}{\mathrm{d}t} = \nu\theta(t)\exp\left(-\frac{E_{\mathrm{des}}}{k_{\mathrm{B}}T(t)}\right) \tag{1.13}$$

where $R(t)$ is the desorption rate; ν is the desorption pre-exponential factor that depends on the substrate and adsorbate; $\theta(t)$ is the coverage defined as percentage of 1 ML (monolayer), i.e., the number of adsorbate particles divided by the number of adsorption sites on the surface; E_{des} is the desorption energy; k_{B} is the Boltzmann constant; $T(t)$ is the temperature of the surface. Based on this equation, one can find out a relation between the TPD peak temperature and the desorption energy; the latter is used in astrochemical models.

In the above simple rate equation, the surface is assumed to be uniform. However, in reality, surfaces are non-uniform. Specifically, cosmic dust surfaces are usually rough and amorphous. A continuous energy distribution should be used in the rate equation. Particles can even move around the surface, jumping between different adsorption sites. How particles behave on a rough surface is the focus of Chapter 6.

1.8 This thesis

In this thesis we study the gas-grain processes on the surface of cosmic dust analogues. In Chapter 2 we describe the experimental apparatus, and some calibration measurements that are used in later chapters. In Chapter 3 we use two methods, one direct and the other indirect, to measure the desorption energy of atomic oxygen from dust grain analogues. Chapter 4 studies the formation of water on a warm amorphous silicate surface via the ozone hydrogenation channel, and derives the desorption energy of OH radical from the surface. Chapter 5 studies the formation of hydroxylamine molecules on a grain surface via ammonia oxidation and estimate the reaction efficiency. Chapter 6 shows the application of a diffusion-desorption rate equation model to study how particles diffuse and desorb on a non-uniform surface.

Chapter 2

Experimental

2.1 Overview

The main apparatus consists of a 10 inch diameter cylindrical stainless steel chamber with two three-stage differentially pumped molecular beam lines. A schematic is shown in Figure 2.1. For the work presented in this thesis, only one beam line is used. In the following, the description of apparatus is presented in two subsections, namely, the main chamber and the beam line. A detailed description for the same apparatus is also available in Roser (2004), thus the emphasis of this chapter is on the changes made in recent years. In Section 2.4 we show the typical procedure of a TPD experiment and a method to calibrate beam flux.

2.2 Main chamber

The main chamber is pumped by a combination of turbomolecular pumps, an ion pump and a cryopump. A Ti sublimation pump is also attached to the main chamber for additional pumping when necessary. After each breaking of vacuum, the whole chamber is baked at about 100 ℃ for at least 3-4 days. Once cooled down to room temperature, the main chamber base pressure is (1-3)$\times 10^{-10}$ torr. At this pressure, it takes more than a couple of hours for a background gas of unit sticking coefficient to build a layer on the surface. A triple-pass

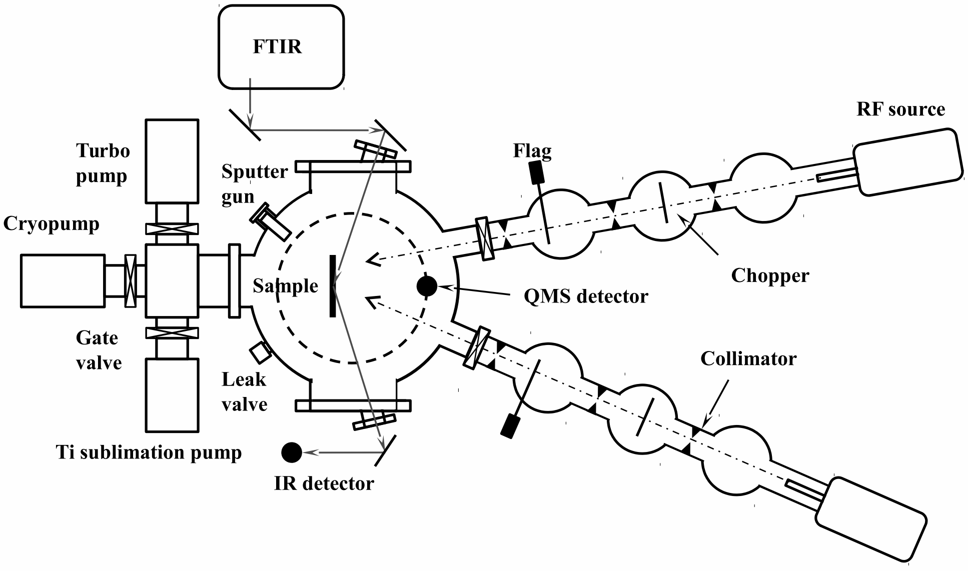

Figure 2.1: A schematic of the main apparatus.

Hiden HAL/3F quadrupole mass spectrometer (QMS) is mounted vertically on a doubly differentially pumped Thermionic RN-1000 rotary platform. The rotary platform can be rotated by a stepper motor which is controlled by an Applied Motion ST10-S stepper motor controller. So, the QMS can either face the molecular beam to measure its composition or face the sample to measure the species desorbing from the sample. The QMS is operating as residual gas analyzer (RGA), with an ionizer electron impact energy of 94.5 eV (optimized for D_2 signal) for experiments in Section 3.2 and Chapter 4, and 70 eV (a value most widely used) for experiments described in other chapters and sections. The QMS ion current can be read using client software provided by Hiden Analytical, or, alternatively, the ion pulse signal can be output to an external pulse counting device, such as a multichannel scaler (EG&G Ortec MCS-Plus), for better time resolution. The QMS ionizer is surrounded by a stainless steel cap with a Teflon cone attached to it. The entrance of the ionizer and the cone are lined up so that most of the gas molecules that enter the cone can go into the QMS ionizer. During the exposure stage, the QMS detector is moved away from the sample so that the detector does not block the molecular beam. During the TPD stage, the sample is close to the cone entrance, so that the cone fully covers the beam spot on the sample to increase the QMS signal while minimizing the noise due to the desorption from other cold parts of the sample holder. Schematics are shown in Figure 2.2.

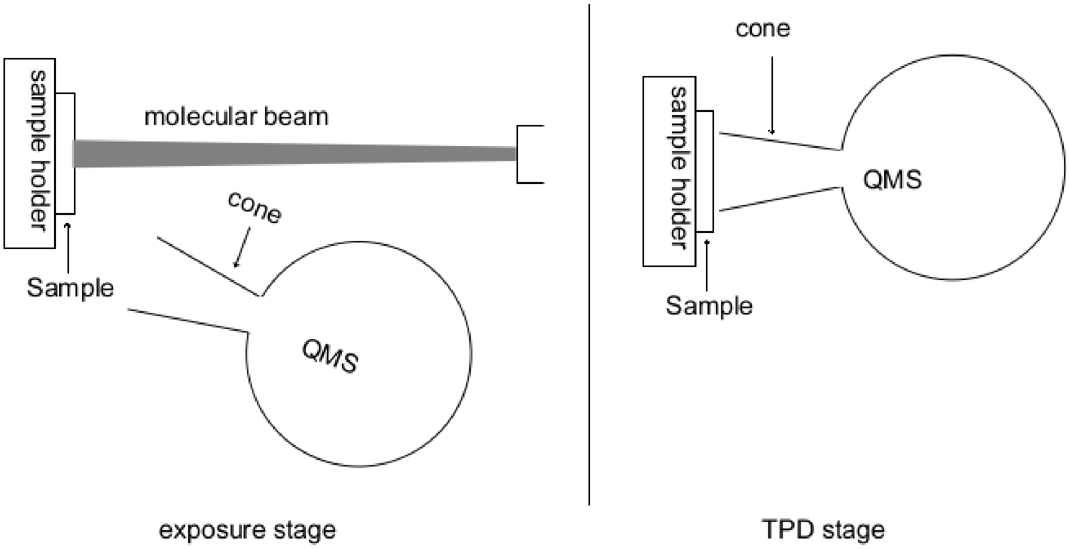

Figure 2.2: Top view of the QMS, the cone and the sample, in both exposure stage and TPD stage.

The sample holder is mounted on a XYZ 3-dimensional translation manipulator. The manipulator is sitting on a Thermionics RNN-600 rotary platform. Both the RNN-600 and the RNN-1000 rotary platforms are double differentially pumped by a turbomolecular pump and a rotary pump. This configuration gives the sample the freedom of translation in three dimensions and rotation around the vertical axis, and ensures good vacuum at the same time. The sample is provided by Dr. John R. Brucato of the Astrophysical Observatory of Arcetri in Italy. It is a 1 μm silicate film on top of a 1 cm diameter 1 mm thick gold coated copper disk deposited by the electron beam physical vapor deposition technique. A detailed description and characterization of the sample can be found in Jing et al. (2013). The sample can be cooled down by liquid helium to 8 K, or heated up to 500 K by a 25 ohm resistive heater buried underneath the sample disk. A 800 K thermal switch is inserted between the sample holder and the cold-finger. The thermal switch has a low thermal conductance at higher temperature but high thermal conductance at low temperature. It prevents the cold-finger from heating up during TPD stage while still enabling the sample to cool down to about 8 K during exposure stage. This reduces the desorption from the cold parts close to the cold-finger in TPD stage. A calibrated Lakeshore silicon diode thermometer is installed underneath the sample disk to measure the sample temperature. Since the sample is only 1 μm thick, it is assumed that the temperature of the silicate surface is the same as the temperature at the back of the sample disk. A silver film is inserted between the silicon diode sensor and the sample disk to improve the thermal conductivity. The silicon diode and the heater are connected to a Lakeshore 336 temperature controller, which can read out and control the sample temperature. When the sample is exposed to the beam (exposure stage), it is important to keep the surface temperature constant. This is achieved by a continuous liquid helium flow and the temperature controller running in a PID loop mode. Typically the temperature variation during the exposure stage is less than 0.1 K. When the desired surface temperature is relatively high, e.g., 50 K, the liquid helium flow is set to less than 20% of the maximum, just a little more than enough to remain the desired surface temperature. In this way the adsorption of molecules to the sample holder is minimized. When the sample is heated to carry out the TPD measurements, the sample has to be heated up in a reproducible way. In the following chapters, two heating modes are used. One is the constant heating power mode in the temperature controller while keeping the same liquid helium flow for each run (in Chapter 4 and Section 3.2); the other is the linear ramp rate heating mode in the controller (in Chapter 5 and Section 3.3). Both methods can yield reproducible heating ramp curves. To keep the sample clean, the sample is annealed at about 400 K for a few minutes at the beginning of the day. This cleaning procedure is sufficient to produce a clean surface because it yields identical experimental results on water formation with those after cleaning the sample with argon ion sputtering (Jing et al., 2013). Benchmark TPD runs are also performed routinely to make sure that the silicate surface is in the same condition among different sets of experiments.

2.3 Molecular beam

The molecular beam line has three differentially pumped stages. The first and second stage are pumped by diffusion pumps while the third stage is pumped by a turbomolecular pump. Collimators are installed between stages # 1 and # 2, #2 and # 3, and between stage # 3 and the main chamber (the stage number is counted from the source). These three collimators ensure that the molecular beam is well focused on a 3 mm diameter spot on the sample surface. A radio frequency dissociation source is mounted onto the first stage. A schematic is shown in Figure 2.3. The source was modified from a design by Slevin (1981). It consists of a Pyrex glass tube for gas flow, surrounded by water cooling. The dissociation source is surrounded by helix coil powered by a radio frequency (RF) power supply. The power supply is tuned by a LC circuit for impedance matching. A more detailed description of the dissociation source can be found in Roser (2004). Gas is introduced into the source via 1/4 inch stainless steel tubing and Tygon tubing. An Alicat MCS-5 mass flow controller is used to control the gas flow. The direct beam is measured by letting the QMS detector face the beam line and introducing gas into the beam line. The RF power is off when measuring the molecular beam intensities. The measured QMS signals versus gas flow for various gases are shown in Figure 2.4. In measuring NH_3 beam, there are both mass 17 amu and mass 16 amu, where mass 16 amu is due to the fragmentation of NH_3 in the ionizer.

Atomic species can be produced by turning on the RF power supply. The dissociation rate can be optimized by adjusting the RF power with the impedance matching circuit. The gas flow is also a determinant factor for the dissociation rate. Typically, the highest

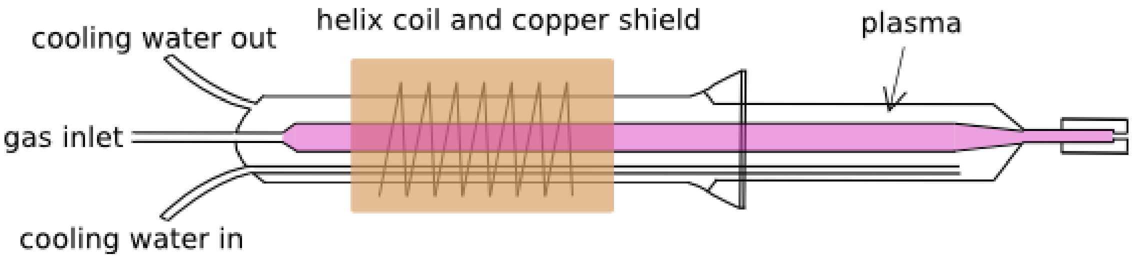

Figure 2.3: A drawing of the radio frequency dissociation source.

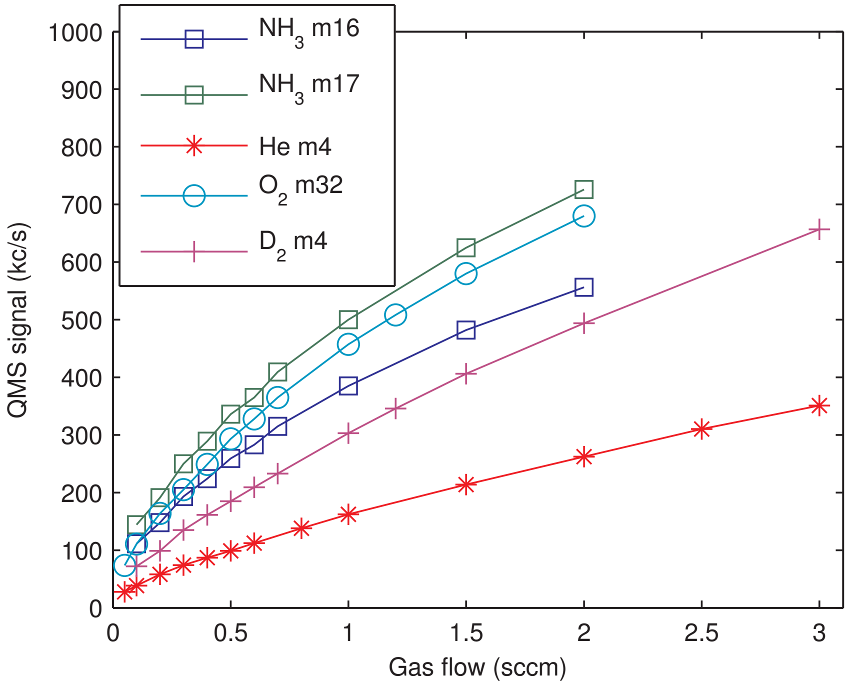

Figure 2.4: QMS measured beam counts versus gas flow for NH_3, O_2, D_2, He. In measuring NH_3 beam, there are both mass 17 amu and mass 16 amu, where mass 16 amu is due to the fragmentation of NH_3 in the ionizer.

dissociation rate is achieved at low gas flow ($\leq$ 0.1 sccm). The beam dissociation rate is checked typically on the same day as the TPD experiments or the day before. We use O_2 as an example to explain how the dissociation rate is measured. First, with the beam valve to the main chamber closed, we turn on the QMS to measure mass 32 amu in the main chamber background; assume the signal is C_{bg}. With RF off, we open the beam valve to measure O_2 again; let's call the QMS signal C_{off}. Then we turn on the RF and measure the mass 32 amu signal once again, call it C_{on}. C_{on} should be lower than C_{off} because of the dissociation (see

Figure 2.7 for an example). The dissociation rate can then be expressed as:

$$1 - \frac{C_{\text{on}} - C_{\text{bg}}}{C_{\text{off}} - C_{\text{bg}}} \tag{2.1}$$

Molecules are usually easy to crack into atoms. However, atoms can recombine on the wall of the Pyrex glass to form molecules again. The recombination rate is usually the limiting factor of the dissociation rate. This can be seen from the dissociation of NH_3 gas. When the RF is on, even if the RF power is as low as 10 W, the measured mass 17 amu and mass 16 amu beam intensities drop to almost background level immediately. The signal of mass 15 amu also drops. This indicates that the dissociation rate is almost 100 %, and there is a negligible amount of $NH_3/NH_2/NH$ in the beam. The signal of mass 28 amu (N_2) and mass 2 amu increase significantly; mass 14 amu increases slightly due to the fragmentation of N_2 in the ionizer.

For molecules present in the background gas such as H_2, C_{on} and C_{off} are only slightly higher than C_{bg}, and the measurement of dissociation rate is not accurate enough by using the QMS alone. By modulating the beam using a slotted wheel driven by an in vacuo DC motor (the chopper), a higher sensitivity can be achieved. A chopper disk with 1/40 open and 39/40 closed is used. An infrared LED and a photodiode facing each other are located to the opposite sides of the chopper disk; they can generate a synchronization signal in each cycle. Two signal acquisition schemes are used. In the first, the QMS ion pulse signal is sent to a lock-in amplifier, the synchronization signal from the photodiode is then the lock-in reference signal. In the second scheme, a multichannel scaler (MCS) is used. A schematic of this measuring scheme is shown in Figure 2.5. The photodiode signal serves as the trigger start signal for the MCS. Whenever the MCS receives a start trigger signal, it puts the ion pulse counts from the QMS in successive time bins. When the next start trigger signal comes, MCS stops the current cycle, and starts over from the first channel. Counts from a number of cycles are added to improve the signal to noise ratio. Using this method, the signal from the beam sharpens while the background flattens. The MCS spectra that shows the difference in H_2 signal between RF on and RF off are in Figure 2.6. The dissociation rate can be calculated using the above mentioned method.

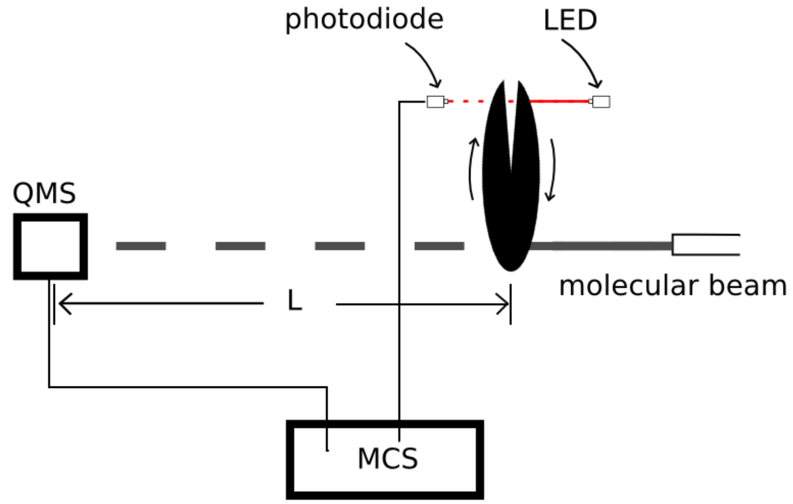

Figure 2.5: A schematic of the direct beam measurement using MCS and chopper.

The dissociation rates for O_2, H_2, and D_2 as a function of gas flow are presented in Figure 2.7. It can be seen that the dissociation rate decreases with gas flow; this is due to the increased recombination rate on the Pyrex glass wall. In the later chapters, two typical O_2 flows are used, 0.1 sccm and 0.3 sccm.

The velocity of atoms/molecules in the beam can also be measured using the MCS and the chopper. In each cycle of the chopper wheel, when the 1/40 open slot is aligned up with the photodiode, the photodiode trigger starts a new scan of the MCS. About half a cycle later (because of the width of the open slot is not infinitely small, the delay is not exactly one half), the molecular beam is aligned up with the open slot and molecules can pass the wheel. Suppose the velocity of the molecules is v and the distance from the chopper wheel to the QMS is L (which is about 76 cm), then it takes $t = L/v$ for the molecules to reach the QMS. We assume the response times of the QMS and the MCS are negligible and a peak shows up immediately after molecules reach the QMS. The time delay between the photodiode signal and the MCS peak signal is measured by the MCS. The time delay should be related to the

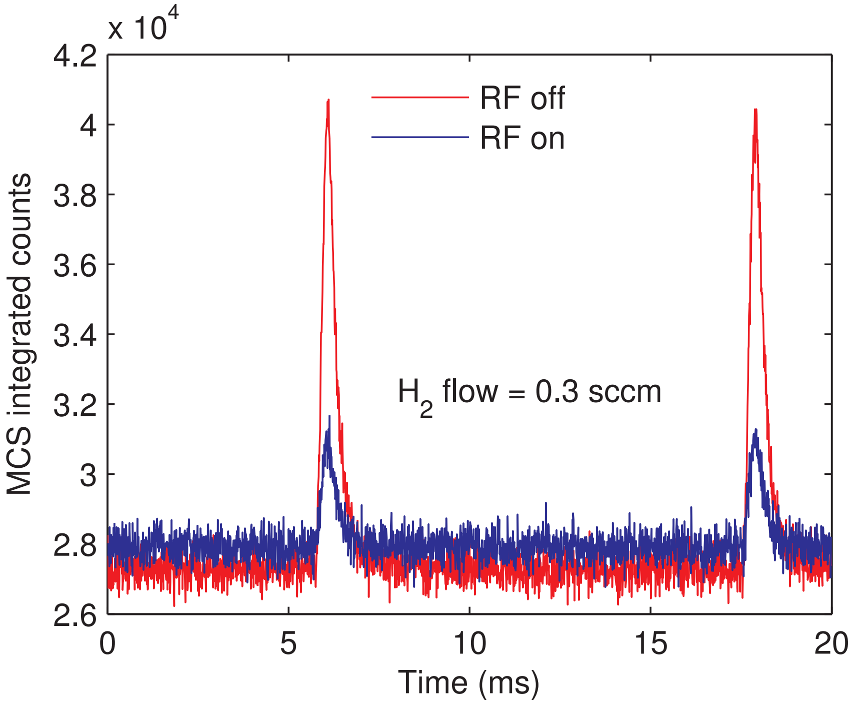

Figure 2.6: MCS recorded spectra of H_2 with RF on and RF off. The H_2 gas flow is 0.3 sccm.

beam velocity by:

$$\text{delay} = \frac{L}{v} + A(\frac{1}{f}) \tag{2.2}$$

where f is the chopper wheel spinning frequency and A is a constant value close to 0.5. By varying the frequency and measuring the delays, the velocity of the beam can be calculated. We send in molecular oxygen from the dissociation source with RF off to measure molecular oxygen beam velocity and with RF on to measure the atomic oxygen beam velocity. It should be noted that the velocity we measured is the most probable velocity instead of root mean square velocity because the MCS peak position only represents the most probable time delay. Based on a linear fitting of the curves in Figure 2.8, the velocity for O_2 and O are calculated to be 491 m/s and 687 m/s respectively. Compared to the most probable velocity for O_2 and O equilibrated at room temperature (300 K) 395 m/s and 558 m/s, the beam velocities are only moderately enhanced. The beam velocity of O is about $\sqrt{2}$ times that of O_2, which indicates that O is more or less at thermal equilibrium, but not at an excited

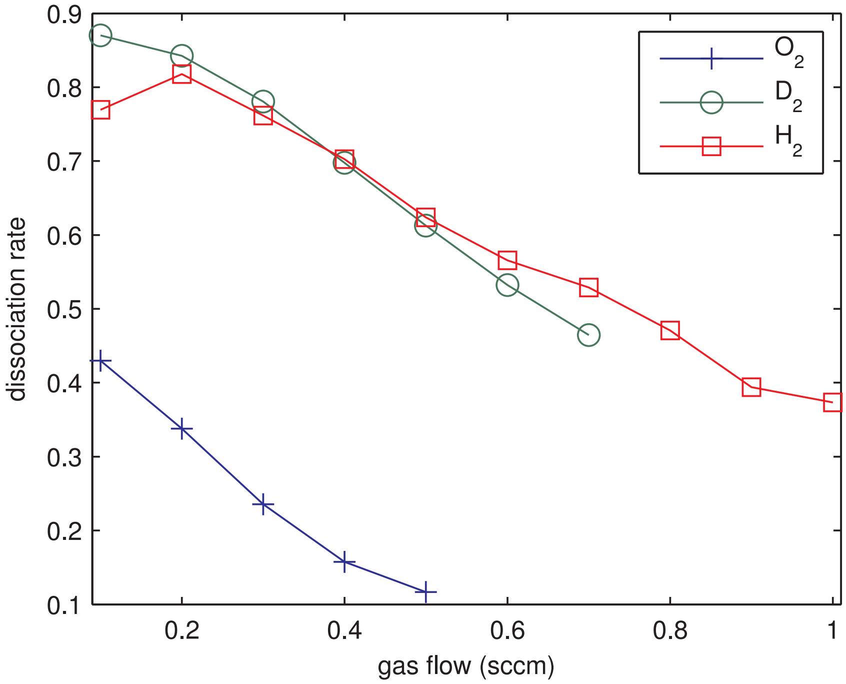

Figure 2.7: Dissociation rate for O_2, H_2, and D_2 at different gas flow rate.

state.

Because of the high collimation of the beam, opening the beam valve separating the beam line from the main chamber does not affect the main chamber pressure significantly. Typically, when the main chamber pressure is 1×10^{-10} torr, opening the beam valve increases the pressure to less than 2×10^{-10} torr. At this pressure increase, the adsorption onto the sample holder from the chamber background is negligible. The timing of the exposure is critically important when the exposure time is short. Since opening and closing the gate valve between the beam line and the main chamber takes a few seconds, there is an uncertainty in the length of the exposure. This problem is solved by installing a flag in the third stage of the beam line. The flag is a thin metal plate mounted on a rotatable rod; the beam can be blocked by rotating the rod by 90 degrees. The time it takes to rotate the flag (whether opening or blocking the beam) is well less than half a second, thus the uncertainty of the exposure length is less than one second.

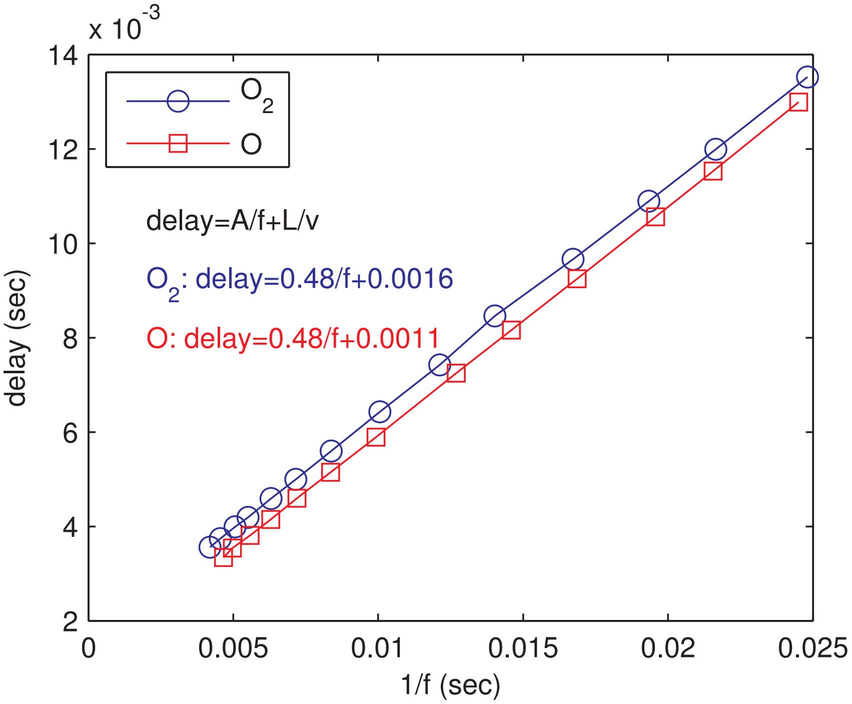

Figure 2.8: Measured time delays between the photodiode signal and the MCS peak versus the inverse of chopper frequency for both molecular oxygen and atomic oxygen. The parameters for a linear fitting are also included in the figure.

2.4 TPD experiments

Temperature programmed desorption (TPD) is a powerful and widely used tool to study surface kinetics. The focus of this thesis is the physical and chemical processes on the surface of interstellar dust grain analogs and most of the data taken in this thesis are based on TPD experiments. A schematic of a TPD experiment is shown in Figure 2.9. Typically, a TPD experimental run consists of two stages. The first stage is the exposure stage, in which the sample surface is kept at relatively low temperature and a certain dose of atoms/molecules are sent to the sample surface. In our specific experimental condition, we move the QMS cap and cone 60 degrees away from the beam so that the beam is not blocked by the cap. The QMS signal is recorded during the exposure stage to detect the reflection of atoms/molecules from the surface or newly formed molecules that are ejected from the surface. After the exposure stage, the sample is rotated by 60 degrees to face the QMS cone, then the sample is moved to about 2 mm from the sample, so that most of the desorbed molecules go into the QMS detector. The second stage is the TPD stage. In this stage, the surface is heated up to thermally desorb species from the surface. Both the surface temperature and the QMS signal are recorded by the computer, so that one can analyze the desorption profile. The temperature around which the desorption is highest indicates the strength of the binding energy between the atoms/molecules and the surface. The amount of atoms/molecules on the surface is proportional to the TPD peak area in the TPD spectrum. Figure 2.10 shows the TPD spectra of CO_2 on the amorphous silicate surface. From 0.5 minutes to 2 minutes of CO_2 exposure, the TPD peak temperature shifts to lower values. Between 2 minutes and 2.5 minutes of CO_2 exposure, there is a sudden change both in peak temperature and peak shape. This sudden change is due to the transition from submonolayer coverage to multilayer coverage. In the submonolayer coverage, molecules tend to fill the deep adsorption sites before they go to shallow adsorption sites. After one whole layer is built on the surface, additional CO_2 molecules adsorb on top of CO_2. In the multilayer region, the TPD peak temperature shifts slightly to the right. This TPD peak temperature shift with coverage can be used to calibrate the surface coverage of molecules. In the case of 0.3 sccm CO_2 flux, an about 2 minute dose corresponds to one monolayer (1 ML). The beam flux is then 0.5 ML/minute. In surface science, the surface adsorption sites density is typically taken to be 10^{15} cm^{-2}, thus the CO_2 beam flux is 8.3×10^{12} cm^{-2}s^{-1}. In the following chapters, the beam flux is calibrated similarly.

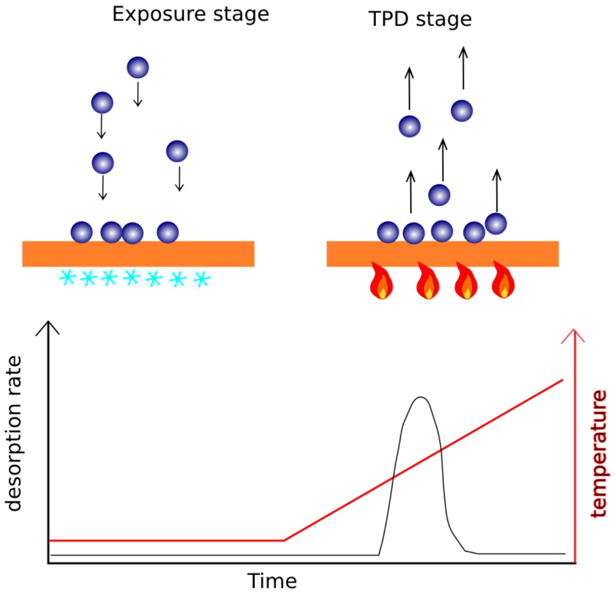

Figure 2.9: Schematic of a TPD experiment. In the exposure stage of a TPD experiment, sample surface stays at low temperature and atoms/molecules are sent to the sample. In the TPD stage, the sample surface is heated up to thermally desorb atoms/molecules from the surface, and a desorption peak shows up in the mass spectrometer signal.

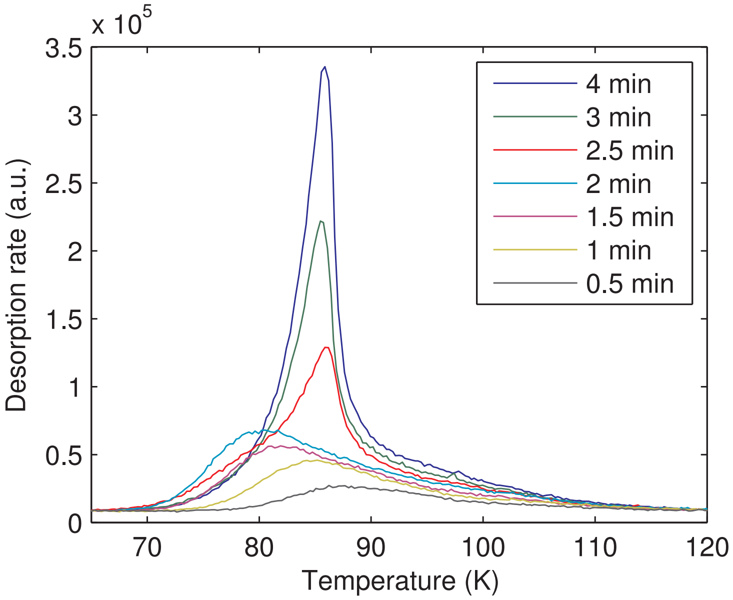

Figure 2.10: CO_2 adsorption-desorption TPD experiments on an amorphous silicate surface. During exposure stages, the CO_2 gas flow was 0.3 sccm. The exposure durations were 0.5 minute, 1 minute, 1.5 minutes, 2 minutes, 2.5 minutes, 3 minutes, and 4 minutes, respectively. The surface temperature during exposure was 50 K; the heating ramp rate during the TPD stage was 1 K/s.

Chapter 3

Atomic Oxygen Desorption from Dust Grain Surfaces

The desorption energy of atomic oxygen from an ISM-related surface is a fundamental parameter that enters ISM models. It determines the fraction of atomic oxygen on the grain surface versus that in the gas phase and influences the formation mechanisms (via gas phase reactions versus via grain surface reactions) and formation rates of oxygen-containing molecules. However, its value has not been measured in the laboratory because of technical difficulties. We employed two methods, one indirect and the other direct, to measure the desorption energy of atomic oxygen from three surfaces of astrophysical interest, i.e., the surface of an amorphous silicate and of porous amorphous water ice. In the indirect method, we first obtained the desorption energy of molecular oxygen from adsorption-desorption TPD experiments, then carried out ozone formation experiments via $O + O \rightarrow O_2$. We studied the surface kinetics of molecular oxygen obtained from TPDs of molecular oxygen, and measured the amount of ozone formed via $O + O_2 \rightarrow O_3$ with the QMS. With this information we used

---

Parts of this chapter have appeared in or are adapted from: Jiao He, Dapeng Jing, and Gianfranco Vidali. "Atomic oxygen diffusion on and desorption from amorphous silicate surfaces." Physical Chemistry Chemical Physics 16, no. 8 (2014): 3493-3500.

a rate equation model to calculate the surface kinetics (diffusion and desorption) of atomic oxygen. In the direct method, atomic oxygen is deposited onto surfaces and then desorbed from surfaces during TPD stages. By carefully controlling the experimental condition, the direct desorption of atomic oxygen is detected when heating up the sample surfaces. With the measured TPD peak temperature of atomic oxygen, we calculate its desorption energy. The values obtained by both methods agree with a model prediction which is based on astronomical observations.

3.1 Introduction

Oxygen is the third most abundant element in space after hydrogen and helium. It has attracted considerable attention among astrophysicists and astrochemists because it is an indicator of metallicity and thus a probe of the evolution of star-forming galaxies (Zahid et al., 2013). It intervenes in many reactions to form other molecules, such as H_2O, CO, and CO_2, and even more complex molecules, such as amino acids. Oxygen is found mostly in the gas phase in diffuse clouds (<10 H atoms/cm^3) and in molecular form (H_2O, CO, CO_2, etc.) in the ices of denser molecular clouds. Furthermore, O is locked in grains, mostly silicates of the type $(Fe_xMg_{1-x})_2$ SiO_4, $0 < x < 1$. It is found that both atomic and molecular oxygen are depleted in the gas phase, although there is some uncertainty to what extent (Jensen et al., 2005; Whittet, 2010; Melnick et al., 2012). The deficiency of oxygen in the gas phase, especially in molecular form, is particularly vexing (Melnick et al., 2012; Hincelin et al., 2011; Goldsmith et al., 2011). Various gas phase models predicted O_2 to be the third most abundant molecular species after H_2 and CO, at an abundance above 10^{-5} relative to H_2 in well shielded regions (see Goldsmith et al. (2011) and references therein). At this predicted abundance O_2 should play an important role in gas phase cooling. However, the search for O_2 with space observatories has found much lower O_2 abundances. Survey with the SWAS (Submillimeter Wave Astronomy Satellite) (Goldsmith et al., 2000) sets an upper limit of N(O_2)/N(H_2) smaller than 2.6×10^{-7}, which is two orders of magnitude lower than model predictions. With the launch of Odin, Larsson et al. (2007) observed the star-forming molecular cloud core ρ Oph A and found the O_2 abundance to be 5×10^{-8}, averaged over the Odin beam. Recent observation of ρ Oph A with Herschel Space Telescope has obtained a similar O_2 abundance as found with Odin (Liseau et al., 2012). In a recent search for O_2 emission in an ionization region towards the Orion bar with Herschel by Melnick et al. (2012), O_2 was detected; but again, at a much lower abundance than expected. In this region, dust grains are expected to be at higher temperature because of the radiation flux from stars. Oxygen is expected to be ejected from grains, for example by photodesorption, and in the gas phase it can form O_2 via reactions such as $O + OH \rightarrow O_2 + H$. Therefore O_2 is expected to be more abundant in the gas phase by a factor 10 than it would be in a similar UV quiescent region. Although O_2 was detected, its abundance came short of what models of the chemical evolution of that specific space environment predict (Hollenbach et al., 2009). In trying to reconcile observations with prediction of models, Hollenbach et al. (2009) and Melnick et al. (2012) pointed out that if the desorption energy of O is higher than the often assumed value of 800 K(Tielens & Hagen, 1982) (by a factor of 1.5 in Hollenbach et al. and a factor of 2 in Melnick et al.), then there would be much less oxygen desorbing from grains and consequently less O available for O_2 formation in the gas phase. This value of 800 K for O desorption from dust grains is found in many models of chemical evolution of interstellar medium (ISM) (Hasegawa et al., 1992; Garrod & Pauly, 2011; Hollenbach et al., 2009; Caselli et al., 2002, 1998; Stantcheva et al., 2002) but has no strong theoretical derivation (Tielens & Hagen, 1982) and no experimental confirmation. One of the goals of this chapter is to address this problem by presenting measurements of laboratory experiments of oxygen chemistry on an amorphous silicate surface, an analog of ISM dust grains, in simulated space conditions.

Besides atomic oxygen desorption from dust grains, there are other processes involving oxygen that influence the chemical make-up of ISM clouds. Oxygen-related chemical reactions begin when atomic oxygen (O) or molecular oxygen (O_2) stick to grain surfaces. Adsorbed O or O_2 can react with radicals that are on surfaces of grains to form more complex molecules (Vidali, 2013) via the Eley-Rideal, hot-atom or Langmuir-Hinshelwood mechanisms. Because of the low temperature of dust grains (10-15 K in dense molecular clouds), kinetics plays a large role in reactions on surfaces. Therefore, it is important to quantify the energetics of adsorption, desorption, and diffusion processes so accurate parameters can be entered in codes of the chemical evolution of ISM environments.

Oxygen chemistry has been studied on analogues of grain surfaces, both theoretically and experimentally. Xie et al. (2006) found theoretically that the atom-molecule reaction $^3O+HC_3N$ that has a barrier in the gas phase, can be effectively catalyzed by water ices to be barrierless. Tielens & Hagen (1982) proposed that water formation is through the hydrogenation of $O/O_2/O_3$ on grain surfaces. Lamberts et al. (2013) used a Monte Carlo code to study the surface reaction of O_2 hydrogenation. In all these theoretical works, the surface kinetics of oxygen were not studied in detail. Experimentally, the formation of ozone from energetic particles has been studied by several groups (Baragiola et al., 1999; Bennett & Kaiser, 2005; Ennis et al., 2011), but fewer experiments used atoms/molecules at thermal energy.

Extensive work has been done in recent years to study the formation of water (see Section 4.1). Miyauchi et al. (2008) investigated water and hydrogen peroxide formation by depositing H on cold O_2 ice and obtained the effective reaction rates. Cuppen et al. (2010) studied O_2 hydrogenation by simultaneous H and O_2 deposition. Dulieu et al. (2010) and Jing et al. (2011) studied water formation via atomic oxygen hydrogenation by depositing O and H via two beam lines. However, in these and similar experiments, because of the difficulty of obtaining a large dissociation fraction, what is deposited on the surface is not only O, but also O_2. O_2 and O can react and form O_3; therefore, in a typical experiment H is really reacting with a mixture of O, O_2, and O_3. Further investigation of oxygen surface kinetics is needed to explain the relative ratio among H+O, $H+O_2$ and $H+O_3$ channels. Other than water formation, there has been experimental work done on the formation of other oxygen-containing molecules on dust analogues. The formation of CO_2 is another reaction that requires grains. Roser et al. (2001), and more recently, Raut & Baragiola (2011), studied the formation of CO_2 on a surface by sending CO molecules together with oxygen atoms via beam lines, and found low efficiency for the $CO+O \rightarrow CO_2$ reaction. This might be because O tends to combine with another O to form O_2 instead of reacting with CO, or because undissociated O_2 diffuses fast on the surface and reacts with O to form O_3. All these studies require a better understanding of O/O_2 kinetics on surfaces.

The fundamental processes of oxygen desorption and diffusion on ISM related surfaces was not investigated until recently. Ward et al. (2012), when doing research on the reaction of atomic oxygen with CS_2 on a HOPG surface, introduced simple rate equations to analyze the data. However, they use Arrhenius expression for both Langmuir-Hinshelwood and Eley-Rideal mechanisms, which is probably incorrect. In a work by our group, Jing et al. (2012) studied the formation of molecular oxygen and ozone on an amorphous silicate surface using atomic ^{16}O and ^{18}O beams. A value of the diffusion energy barrier for atomic oxygen on an amorphous silicate surface was obtained. However, this value is not accurate because an error was found (Jing et al., 2014) in a calculation related to a control experiment to separate contributions of ozone from molecular oxygen in the O_2 signal in our detector (ozone is fragile and is known to break up into O_2^+ and O^+ in the ionizer of a quadrupole mass spectrometer). In Section 3.2 we present the results of further experimental investigations on the formation of ozone from reaction with atomic and molecular oxygen on silicates, and introduce a more comprehensive rate equation model to study the kinetics of O and O_2 on amorphous silicate surfaces. The desorption energy of atomic oxygen from an amorphous silicate surface is obtained indirectly. In Section 3.3, because of the improved experimental setup, we were able to measure directly the desorption energy of atomic oxygen from an amorphous silicate surface and a porous amorphous water ice surface by performing TPD experiments.

3.2 Indirect measurement of O desorption energy

3.2.1 Experimental

Apparatus

The dissociation source used in this set of experiments is of an old design. The dissociation efficiency is about 25% for molecular oxygen and is constant throughout the experiments. The calibration of beam flux is also different from that in Section 2.4. The beam flux calibration is obtained by flooding the chamber with O_2 and recording the main chamber pressure and the QMS ion counts. A conversion between QMS ion counts and the number of O_2 molecules is obtained. The flux is calculated to be about 7.6×10^{11} $cm^{-2}s^{-1}$ and 5.0×10^{11} $cm^{-2}s^{-1}$ for O_2 and O respectively (except for experiments as shown in Figure 3.1, which is about 20% lower). The gas used in the indirect method is isotope labeled $^{18}O_2$. In the rest of this section, oxygen always refers to ^{18}O, unless specified otherwise. The gas flow is controlled by a needle valve instead of the mass flow controller. A thermalcouple pressure gauge is used to measure the source gas pressure. The QMS settings are optimized for the D_2 signal (which also more or less optimizes the O_2 signal), with an ionizer electron impact energy 94.5 eV, SEM voltage 2200 V, filament emmision current 160 mA.

Description of experiments

Direct measurements of atomic oxygen desorption or diffusion are challenging because pure atomic oxygen is unavailable under present experimental conditions. Atomic oxygen is usually mixed with molecular oxygen. When O and undissociated O_2 from the beam land on the surface, there are two likely chemical reactions involved:

$$O + O \rightarrow O_2 \tag{3.1}$$

$$O + O_2 \rightarrow O_3 \tag{3.2}$$

The surface kinetics of atomic oxygen is studied by quantifying these two reactions, including determining the surface kinetics of O_2 and the amount of both reactants and products on the surface. The amount of O and O_2 from the beam line are characterized by direct beam measurements. The amount of O_3 formed can be measured by Fourier Transform Infrared spectroscopy (FTIR) or TPD. However, the focus of this investigation is on submonolayer coverage where the FTIR signal for O_3 is too weak, thus TPD techniques are used instead. When measuring O_3 using TPD and the QMS, another difficulty arises because O_3 breaks up into O^+ and O_2^+ in the QMS ionizer. Additional efforts are required to determine whether the measured O^+/O_2^+ are due to O_3 breaking up or O/O_2 desorption from the surface. This is discussed in detail later. The surface kinetics of O_2 can be obtained by performing O_2 adsorption-desorption experiments. Information from the ozone formation experiments and O_2 adsorption-desorption experiments enables the quantification of atomic oxygen surface kinetics, including the desorption energy and the diffusion energy barrier.

Two sets of O_2 adsorption-desorption experiments are performed. The first is O_2 adsorption-desorption TPD experiments at different surface temperatures to find out the residence time or, equivalently, the steady state coverage for O_2. It is found that during exposure at a surface temperature below 20 K, there is no steady state coverage, i.e., O_2 can build up ice. At 40 K and 50 K only 0.3 ML and 0.035 ML stick on the surface, respectively. Thus, in ozone formation experiments, if the surface temperature rises above 50 K, the amount of O_2 on the surface is negligible. The second set of O_2 adsorption-desorption experiments is adapted from one of our previous works (Jing et al., 2012). Here we summarize the second set and in the next Section we use a direct inversion method to extract the desorption energy distribution (see Chapter 6 for more discussion of the direct inversion method). In the experiments in Jing et al. (2012), the sample is kept at 20 K during the exposure to the molecular oxygen beam. The exposure time is incremented by 1.5 minutes from 1.5 to 15 minutes. After exposure, the sample is warmed up at a rate of about 1 K/sec[1] to a tem-

---

[1] The heating ramp rate is not linear, because a constant power heating mode is used and the heat conductance of the 800 K thermal switch is changing with the temperature.

perature higher than 100 K to thermally desorb O_2 molecules. After every 2 to 3 TPD runs the sample is heated up to higher than 230 K to desorb water that could have condensed on the surface. Based on an analysis of TPD peak areas and beam flux it is found that a 10.5 minutes exposure in the set of experiments by Jing (the flux in those experiments is different from the one used in other experiments reported in this Section) is equivalent to 1 ML. Here we focus on experiments at submonolayer coverage, and TPD traces are shown in Figure 3.1. An analysis of this set of experiments is in subsection 3.2.2.

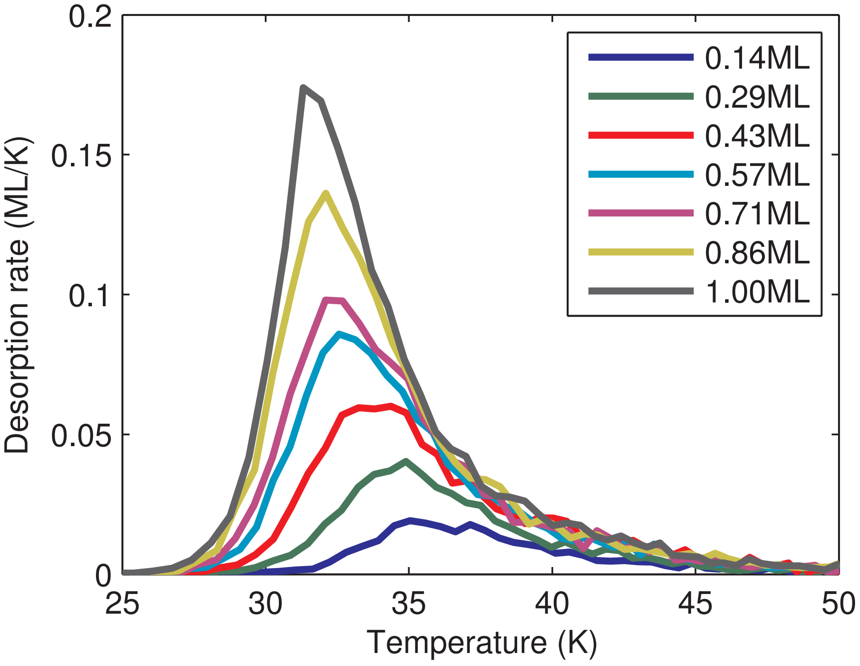

Figure 3.1: Adsorption-desorption of O_2 from an amorphous silicate surface kept at 20 K for different coverages. The heating ramp rate during the TPD stage is about 1 K/sec.

In the ozone formation experiments, we first check the composition of the beam and measure the flux of the various components. When the QMS detector is placed in front of the beam line, the amount of O_3 in the beam is negligible (less than 0.1% of the beam intensity). Ozone formation experiments are carried out next. We keep the amorphous silicate surface at 30 K, 40 K, 50 K and 60 K, and send the dissociated O/O_2 beam onto the sample for different durations, then we do a TPD. When the surface temperature during exposure stage is 30 K or 40 K, the sample is warmed up to 50 K and maintained for 2 minutes to desorb O_2 before the TPD, so as to make sure the atomic mass 36 amu TPD peak that appears at about 63 K is not from undissociated O_2 in the beam. This simplifies the analysis of ozone cracking in the ionizer. All relevant atomic masses, including mass 18 amu, 36 amu and 54 amu, are recorded both during the exposure stage and the TPD stage with the QMS facing the sample. In all measurements there is no discernible direct desorption of mass 18 amu other than background noise. Since O_3 can crack into O and O_2 in the QMS ionizer, mass 36 amu signal is at least partly due to the cracking of O_3. The TPD traces are shown in Figure 3.3. When the surface temperature during exposure stage is 60 K, there is no O_2 or O_3 detected in the TPD (not shown in the figure). This is because O_3 starts to desorb at around 60 K and O_3 formed during the exposure at 60 K desorbs quickly.

3.2.2 Results and analysis

In the following, we first obtain a desorption energy distribution of O_2 based on a direct inversion method. This is followed by a analysis of whether the mass 36 amu TPD peak at around 67 K is due to O_2 that is formed on the surface or due to ozone fragmentation. Then the ozone formation experimental data is analyzed using a rate equation model to find out the desorption energy of atomic oxygen.

Experiments of O_2 adsorption-desorption

To extract the desorption energy distribution from adsorption-desorption TPD experiments, the direct inversion method (more details in Chapter 6) is adopted. The Polanyi-Wigner equation is written as:

$$-\frac{\mathrm{d}\theta(t)}{\mathrm{d}t} = \nu\theta(t)\exp(-E_{\mathrm{des}}(\theta)/k_{\mathrm{B}}T) \tag{3.3}$$

where ν is the pre-exponential factor of the desorption. In general, ν depends on the substrate and adsorbate, but in this analysis the standard value $\nu = 10^{12}\ \mathrm{s}^{-1}$ is taken. $\theta(t)$ is the coverage defined as percentage of one monolayer, i.e., the number of particles (atoms or molecules adsorbed on the surface) divided by the number of desorption sites on the surface. The order of desorption is taken to be 1 in this paper. E_{des} is the desorption energy, k_{B} is Boltzmann constant, T is the surface temperature. Then, the coverage dependent desorption energy distribution can be calculated for each TPD trace as follows:

$$E_{\mathrm{des}}(\theta) = -k_{\mathrm{B}}T \ln\left(-\frac{\beta}{\nu\theta}\frac{\mathrm{d}\theta}{\mathrm{d}T}\right) \tag{3.4}$$

Here β is the heating ramp rate; E_{des} is the desorption energy of the lowest occupied site at a coverage of θ. A numerical derivative of E_{des} gives the E_{des} distribution $f(E_{\mathrm{des}})$, which satisfies:

$$\int f(E_{\mathrm{des}})\ \mathrm{d}E_{\mathrm{des}} = 1 \tag{3.5}$$

the integration is over the whole desorption energy spectrum. We obtained the desorption energy distribution for O_2 from the silicate surface $E_{\mathrm{des}}^{\mathrm{O_2}}$ which is shown in Figure 3.2. It can be seen that the distribution is peaked at about 78 meV. The O_2 diffusion energy barrier $E_{\mathrm{diff}}^{\mathrm{O_2}}$ is difficult to measure directly, especially for non-regular surfaces. Generally it is assumed that $E_{\mathrm{diff}} = \alpha E_{\mathrm{des}}$, where α is a number adopted to be between 0.3 and 0.8 (Garrod & Pauly, 2011). For amorphous surfaces the α value is higher than for regular surfaces. We therefore have an estimate of 23.3 meV$< E_{\mathrm{diff}}^{\mathrm{O_2}} <$ 62.4 meV depending on the assumed value of α.

O_3 formation

The TPD results are shown in Figure 3.3. There are both mass 36 amu (m36) and mass 54 amu (m54) peaks at about 63 K. An integration of the TPD traces shown in Figure 3.3 gives value reported in Table 3.1. The ozone yield at $T_{\mathrm{exp}} = 50$ K is about half of the yields when $T_{\mathrm{exp}} = 30$ K. If the desorption energy of O is 800 K (69 meV), as suggested by Tielens & Hagen (1982), which is lower than the desorption energy of O_2 (78 meV), then, because 30 K is close to the desorption peak temperature of O_2, an easy calculation should show that

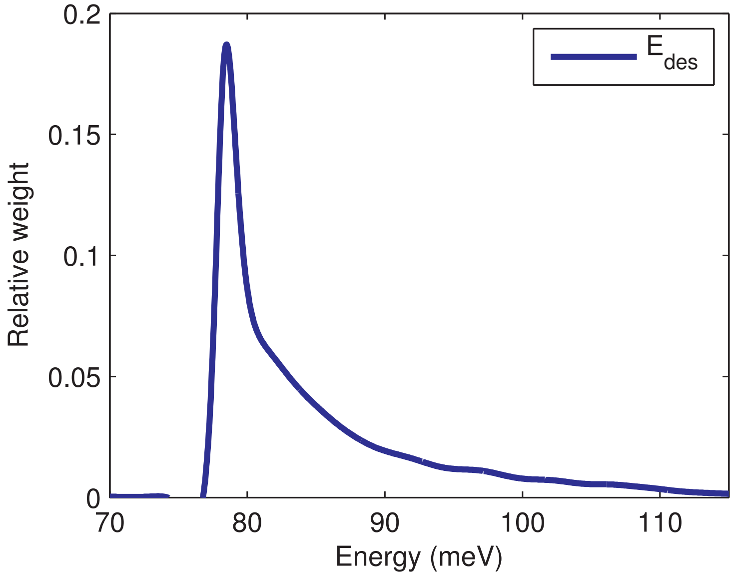

Figure 3.2: Distribution of $E_{\rm des}$ for O_2 on an amorphous silicate surface obtained from direct inversion of TPD data shown in Figure 3.1.

the residence time for both O and O_2 is orders of magnitude shorter at 50 K than at 30 K. One can calculate that the ozone yield at 50 K is also orders of magnitude lower than that of 30 K. But this disagrees with the experimental results shown in Figure 3.3. One then concludes that the desorption energy for O should be higher than 800 K.

In Table 3.1 the integrated TPD area ratio m36/m54 is almost a constant, which is between 15.8 and 17.8 for the experiments plotted in Fig (3.3). Besides, mass 36 amu and mass 54 amu appear at the same temperature and have similar shape. Now, a question arises: does the TPD peak of mass 36 amu in Figure 3.3 come from the undissociated O_2 from the beam, from O_3 cracking in ionizer or from O_2 ($O + O \rightarrow O_2$) as a result of O diffusion on the surface during the TPD? The first possibility can be excluded because undissociated O_2 desorbs at a temperature below 50 K, and the sample is kept at 50 K for at least 2 minutes before the TPD to make sure there is negligible undissociated O_2 left on the surface. The other two cases require more analysis. It is necessary to find out which one is true before quantifying the amount of ozone formed. If the mass 36 amu peak comes exclusively from O_3 cracking in the ionizer, then the ozone formed on surface is not mixed with O; if part of

Table 3.1: Integration of TPD traces from Figure (3.3). The last row is the TPD yield ratios of mass 36 amu to mass 54 amu.

T_{exp}	30 K			40 K				50 K				
Exposure (min)	10	20	30	5	10	15	30	5	10	15	20	30
$N(O_2)/10^4$	13.5	30.0	46.4	7.62	15.0	20.0	39.6	5.79	11.9	14.8	19.9	24.2
$N(O_3)/10^3$	8.2	17.2	29.5	4.29	8.41	11.9	23.5	3.23	7.51	8.63	11.2	14.1
$N(O_2)/N(O_3)$	16.4	17.4	15.8	17.6	17.8	17.0	16.9	17.9	15.8	17.1	17.8	17.2

the mass 36 amu peak is from O_2 desorption ($O+O\rightarrow O_2$) then there is O mixed with O_3. In the second case the temperature at which O starts to diffuse significantly should be virtually the same as the O_3 desorption temperature, since the TPD desorption peak of mass 36 amu occurs simultaneously with the TPD peak of mass 54 amu.

In a previous paper by our group (Jing et al., 2012), we did some analysis of the same TPD peak but with a different experimental setup and a different set of experimental data. Here, we summarize that experiment. We used two beam lines simultaneously, one with dissociated $^{16}O_2$ and the other with dissociated $^{18}O_2$. The sample temperature during exposure was 15 K. The TPD peak of mass 34 amu that was centered at about 63 K was attributed partly to $^{16}O^{18}O$ as a result of ^{16}O and ^{18}O diffusion during the TPD stage when the surface temperature was higher than about 60 K. The fact that both mass 34 amu and ozone desorb at the same temperature was explained as a coincidence between the temperature at which atomic oxygen diffuses significantly and the temperature at which ozone desorbs significantly. By comparing these data with current work and re-analyzing the previous data, it is found that the contribution of O diffusion to the TPD peak centered at 63 K was overestimated because the cross-section data used for O_3 break-up in the QMS ionizer might not have been appropriate for our ionizer (Jing et al., 2014).

Now we analyze the ratio of O_2/O_3 contributions to the TPD peak centered at 63 K using the data shown in Figure (3.3) and try to determine whether the mass 36 amu peak at 63 K is due to ozone cracking or O diffusion. First, let us suppose that atomic oxygen

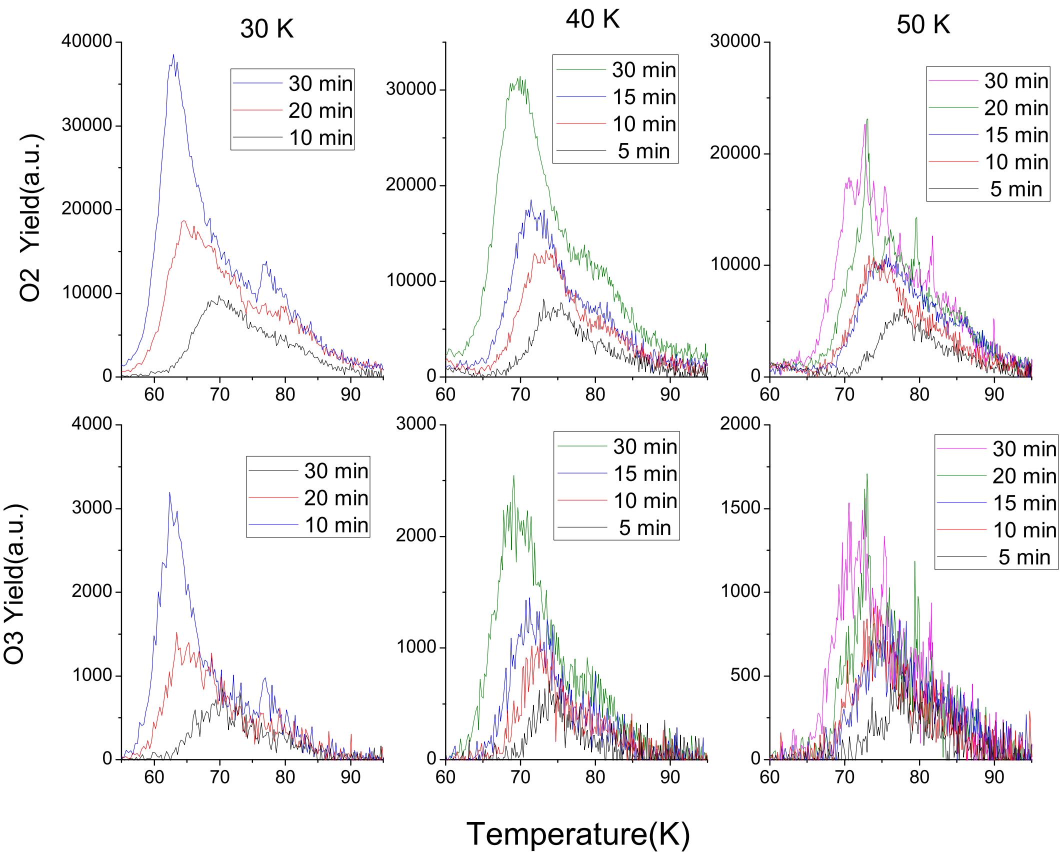

Figure 3.3: TPD traces of O_2 and O_3 after O/O_2 exposure for the indicated times; the surface temperatures during exposure are 30 K, 40 K and 50 K.

starts to diffuse significantly at above 60 K, as it was suggested in Jing et al. (2012). When the surface temperature during exposure, T_{exp} is 30 K, the residence time of O_2 on surface is tens of seconds assuming $E_{\mathrm{des}}^{O_2}$=78 meV. At this temperature the O_2 diffusion rate should be very high. Taking into account that the dissociation rate of O_2 is about 25% in our system, the O/O_2 ratio in the beam flux is about 2:3, and there should be enough O_2 to react with all the O. After warming up to 50 K to desorb residual O_2, what is left on the surface should be O_3 only. Since in the TPD stage the QMS records signals of both mass 36 amu (O_2) and mass 54 amu (O_3), the $O_2^{\mathrm{QMS}}/O_3^{\mathrm{QMS}}$ ratio should be a constant that depends on the cracking ratio of O_3 in the QMS ionizer; let this constant be C_1. In contrast, when T_{exp} is 50 K, the residence time for O_2 is very short; it is likely that there is not enough O_2 to react with all

Table 3.2: Calculation of O coverages $\theta(\mathrm{O})$ and O_2 coverages $\theta(\mathrm{O_2})$ at 30 K, 40 K, and 50 K, and of the O desorption energy $E^{\mathrm{O}}_{\mathrm{des}}$, assuming different α values. The units for coverages and desorption/diffusion energies are ML and meV respectively.

α	T	30 K	40 K	50 K	$E^{\mathrm{O}}_{\mathrm{diff}}$	$E^{\mathrm{O}}_{\mathrm{des}}$
0.3	$\theta(\mathrm{O})$	1.4×10^{-9}	2.4×10^{-7}	2.9×10^{-6}	45	150
	$\theta(\mathrm{O_2})$	1.0×10^{-2}	5.7×10^{-6}	9.1×10^{-8}		
0.4	$\theta(\mathrm{O})$	2.9×10^{-8}	2.3×10^{-6}	1.8×10^{-5}	61	152
	$\theta(\mathrm{O_2})$	1.0×10^{-2}	5.7×10^{-6}	9.1×10^{-8}		
0.5	$\theta(\mathrm{O})$	5.9×10^{-7}	2.2×10^{-5}	1.1×10^{-4}	76	153
	$\theta(\mathrm{O_2})$	1.0×10^{-2}	5.7×10^{-6}	9.1×10^{-8}		
0.6	$\theta(\mathrm{O})$	1.2×10^{-5}	2.1×10^{-4}	6.6×10^{-4}	92	153
	$\theta(\mathrm{O_2})$	1.0×10^{-2}	5.7×10^{-6}	9.1×10^{-8}		
0.7	$\theta(\mathrm{O})$	2.4×10^{-4}	2.1×10^{-3}	4.0×10^{-3}	108	154
	$\theta(\mathrm{O_2})$	1.0×10^{-2}	5.7×10^{-6}	9.1×10^{-8}		
0.8	$\theta(\mathrm{O})$	5.0×10^{-2}	2.0×10^{-2}	2.4×10^{-2}	123	154
	$\theta(\mathrm{O_2})$	1.0×10^{-2}	5.7×10^{-6}	9.1×10^{-8}		

the O, and it can be expected that there is both O_3 and unreacted O left on the surface. As the temperature goes above 60 K in the TPD stage, O starts to diffuse and forms O_2. Since there is both O_3 (from O_2+O) and O_2 (from O+O) desorption above 60 K, the $\mathrm{O}_2^{\mathrm{QMS}}/\mathrm{O}_3^{\mathrm{QMS}}$ ratio from the TPD peak area should be higher than C_1; let's call the ratio C_2. It can be shown that the percentage of O_2 (coming from O+O) that is mixed with O_3 in the TPD peak at $T_{\mathrm{exp}} = 50$ K is $O_2\%=(C_2 - C_1)/(C_1 + 1)$, and the percentage of O mixed with O_3 before the TPD is twice of O_2%. As is shown in table (3.1), $C_1 \approx 16.5$ and $C_2 \approx 17.2$; the difference between C_1 and C_2 is well within the error bars. The amount of O_2 mixed with O_3 in the TPD peak is negligible ($O_2\% \leq 4\%$). We conclude that the signal of mass 36 amu peak in the TPD peaks in Figure (3.3) is all due to ozone cracking in the ionizer. One can also obtain a temperature range in which the O start to diffuse significantly. Because our assumption that O starts to diffuse above 60 K turns out to be not true, the temperature at which O starts to diffuse significantly, $T^{\mathrm{O}}_{\mathrm{diff}}$, should be lower than 60 K. Furthermore, if one considers that $T^{\mathrm{O}}_{\mathrm{diff}}$ cannot be between 50 K and 60 K, or otherwise there would be a peak of mass 36 amu between 50 K and 60 K, then the temperature at which O starts to diffuse significantly $T^{\mathrm{O}}_{\mathrm{diff}}$ should be lower than 50 K.

Rate equation modeling

Our next step is to quantitatively describe the O_2 and O_3 formation processes using a rate equation model, and then obtain the values for diffusion energy $E_{\mathrm{diff}}^{\mathrm{O}}$ and desorption energy $E_{\mathrm{des}}^{\mathrm{O}}$ from the data.

The rate equations to describe O_2 and O_3 formation on the sample surface are written as:

$$\frac{\mathrm{d}\theta(\mathrm{O_2})}{\mathrm{d}t} = flux(\mathrm{O_2}) - \nu\theta(\mathrm{O_2}) \exp\left(-\frac{E_{\mathrm{des}}^{\mathrm{O_2}}}{k_{\mathrm{B}}T}\right) - \nu\theta(\mathrm{O_2})\theta(\mathrm{O}) \left(\exp\left(-\frac{E_{\mathrm{diff}}^{\mathrm{O_2}}}{k_{\mathrm{B}}T}\right) + \exp\left(-\frac{E_{\mathrm{diff}}^{\mathrm{O}}}{k_{\mathrm{B}}T}\right)\right) \tag{3.6}$$

$$\frac{\mathrm{d}\theta(\mathrm{O})}{\mathrm{d}t} = flux(\mathrm{O}) - 2\nu\theta(\mathrm{O})^2 \exp\left(-\frac{E_{\mathrm{diff}}^{\mathrm{O}}}{k_B T}\right) - \nu\theta(\mathrm{O_2})\theta(\mathrm{O}) \left(\exp\left(-\frac{E_{\mathrm{diff}}^{\mathrm{O_2}}}{k_B T}\right) + \exp\left(-\frac{E_{\mathrm{diff}}^{\mathrm{O}}}{k_B T}\right)\right) \tag{3.7}$$

On the right side of equation (3.6) the first term is known from the measurement of the direct beam, the second term describes the desorption of O_2, and the third term describes the reaction $O_2 + O \rightarrow O_3$. The O_3 formation rate depends on both the diffusion rate of O and O_2. However, if $E_{\mathrm{diff}}^{\mathrm{O_2}}$ and $E_{\mathrm{diff}}^{\mathrm{O}}$ are not very close to each other, the one with lower value dominates the diffusion process, and the other one can be ignored. Since it is already known that O_2 starts to diffuse at low temperature (well below O_2 desorption peak temperature), we assume $E_{\mathrm{diff}}^{\mathrm{O_2}} < E_{\mathrm{diff}}^{\mathrm{O}}$ and the O_3 formation term can be approximated by $\nu\theta(\mathrm{O_2})\theta(\mathrm{O}) \exp(-E_{\mathrm{diff}}^{\mathrm{O_2}}/k_{\mathrm{B}}T)$. On the right side of equation (3.7) the second term is due to the reaction $O + O \rightarrow O_2$. We assume the reaction product O_2 desorbs immediately after formation so that it does not go into equation (3.6). This is a reasonable assumption because the reaction $O+O \rightarrow O_2$ is strongly exothermic and thus one expects that O_2 leaves the surface upon formation. Direct desorption of O is ignored in equation (3.7) since O diffusion should take place before O desorption and O diffuses to form O_2 instead of desorbing directly. This assumption will be verified later after obtaining the desorption energy of O.

The equations can be simplified by assuming steady state conditions. When the surface temperature during exposure, T_{exp}=30, 40 or 50 K, reactions should proceed fast and reach a steady state quickly because of the high mobility of O_2. In steady state, equation (3.6) and equation (3.7) can be expressed as:

$$flux(\mathrm{O_2}) = \mathrm{O_2} \text{ desorption rate} + \mathrm{O_3} \text{ formation rate} \tag{3.8}$$

$$flux(\mathrm{O}) = \mathrm{O_2} \text{ formation rate} + \mathrm{O_3} \text{ formation rate} \tag{3.9}$$

where $flux$ represents the deposition rate from the beam. Equation (3.8) and (3.9) say nothing more than that all the O_2 coming from the beam either desorbs or forms ozone, while all the O coming from beam either forms O_2 or ozone. By integrating the TPD peak areas in Figure 3.3 (including both mass 36 amu and mass 54 amu because both of them are coming from ozone desorption) and comparing with direct beam measurement, equation (3.8) and (3.9) lead to:

at 30 K: O_3 formation rate $= 0.44\ flux(\mathrm{O_2}) = 0.65\ flux(\mathrm{O})$
at 40 K: O_3 formation rate $= 0.42\ flux(\mathrm{O_2}) = 0.63\ flux(\mathrm{O})$
at 50 K: O_3 formation rate $= 0.31\ flux(\mathrm{O_2}) = 0.46\ flux(\mathrm{O})$

Notice that there is a significant drop in O_3 formation rate between 40 K and 50 K. Equation (3.9) then suggests that between 40 K and 50 K there is a significantly increasing amount of O that forms O_2 instead of O_3. One might think that perhaps between 40 K and 50 K O starts to desorb directly; however, it is verified later that O does not desorb significantly. O must start to diffuse significantly between 40 K and 50 K. In subsection 3.2.2 we argued that at 30 K the O should be all consumed by O_2, but the QMS measurements shows that only 65% of O is consumed. An explanation of this discrepancy might be that in a QMS the detection efficiencies for different gases are different, O_3 (including un-cracked O_3 and cracked O_3) could have lower detection efficiency than O_2, and the QMS signal height comparison must be corrected for different gases. Thus, we let the O_3 formation rate = flux(O) at 30 K and correct for the other O_3 amounts proportionally. After correction, at 30 K all the O are converted to O_3, at 40 K about 97% of O are converted to O_3, at 50 K 71% of O is converted to O_3 while the remaining 29% diffuse and form O_2.

Combining equation (3.6)-(3.9) and solving analytically for $\theta(\mathrm{O})$ and $\theta(\mathrm{O_2})$:

$$\theta(\mathrm{O}) = \frac{\mathrm{O_3 \text{ formation rate}}}{\mathrm{flux(O_2) - O_3 \text{ formation rate}}} \times \exp\left(-\frac{E_{\mathrm{des}}^{\mathrm{O_2}} - E_{\mathrm{diff}}^{\mathrm{O_2}}}{k_{\mathrm{B}}T}\right) \tag{3.10}$$

$$\theta(\mathrm{O_2}) = \frac{\mathrm{flux(O_2) - O_3 \text{ formation rate}}}{\nu \exp(-E_{\mathrm{des}}^{\mathrm{O_2}}/k_{\mathrm{B}}T)} \tag{3.11}$$

In equation (3.10) and (3.11) the only variable is $E_{\mathrm{diff}}^{\mathrm{O_2}}$; in the expression $E_{\mathrm{diff}}^{\mathrm{O_2}} = \alpha E_{\mathrm{des}}^{\mathrm{O_2}}$ one lets α= 0.3, 0.4, 0.5, 0.6, 0.7 and 0.8, and calculate $\theta(\mathrm{O})$ and $\theta(\mathrm{O_2})$ values for different values of T and α. The calculated values of $\theta(\mathrm{O})$ and $\theta(\mathrm{O_2})$ are shown in table 3.2. To estimate the O diffusion energy barrier $E_{\mathrm{diff}}^{\mathrm{O}}$, we consider that at $T_{exp} = 50$ K 29% of O diffuses and forms O_2 instead of O_3, and plug in the values of $\theta(\mathrm{O})$ corresponding to different α values, and T=50 K, into the following equation:

$$2\nu\theta(\mathrm{O})^2 \exp\left(-\frac{E_{\mathrm{diff}}^{\mathrm{O}}}{k_{\mathrm{B}}T}\right) \approx 0.29 \text{ flux(O)} \tag{3.12}$$

and then calculate for $E_{\mathrm{diff}}^{\mathrm{O}}$. The desorption energy for O can be calculated using $E_{\mathrm{des}}^{\mathrm{O}} = E_{\mathrm{diff}}^{\mathrm{O}}/\alpha$. Here, we are assuming the α values are the same for both atomic and molecular oxygen. The calculated results are shown in Table 3.2. It can be seen that even if α varies between 0.3 and 0.8, the calculated atomic oxygen desorption energy $E_{\mathrm{des}}^{\mathrm{O}}$ is almost the same. The value is $E_{\mathrm{des}}^{\mathrm{O}} = 152 \pm 2$ meV. The uncertainty in $E_{\mathrm{des}}^{\mathrm{O}}$ value comes mostly from the uncertainty in the determination of the O_3 formation efficiency. By allowing a large 50% uncertainty in the determination of O_3 amount, the change in $E_{\mathrm{des}}^{\mathrm{O}}$ value is 20 meV at most. Then it can be concluded that the desorption energy for atomic oxygen is $E_{\mathrm{des}}^{\mathrm{O}} = 152 \pm 20$ meV (1760±230 K).

In the above discussion, no O direct desorption is assumed. This assumption can be verified now. The ratio between the amount of O due to O desorption and the $\mathrm{O+O \rightarrow O_2}$

amount can be calculated as:

$$\frac{\nu\theta(\mathrm{O})\exp\left(-E_{\mathrm{des}}^{\mathrm{O}}/k_{\mathrm{B}}T\right)}{2\nu\theta(\mathrm{O})^2\exp\left(-E_{\mathrm{diff}}^{\mathrm{O}}/k_{\mathrm{B}}T\right)} \tag{3.13}$$

The value is between 4.2×10^{-6} for $\alpha = 0.3$ and 1.6×10^{-2} for $\alpha = 0.8$, which is much less than 1. Thus, the assumption is correct and it is fine to ignore the atomic oxygen desorption term in equation (3.7).

In the above lengthy derivation, we obtained the desorption energy of of atomic oxygen on amorphous silicate surface in an indirect method. In the next section, we present a direct measurement of this energy.

3.3 Direct measurement of O desorption energy

3.3.1 Experimental

In this set of measurements, the experimental setup is optimized for measuring atomic oxygen desorption. The dissociation source is re-designed to improve oxygen dissociation rate (see Figure 2.3). The new source has a more sufficient water cooling and smaller surface to volume ratio than the old source. Therefore the dissociation ratio is enhanced. The gas flow is controlled by a mass flow controller to ensure stable flow. The QMS settings are also different from that in the indirect measurements. The ionizer electron energy is decreased from 94.5 eV to 70 eV in order to decrease the fragmentation of ozone. Correspondingly, the SEM voltage and filament emission current are increased to 2300V and 300 mA in order to compensate for the decreased electron impact energy. Oxygen gas used in this Section is ^{16}O instead of ^{18}O because the chamber background of mass 16 amu is much lower than the mass 18 amu (water). In the rest of this Section, oxygen always refers to ^{16}O unless specified otherwise.

The procedures to calibrate the beam flux are described in Section 5.2.1 and 2.4. When the molecular oxygen beam is about 0.34 ML/minute (3.4×10^{14} cm^{-2}minute^{-1}), the efficiency of dissociation is 42 %. Thus the beam intensities of O and O_2 are 0.29 ML/min (2.9×10^{14} cm^{-2}minute^{-1}) and 0.20 ML/min (2.0×10^{14} cm^{-2}minute^{-1}), respectively.

During the atomic oxygen (O) exposure, because the dissociation rate is not unity, there is always O_2 mixed with O, so ozone formation via $O+O_2 \rightarrow O_3$ is likely. When O desorption is seen in the TPD, it could come from the bare silicate surface and/or from ozone that was formed on the silicate as explained above. To find out which one is true, the silicate surface was pre-covered with different coverage of ozone before depositing atomic oxygen. If O desorbs from the silicate surface, then as the pre-covered ozone approaches one monolayer, the amount of O desorption should decrease to zero. In the other case, if O desorbs from an ozone patch, then as the pre-covered ozone amount increases from zero to one monolayer, the amount of O desorption should increase linearly. The correlation between the coverage of ozone and the amount of atomic oxygen direct desorption in the TPD can suggest whether O is desorbing from the silicate surface or from ozone. It will be shown later that the former is true. The presence of ozone on the silicate surface actually helps to decrease the formation of O_2 and O_3 via, respectively, the O+O and the $O+O_2$ reactions, since O and O_2 do not react with O_3. Ozone functions as an obstacle in the diffusion of O and O_2 on the surface. In dense clouds, dust grains are usually covered by ice mantles, with water as the main component. We also carried out measurements on porous amorphous water ice. The ice substrate was prepared with background deposition through a microcapillary doser. The thickness was estimated from the background pressure and the duration of the deposition. A 500 ML (with an uncertainty of 30 %) porous amorphous water ice film was deposited at 70 K on top of a 500 ML single crystalline water ice. The ice film was cooled down to lower temperatures for O/O_2 beam irradiation and TPD. During the following TPD experiments, the porous ice film was maintained below 70 K to prevent pore collapse in the ice films (see the temperature ramp in Figure 3.4).

3.3.2 Results and analysis

Figure 3.4 shows temperature programmed desorption (TPD) spectra of oxygen from a porous water ice film. We deposit 8 minutes of O/O_2 on porous water ice at 48 K. After the exposure, the surface is cooled down to 20 K and then heated up at a linear ramp rate of 10 K/minute to 70 K to desorb the atoms and molecules on the surface. During the TPD, the desorption rate is recorded by the QMS facing the sample. Ozone is formed on the ice and comes off at about 67 K. Because ozone is fragile against electron impact ionization, a good fraction breaks up into O_2^+ and O^+, as it can be seen from the peaks of mass 16 amu and 32 amu at about 67 K. In the mass 16 amu signal, there is a peak at 57 K, which is due to O direct desorption. As the sample is heated, O diffuses and forms O_2, and O_2 leaves the surface upon formation, because of the short residence time of O_2. The mass 32 amu peak centered at about 50 K is due to O_2 formation via O diffusion. As O is gradually used up, the O_2 formation rate decreases, and the rate of O direct desorption increases. The TPD peak area of O direct desorption corresponds to about 3% of a layer.

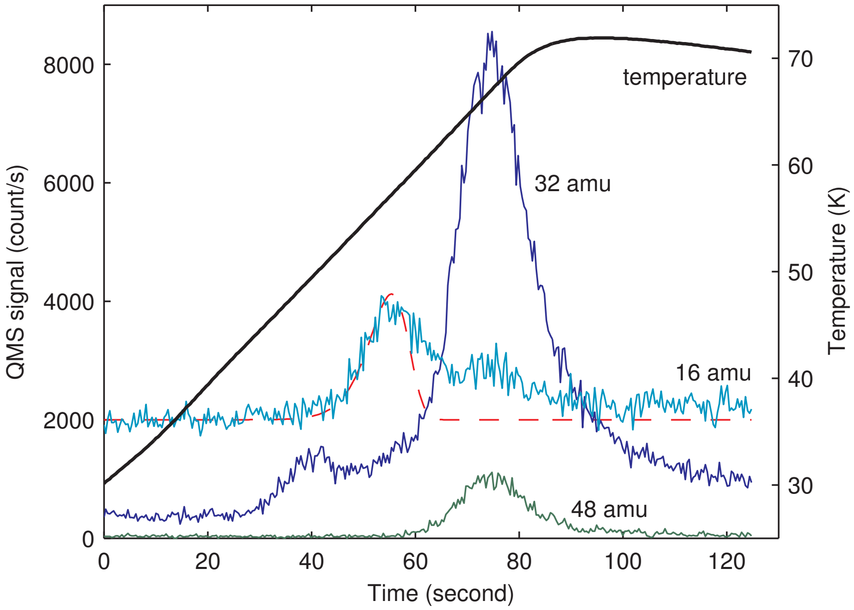

Figure 3.4: TPD traces of mass 16, 32, 48 amu after depositing 8 minute O/O_2 at 48 K on porous amorphous water ice. The heating ramp is 10 K/minute. The dashed line shows a fitting of the mass 16 amu peak using $E_{\mathrm{des}}(\mathrm{O}) = 1660$ K (see text).

Similar experiments were performed on the surface of an amorphous silicate. Compared to porous amorphous water ice surface, the amorphous silicate surface is flatter. The mobilities of O and O_2 on it are higher, and the formation of O_3 and O_2 are also faster. To hinder the formation of O_2 and O_3, and leave more atomic oxygen on the surface available for direct desorption, we pre-coated the surface with a fraction of a layer of O_3. We ascertained that O_3 does not react with atomic oxygen or molecular oxygen; O_3 is used to hinder the diffusion rate of atomic and molecular oxygen. To find out whether atomic oxygen is desorbing from bare amorphous silicate surface or ozone patch, measurements were performed to check the amount of O direct desorption from silicate surface covered with 0.2 ML, 0.4 ML, 0.6 ML, and 0.8 ML of ozone. Figure 3.5 shows the TPD spectra after depositing 480 seconds of O/O_2 on a 0.2 ML O_3 pre-coated amorphous silicate surface. In the figure, the two contributions to the mass 16 amu peak, i.e., O direct desorption and O_3^+ fragmentation, are merged into a single broad peak. To find out the peak position and peak area of O direct desorption, the O_3^+ contribution needs to be subtracted out. The fragmentation pattern of O_3^+ is measured by O_3 TPD experiments and not shown here. The raw TPD data and the data after subtracting O_3^+ contributions are shown in Figure 3.6. In each panel of this figure, the first row has the raw TPD data, while in the bottom row the contributions of ozone fragmentation to mass 16 amu have been subtracted to show the amount of direct O desorption. After this subtraction, the O direct desorption peak is centered at about 64 K and is clearly different from the ozone desorption peak. We also found that as the coverage of the pre-coating ozone layer increases from 0.2 ML to 0.4 ML, the amount of O direct desorption increases. This is because the increased ozone amount helps to lower the O diffusion rate. However, when the pre-coating ozone is more than 0.6 ML, there is almost no O direct desorption peak. This indicates that the observed O direct desorption is from bare silicate surface instead of ozone ice; otherwise, the O direct desorption amount should be positively correlated with the amount of ozone pre-coating.

The desorption energy of atomic oxygen from different surfaces can be calculated using

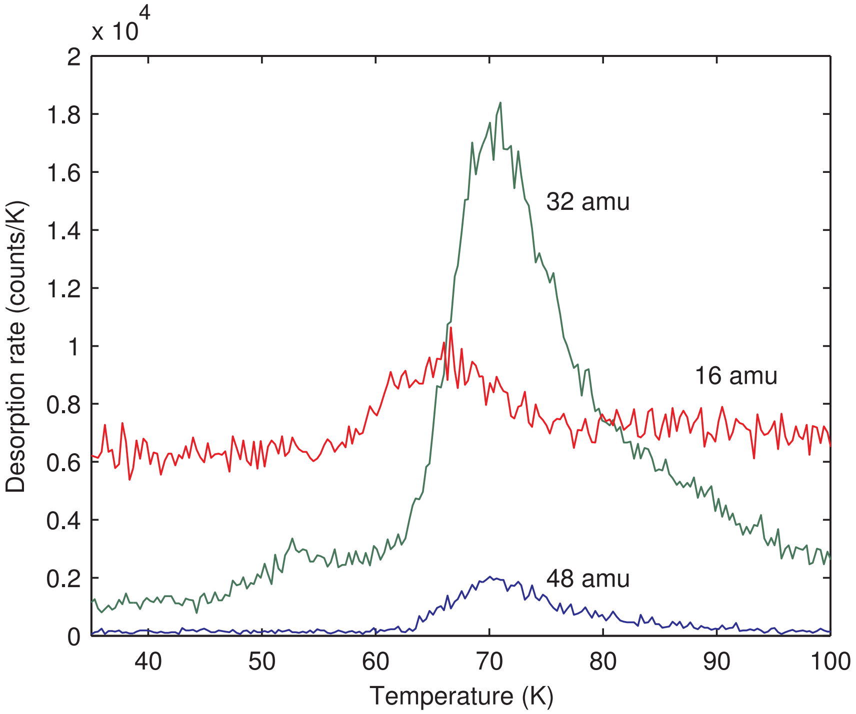

Figure 3.5: TPD traces of 16, 32, 48 amu after depositing 8 minutes of O/O_2 at 48K on an amorphous silicate that has been pre-coated with 0.2 ML of ozone.The heating ramp is 30 K/minute. The inset shows the temperature ramp.

an Arrhenius-type expression:

$$\frac{\mathrm{d}N(t)}{\mathrm{d}t} = -\nu N(t)\exp(\frac{E_{\mathrm{des}}}{k_{\mathrm{B}}T(t)}) \tag{3.14}$$

where $N(t)$ is the number of molecules on the surface at time t; ν is a pre-exponential factor which is standardly taken to be 10^{12} s^{-1}; E_{des} is the desorption energy; k_{B} is the Boltzmann constant; $T(t)$ is the surface temperature. In Figure 3.4 the dashed line shows the fitting of mass 16 amu trace using E_{des} = 1660 K. In Figure 3.7, the mass 16 amu traces in the top-right panel of Figure 3.6 after subtraction of O_3 contribution are plotted together with a fitting using E_{des} = 1850 K. The energy values are shown in Table 3.3. The error bars of the desorption peak temperature are determined by the uncertainty in locating the peak positions. The width and shape of the TPD peak are not taken into account. Therefore, the error bar of desorption energy does not represent the width of distribution; instead, it

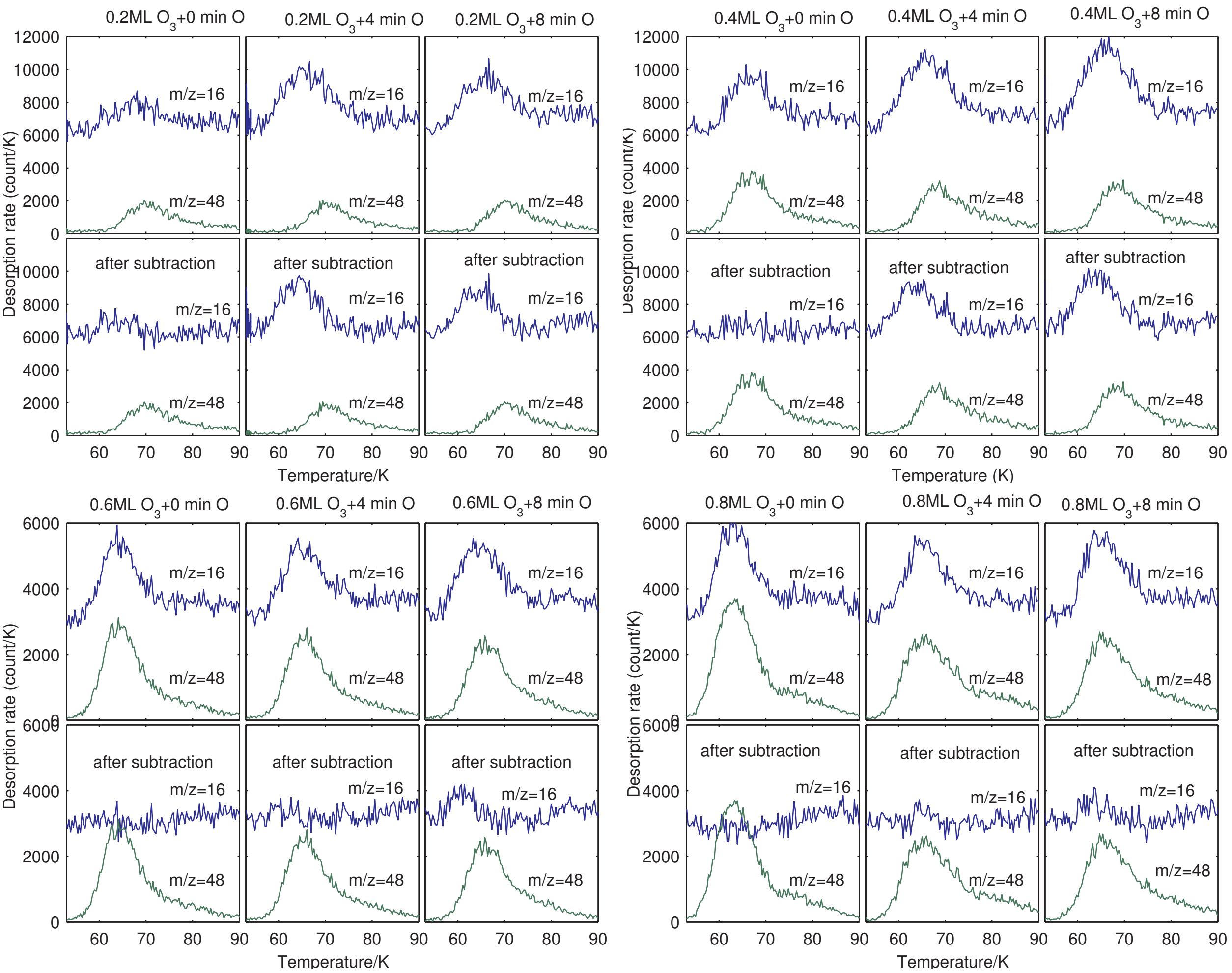

Figure 3.6: TPD traces of mass 16 amu (blue) and mass 48 amu (green) after deposition of 0 minute, 4 minutes, and 8 minutes of O/O_2 on 0.2 ML, 0.4 ML, 0.6 ML, and 0.8 ML of O_3 pre-coated amorphous silicate. The heating ramp is 0.5 K s^{-1}. The top row of each panel has the original TPD traces while in the bottom row the contribution of O_3^+ fragmentation to the signal of mass 16 amu has been subtracted.

represents only the uncertainty in finding the peak of the TPD trace.

Simulations using a phtodissociation region (PDR) model with updated values for atomic oxygen desorption energy are in progress in collaboration with Michael Kaufman who did simulations of oxygen chemistry using a steady-state model of a PDR. This is a typical simulation of PDR regions at the surface of molecular clouds, such as the Orion Bar. The model simulates the chemical structure of molecular clouds as a function of the depth into the cloud. A constant gas density and an external far-ultraviolet (FUV) irradiation are

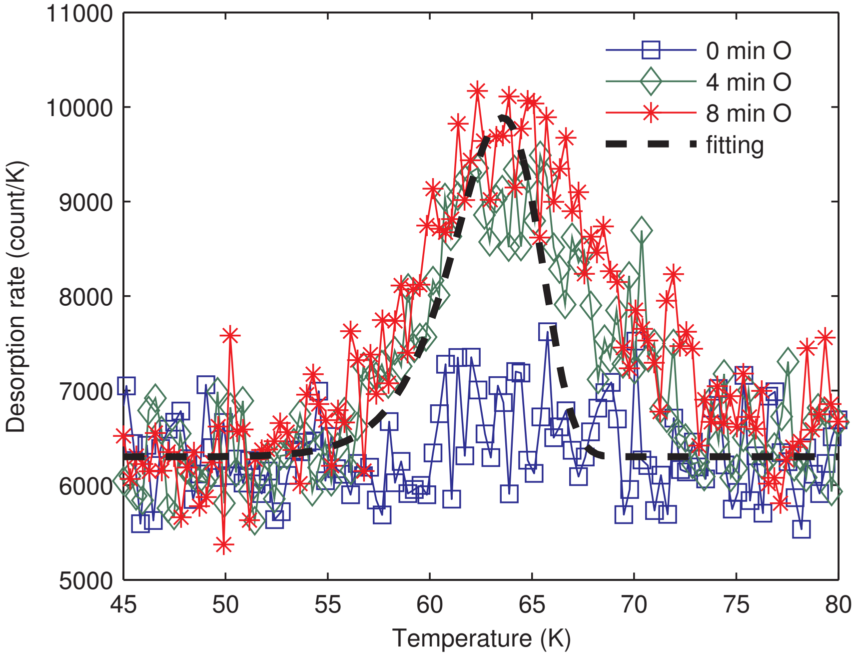

Figure 3.7: Fitting of the mass 16 amu TPD traces after subtraction in the top-right panel (4 min O_3 + 0, 4, 8 min O) of Figure 3.6 using $E_{\mathrm{des}} = 1850$ K.

Table 3.3: Desorption energy of atomic oxygen from porous amorphous water ice and from an amorphous silicate surface.

Surface	Desorption peak temperature	$E_{\mathrm{des}}(\mathrm{O})$
porous water ice	56±2 K	1660±60 K
amorphous silicate	64±3 K	1850±90 K

assumed. In addition to the usual gas phase reactions, oxygen-related grain surface reactions are included to present a relative complete picture of the oxygen chemistry. More details of the model can be found in Hollenbach et al. (2009). The simulation will show the impact of the new atomic oxygen desorption energies obtained in our experiments.

3.4 Conclusions

The desorption energy for atomic oxygen on interstellar dust grain surfaces at low temperature is essential for simulation codes of the chemical evolution of interstellar environments. By indirect measurements via ozone formation experiments and direct measurement of atomic oxygen desorption, we have obtained new values for atomic oxygen desorption energy on ISM related surfaces, even though there have been known technical difficulties found in the past (Jing et al., 2012, 2013). In the indirect method by studying the ozone formation rate on an amorphous silicate surface, the value of atomic oxygen desorption energy is found to be 1760±230 K. In the direct method, atomic oxygen desorption energy has been found to be 1660±60 K and 1850±90 K on porous water ice and amorphous silicate surface, respectively. Models of the chemical evolution of ISM environments using the old estimate (800 K) gave predictions of molecular oxygen abundance in severe disagreement with observations. Our value is in good agreement with an estimate that Melnick et al. (2012) gave to reconcile their own most recent observations of O_2 with modeling predicted abundances. These values should affect most of atomic oxygen related reactions in the ISM.

Chapter 4

Water Formation on Warm Dust Grains

When the surface of a dust grain is at a higher temperature than in dense clouds (e.g., > 20 K), water formation via O_2 hydrogenation is no longer efficient. The OH radical should start to play a more important role. We carried out ozone hydrogenation experiments (H + $O_3 \rightarrow OH + O_2$) on an amorphous silicate surface at 50 K. At this temperature, O_2 does not stay while OH may still reside on the surface. The intermediate product OH can react with atomic/molecular hydrogen to form water. By recording the amount of ozone and the amount of water formed on the surface, we were able to estimate the OH residence time. In addition, the exponential decay of residual ozone on the surface with increasing atomic hydrogen dose was used to calculate the cross-section area of the ozone hydrogenation reaction. Based on this results, we suggest an Eley-Rideal type reaction mechanism for ozone hydrogenation under our experimental conditions.

This chapter is adapted from the following published paper with modifications:
Jiao He and Gianfranco Vidali. "Experiments of Water Formation on Warm Silicates." The Astrophysical Journal 788, no. 1 (2014): 50.

4.1 Introduction

Water acts as a coolant and a tracer in gravitationally collapsing clouds (Neufeld et al., 1995; Mottram et al., 2013) and provides, as the main constituent of ices coating dust grains, a medium for the chemical enrichment of many space environments, from dense clouds to protoplanetary disks (Kristensen & van Dishoeck, 2011; Hogerheijde et al., 2011). It is well-known that gas phase reactions alone cannot account for the abundance of water in the ISM, and reactions taking place on dust grain surfaces must be considered (Hasegawa et al., 1992; Roberts & Herbst, 2002; Du et al., 2012). Following a reaction network put forward by Tielens & Hagen (1982), there are three main routes to form water via hydrogenation of oxygen ($O+H \rightarrow OH$, $OH+H \rightarrow H_2O$), of molecular oxygen ($O_2 \xrightarrow{H} HO_2 \xrightarrow{H} H_2O_2 \xrightarrow{H} H_2O + OH$) and of ozone ($O_3+H \rightarrow OH + O_2$ followed by reactions with H or H_2). A schematic of the reaction network is shown in Figure 4.1. In the past decade, there has been an intense interest in studying in the laboratory which of these reaction paths are most likely to occur in a given space environment. Most of the work was done on model ices (water, oxygen, ozone) at low temperature (less than 30 K). Formation of water using atomic hydrogen and oxygen was studied by Dulieu et al. (2010) and Jing et al. (2011) on a water ice surface and on the surface of an amorphous silicate, respectively. Formation of hydroxyls in silicates via ion implantation was studied by Djouadi et al. (2011). Formation of water via hydrogenation of a molecular oxygen ice was investigated by Ioppolo et al. (2008) and Miyauchi et al. (2008), while Romanzin et al. (2011) and Mokrane et al. (2009) used ozone made in-situ or deposited ozone on an ice to form water by the reaction route $H+O_3$. Oba et al. (2011) studied the formation of water on a 40-60 K substrate through the $OH+OH \rightarrow H_2O_2$ channel.

However, water formation also proceeds in warmer regions; some of it occurs via gas-phase endothermic or ion-atom/molecule reactions (Glassgold et al., 2009; Hollenbach et al., 2012). In warm regions, the O_2 hydrogenation channel in surface reactions is not likely to be important since O_2 leaves the surface of ice at around 30 K. The other two channels (hydrogenation of O and O_3) involve the radical OH: $OH+H \rightarrow H_2O$ or $OH+H_2 \rightarrow H_2O+H$.

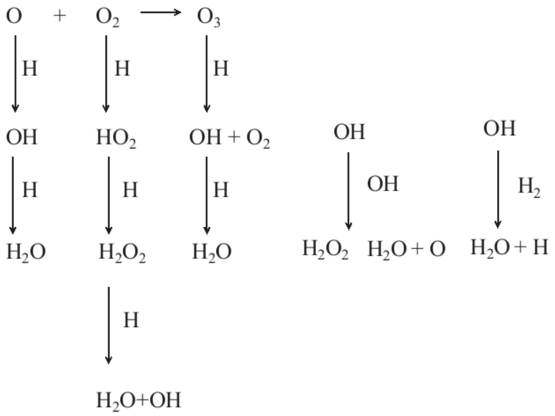

Figure 4.1: A schematic of the water formation routes on grain surfaces.

Therefore it is critical to know what the residence time of OH on grain surfaces is and the mechanisms of reactions on warm grains where the residence time of H or H_2 can be very short.

In diffuse clouds, OH is formed via a series of reactions starting with the O^+ ion (for example: $H^+ + O \rightarrow O^+ + H$, $O^+ + H_2 \rightarrow OH^+ + H$) followed by electron attachment of OH^+ or dissociative recombination of OH_3^+; this chemistry is controlled by the cosmic ionization rate (van Dishoeck & Black, 1986). In hotter (300 K) environments, endothermic reactions ($O+H_2$) play a role (Neufeld et al., 2010). The OH abundance in the gas phase is of the order 10^{-5} - 10^{-6} with respect to hydrogen, depending on the type of environment (Karlsson et al., 2013). Much less is known about oxygen chemistry on grains, although it is recognized that oxygen-bearing molecules produced on grains are an important contributor to the overall chemistry of clouds.

In the gas-grain chemical models for dense clouds of Hasegawa et al. (1992) and Stantcheva et al. (2002), the OH desorption energy was chosen to be 1259 K, which is a value adapted from Allen & Robinson (1977). A simple calculation based on this value predicts that the residence time of OH on a grain surface is less than 0.1 seconds at 50 K if we assume a pre-exponent $\nu = 10^{12}$ s^{-1} in the standard expression $t = \nu^{-1} \exp(E_{\rm des}/k_{\rm B}T)$, where $E_{\rm des}$ is the energy necessary for the molecule to leave the surface (desorption energy) and T is the temperature of the surface. Therefore, with these values, water formation on dust at above 50 K is not efficient if we assume that reactions occur on surfaces with atoms or radicals thermally accommodated to them; this disagrees with astronomical observations which show widespread presence of water in diverse space environments (van Dishoeck et al., 2013).

In this Chapter we report on experiments of water formation on warm (50 K) amorphous silicates. We investigated the formation of water via the OH reaction with H/H_2. OH was obtained by the reaction of O_3 with H. The mechanism of reaction for atomic hydrogen with ozone was quantified and the cross-section for the reaction was measured. This was done in a single set of experiments on the surface of an amorphous silicate film at 50 K via O_3+H/D sequential exposure experiments. The following reactions are of interest:

$$\mathrm{O_3 + H/D \rightarrow OH/OD + O_2} \tag{4.1}$$

$$\mathrm{OH/OD + H/D \rightarrow H_2O/D_2O} \tag{4.2}$$

$$\mathrm{OH/OD + H_2/D_2 \rightarrow H_2O/D_2O + H/D} \tag{4.3}$$

By measuring the destruction rate of ozone through the reaction 4.1, we get the reaction cross-section and thus infer whether atomic hydrogen takes part in the surface reaction via the Eley-Rideal (ER) or hot atom (HA) mechanisms. In studying reactions 4.2 and 4.3, we obtain information regarding the water formation rate and the residence time of OH on grain surfaces.

In the next section the experimental apparatus and measuring methods are presented, followed by the experimental results. In Section 4.4 we present an analysis of the experimental data, from which we obtain estimates of the OH residence time as well as the cross-section of the ozone hydrogenation reaction. The water formation rate is also discussed. In Section 4.5 we explore how our findings can be used to learn about water formation in actual ISM environments.

4.2 Experimental

The experimental setup is similar to that in Section 3.2. The beam fluxes are calibrated by flooding the chamber with D_2, $^{18}O_2$, and $D_2{}^{16}O$, and measuring the chamber pressure and QMS signal simultaneously. The dissociation rates and beam compositions are measured by facing the QMS detector directly to the beam. The dissociation rates for deuterium, hydrogen, and oxygen are measured to be about 45%, 61%, and 25%, respectively, corresponding to a flux intensity of 7.6×10^{11} cm^{-2}s^{-1} and 5.0×10^{11} cm^{-2}s^{-1} for O_2 and O (in the following, "O" refers to ^{18}O unless specified otherwise), 9.3×10^{12} cm^{-2}s^{-1} and 1.5×10^{13} cm^{-2}s^{-1} for D_2 and D, 4.6×10^{13} cm^{-2}s^{-1} and 1.4×10^{13} cm^{-2}s^{-1} for H_2 and H, respectively. The uncertainty due to the variation of the beam flux is less than 10%. In this study we used $^{18}O_2$ instead of $^{16}O_2$; since water is still present as a background gas even in a well-baked chamber, it is important to use isotope labeled gases. This gives us the ability to measure very small amount of water produced on the sample. When dissociating D_2, mass 20 amu is detected in the direct beam with an intensity 1.6% of the D flux. This is due to contamination in the fore-line manifold or in the beam line. The $D_2{}^{16}O$ that forms is subtracted from the observed signals of mass 20 amu.

In temperature programmed desorption (TPD) experiments, the QMS measurement yields of different desorbed species cannot be compared directly unless corrected for QMS ionization efficiency. The ionization efficiency of gas species is inversely proportional to the speed of desorbed molecules $v \propto \sqrt{T/m}$, where T and m are the temperature and mass of the desorbing molecule respectively. T is assumed to be the same as the surface temperature at which desorption peaked. The ionization efficiency also depends on the molecular species. Thus, we perform separate calibration experiments to find out the relative ionization of different molecular species. Without cooling down the sample, the chamber is filled with room temperature gas D_2, O_2, or $D_2{}^{16}O$ to certain pressures and the QMS counts are recorded as a function of pressure. The pressure is measured by a ionization pressure gauge; calibration factors for different gases are applied. The relative detection efficiency is calculated to be

D_2:O_2:$D_2{}^{16}O$=1.39:1.36:1. The fragmentation rates of $H_2{}^{16}O$ and $D_2{}^{16}O$ are measured by sending $H_2{}^{16}O$ and $D_2{}^{16}O$ from the beam and using the QMS to measure the beam compositions. It is found that the measured $^{16}OH/H_2{}^{16}O = 0.27$ while the measured $^{16}OD/D_2{}^{16}O = 0.11$. The fragmentation pattern of $D_2{}^{18}O$ is assumed to be the same as $D_2{}^{16}O$ since the mass difference between ^{18}O and ^{16}O is small. Ozone is formed via the reaction $O+O_2 \rightarrow O_3$ on the surface. The procedure of ozone preparation was discussed in Section 3.2. To summarize: the amorphous silicate sample kept at 30 K is exposed to a dissociated oxygen beam for 20 minutes, then warmed up to 50 K and kept at 50 K for 2 minutes to desorb the remaining O_2. From the calibration procedures in Section 3.2, the amount of ozone formed is estimated to be 0.95 ± 0.1 monolayer. Analysis in Section 3.2 shows that the ozone sample prepared in this method is not mixed with O_2 or O. Ozone (mass 54 amu) can break upon electron impact into O (mass 18 amu) and O_2 (mass 36 amu). The mass 36 amu/mass 54 amu ratio depends on the design and setting of the ionizer in the QMS. For the measurements in this study, the ratio is about 16, so the mass 36 amu amount can well represent the amount of ozone yield. With the sample covered with ozone, we keep the sample at 50 K and expose it to the dissociated hydrogen/deuterium beam for a certain duration. To obtain a reproducible heating slope rate at ozone desorption temperature (it begins at about 60 K), the sample is cooled down to below 30 K and then heated up again by a constant heating power to thermally desorb the reaction products and the residue ozone (measured as mass 36 amu in QMS). A typical sequence of experimental procedures is illustrated in Figure 4.2.

4.3 Results

In Table 4.1 we indicate, for each experiment, the masses of the molecules that were detected and the reactions that could have produced them. Figure 4.3 shows a typical TPD spectrum after the O_3+D sequential experiment. The mass 36 amu ozone peak is centered at around 80 K while all the other masses peak at about 160 K. H_2O_2 and D_2O_2 (mass 38 amu and

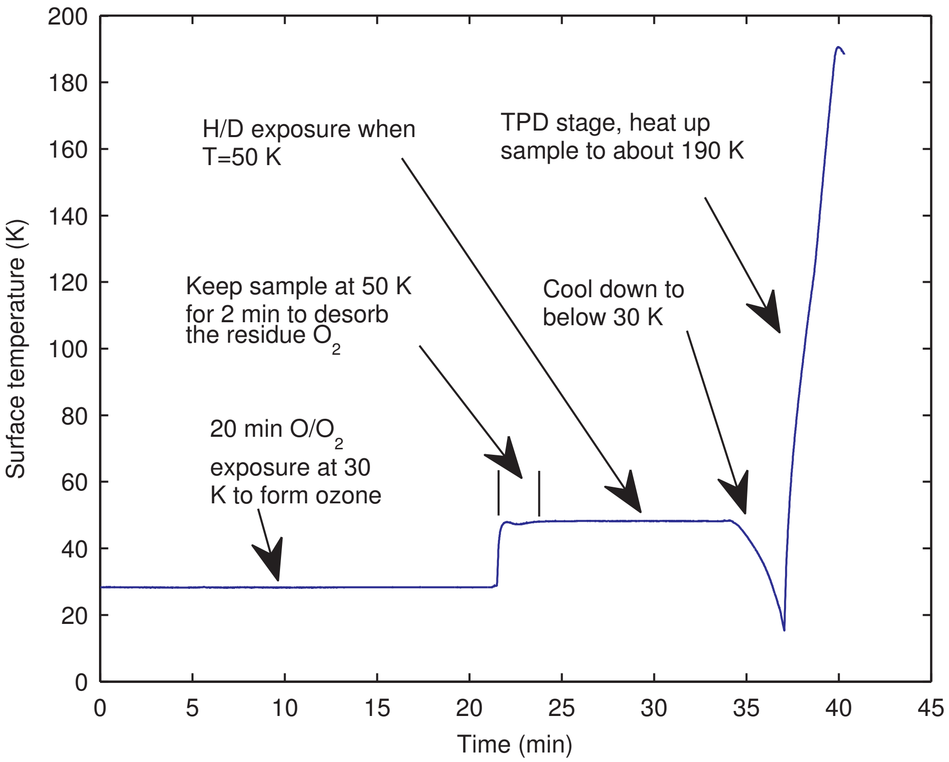

Figure 4.2: Illustration of a typical experimental procedure. The temperature curve is taken from a typical experiment of ozone hydrogenation. In the first stage (T = 30 K) the sample surface is exposed to $^{18}O/^{18}O_2$ beam for 20 minutes. In the second stage the sample is kept at 50 K for 2 minutes with no beam exposure to desorb the residual $^{18}O_2$. In the third stage the sample is cooled down to below 30 K in order to obtain a reproducible heating ramp rate. The last stage is the TPD stage in which the sample is heated up to about 190 K.

mass 40 amu) are checked occasionally, but are not discernible from background. Mass 20 amu and mass 36 amu have a higher background than mass 21 amu and mass 22 amu. The increase of mass 36 amu after 170 K is due to the O_2 desorption from the sample holder.

We repeated the ozone formation procedure (about 0.95±0.1 ML of ozone is formed for each run) but changed the H/D exposure length. Figure 4.4 and Figure 4.5 show TPD yields for different species after sequential deposition of O_3+H and O_3+D respectively. In Figure 4.5 the mass 20 amu contribution from the beam line ($D_2{}^{16}O$) has already been subtracted (see Section 4.2). To better show the trend of mass 20, Figure 4.5 is plotted in log scale.

Table 4.1: Masses recorded for given experiments. In the column "Origin", the source of the molecule is indicated; "frag." indicates it comes from fragmentation in the QMS ionizer. The oxygen isotope ^{18}O was used unless specified. In the origin of mass 21(OD+H_2), the H_2 is from the vacuum background.

Exp.	Mass (amu)	Origin
O_3+H	19	$O_3+H\rightarrow\underline{OH}+O_2$, H_2O frag.
O_3+H	20	$OH+H\rightarrow\underline{H_2O}$, $OH+H_2\rightarrow\underline{H_2O}+H$
O_3+H	36	O_3 frag.
O_3+D	20	$O_3+D\rightarrow\underline{OD}+O_2$, D_2O/HDO frag.
O_3+D	21	$H_2\,^{16}O+D_2\,^{18}O\rightarrow\underline{HD\,^{18}O}+HD\,^{16}O$, $OD+H_2\rightarrow\underline{HDO}+H$
O_3+D	22	$OD+D\rightarrow\underline{D_2O}$, $OD+D_2\rightarrow\underline{D_2O}+D$
O_3+D	36	O_3 frag.

4.4 Analysis and discussion

4.4.1 H/D gas-grain reaction mechanism

When the ozone-covered sample is exposed to the H/D beam, the reaction O_3+H/D→OH/OD+O_2 which has no reaction energy barrier (Mokrane et al., 2009) takes place. The reaction product O_2 desorbs upon reaction because of the very short residence time (Jing et al., 2012). The QMS data recorded in the H/D exposure stage shows that mass 36 amu signal increases above background, which confirms the desorption of O_2 upon formation. The ozone destruction rate is proportional to the ozone coverage, H/D flux, and the reaction cross-section of H/D with O_3. The first two are obtained from calibrations. The cross-section is obtained as follows. We assume that at t=0 the ozone coverage on the surface is $\theta(0) = \theta_0$. After a certain H/D exposure time t the ozone coverage becomes:

$$\theta(t) = \theta_0 \exp(-\phi\sigma t) \tag{4.4}$$

More details can be of this expression is in Section 1.6. In Figure 4.6, the ozone yields are plotted in $\log_e$ scale as a function of H/D exposure. The slope of the two linear fits are

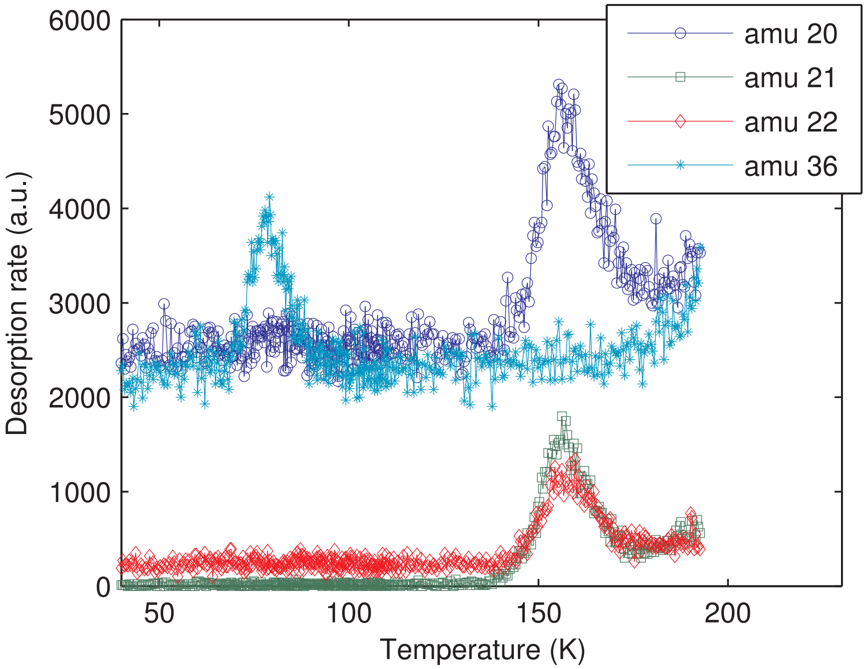

Figure 4.3: A typical TPD spectrum after $^{18}O_3$+D sequential deposition as illustrated in Figure 4.2. Masses 20, 21, 22, and 36 amu are OD, HDO, D_2O, and O_2 (ozone fragmentation) respectively. The surface temperature during D deposition was 50 K.

-0.14 ± 0.02 minute^{-1} and -0.085 ± 0.008 minute^{-1} for H and D, respectively. Using the flux calibration presented in Section 4.2, the cross-sections σ for H and D are calculated to be: $\sigma_H = 1.6 \pm 0.3$ Å^2 and $\sigma_D = 0.94 \pm 0.09$ Å^2, respectively. We notice that σ_H is 60% higher than σ_D; this could be caused by a small reaction energy barrier for the reaction H/D+O_3, although Mokrane et al. (2009) has claimed that there is no discernible barrier.

These two cross-sections are smaller than the typical size of an ozone molecule. In gas-grain modeling, the grain surface is usually modeled by a lattice grid of adsorption sites with a typical site density of $\rho = 1 \times 10^{15}$ cm^{-2}. Molecules or atoms make discrete random-walk steps on the surface. In each step, an atom or molecule jumps to one of the four nearby adsorption sites. The area of each adsorption site is $\rho^{-1} = 10$ Å^2, which is much larger than the cross-section obtained above. We thus conclude that at 50 K on amorphous silicate surfaces H/D is more likely to react with ozone via direct collision (the Eley-Rideal mechanism) instead of the hot-atom mechanism.

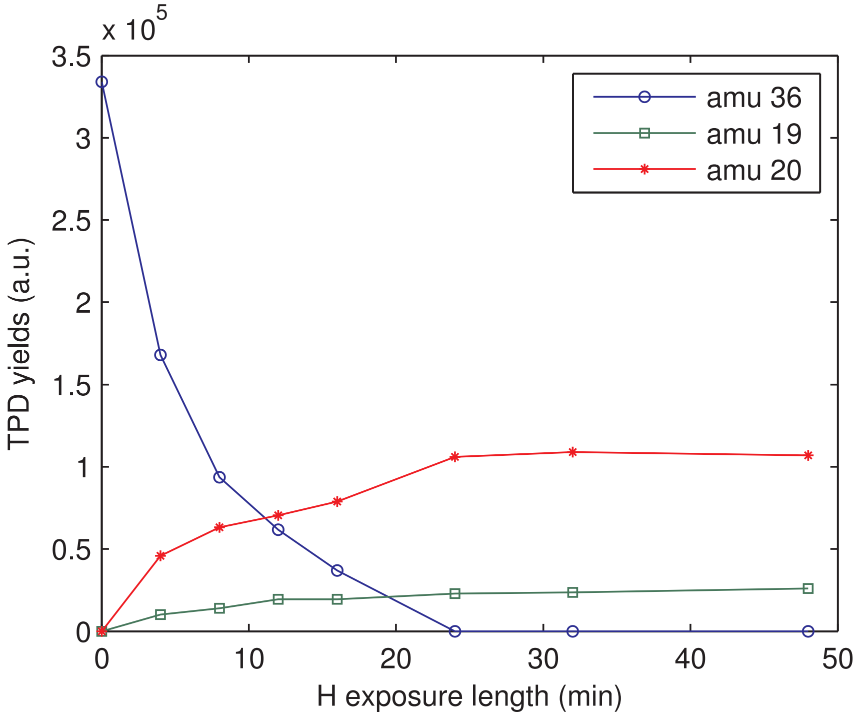

Figure 4.4: TPD yields of masses 19, 20, and 36 amu for $^{18}O_3$+H sequential deposition experiments as illustrated in Figure 4.2. The H exposure lengths were 0 min, 4 min, 8 min, 12 min, 16 min, 24 min, 32 min, and 48 min, respectively. The surface temperature during H deposition was 50 K.

4.4.2 Water formation and OH/OD desorption

A qualitative analysis of OH/OD residence time can be obtained. In Reaction 4.1, the product OH/OD must stay on the surface until another H/D/H_2/D_2 arrives (Reactions (4.2) and (4.3)), otherwise no water can be formed; therefore, OH/OD should have a desorption peak temperature higher than 50 K in order to remain on the surface. Thus, we see that the estimate of the desorption energy by Allen & Robinson (1977) (1259 K) does not agree with our experiments. In that case, OH or OD would desorb from the surface quickly at 50 K (residence time $\sim$ 0.1 second).

The attribution of the measured TPD spectrum is not easy because of the existence of different isotopes and of fragmentation in the QMS. Unfortunately, infrared spectroscopy is of no help here because of the low coverage and IR cross-sections. Romanzin et al. (2011) deposited thick ozone layers before sending in H/D and the infrared signal was strong

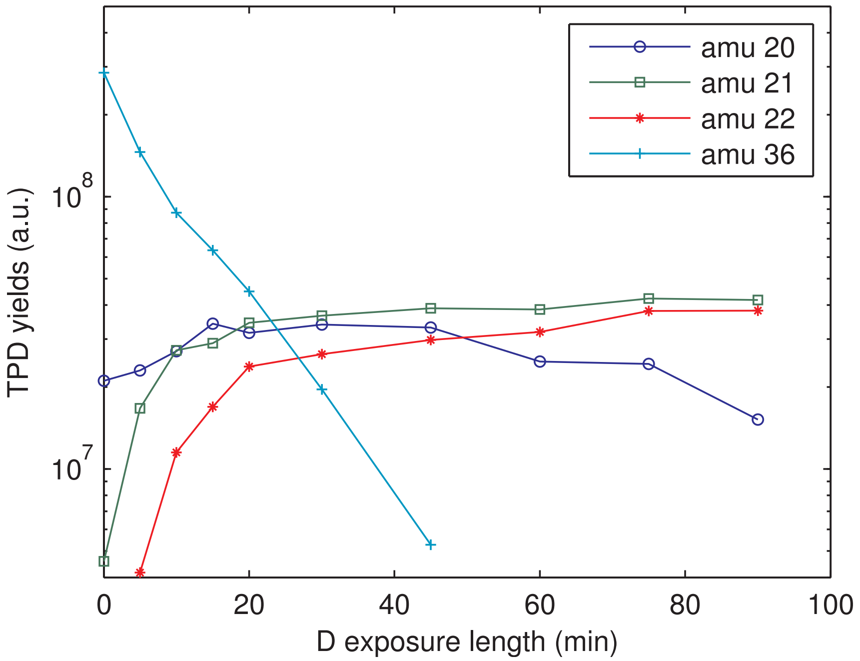

Figure 4.5: Log scale plot of TPD yields of masses 20, 21, 22 and 36 amu for sequential deposition experiments $^{18}O_3$+D as illustrated in Figure 4.2. The D exposure lengths are 0 min, 5 min, 10 min, 15 min, 20 min, 30 min, 45 min, 60 min, 75 min, and 90 min, respectively. The mass 20 amu contribution from the beam line ($D_2\,^{16}O$) has already been subtracted from the yields, although there is still some contamination from the vacuum chamber background, as can be seen from the fact that the mass 20 amu trace does not start from 0.

enough. But hyrogenation of ozone ice is more complicated because of the interference of O_2 hydrogenation channel and the additional uncertainty introduced by H/D penetration. We thus decided to work at sub-monolayer coverage.

In Figure 4.4, the ratio of yields mass 19 amu/mass 20 amu is 0.24±0.03, which is similar to the fragmentation pattern of water in the QMS obtained by measuring the water beam. We thus conclude that all the mass 19 amu signal in Figure 4.4 is due to H_2O fragmentation in the QMS; there is almost no OH direct desorption in the TPD stage. This indicates that the conversion from OH to water is very efficient. The desorption of O_2, H_2O, and OH were also measured in the H exposure stage. There was a slight increase in the O_2 signal but not a discernible H_2O or OH signal.

The interpretation of the O_3+D experimental results in Figure 4.5 is more complicated.

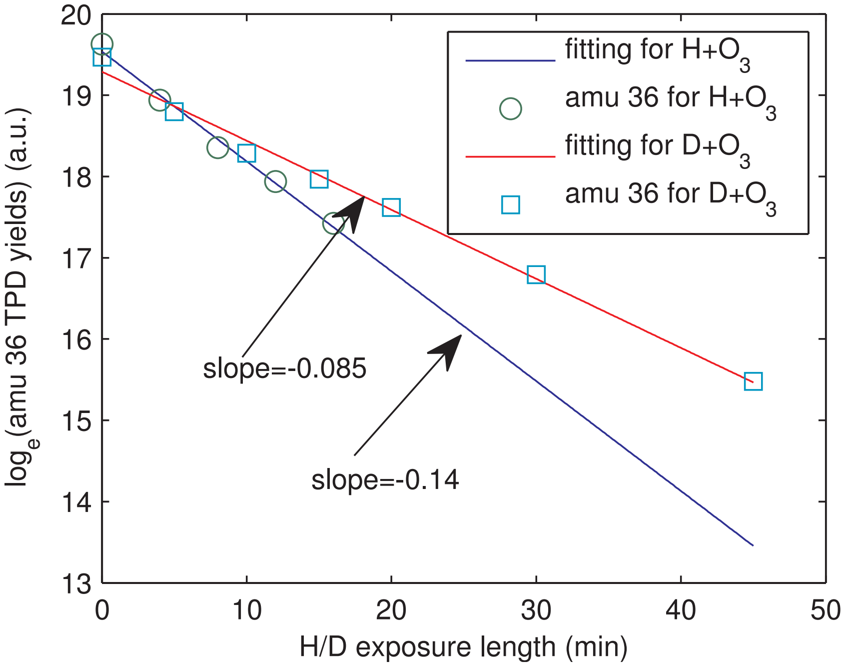

Figure 4.6: Log plot of the ozone (mass 36 amu) TPD yields as a function of H/D exposure time. The two straight lines show linear fits.

The mass 20 amu which peaks at around 160 K may be due to three sources: 1) OD formed from Reaction (4.1), 2) fragmentation of HDO or D_2O in the detector, and 3) $D_2{}^{16}O$ coming from the beam line. The last one is already subtracted from the TPD yields in Figure 4.5. We now consider scenarios 1) and 2). There are two possibilities:

(1) If at least part of the mass 20 amu signal in Figure 4.5 is due to OD desorption, then the desorption peak temperature of OD should be the same as the water desorption peak, centered at 160 K. The desorption energy is calculated to be around 410 meV (4760 K). By comparing Figure 4.4 and Figure 4.5 one can see that there is a strong isotopic effect between H_2O and D_2O formations. In OH+H_2/H, the reaction proceeds very fast so that no OH desorption is seen in the TPD stage, while in OD+D_2/D/H_2 (H_2 is from the background), unreacted OD (mass 20 amu) desorbs from the surface directly. This indicates a strong isotopic effect. OH+H and OD+D reactions are barrier-less and do not have a significant isotopic effect. Only OH+H_2 has known isotopic effects (Oba et al., 2012). Thus,

$OH+H_2$ should play an important role in the water formation under the assumption of this paragraph.

(2) If none of the atomic mass 20 signal in Figure 4.5 is due to OD desorption, the exact value of OD/OH desorption energy is unavailable. However, a lower boundary can be estimated. We focus on the O_3+H experiments shown in Figure 4.4 and assume that OD requires the same desorption energy as OH. TPD spectra of different species cannot be compared directly, but a correction based on the speed of the desorbing species and on the cross-section for ionization in the detector is needed. Ozone (mass 54 amu) desorption peaked at around 80 K while water (mass 20 amu) desorption peaked at around 160 K. Taking into account the QMS detection efficiencies and considering that speed is correlated with temperature and mass as $v \sim \sqrt{T/m}$ (see Section 4.2), we have:

$$\frac{Y_{\mathrm{corr}}(\mathrm{water})}{Y_{\mathrm{corr}}(\mathrm{ozone})} = \frac{Y(\mathrm{H_2O})\sqrt{160/20}}{Y(\mathrm{O_3}) \cdot \sqrt{80/54}/1.36} = 3.15\frac{Y(\mathrm{H_2O})}{Y(\mathrm{O_3})} \tag{4.5}$$

where Y_{corr} represents corrected yields while Y represents measured yields. The factor 1.36 is due to the difference in ionization ratio between O_2 and water. Thus, the water (mass 20 amu) yield needs to be multiplied by 3.15 before comparing it with the ozone (mass 36 amu) yield. According to the data in Figure 4.4 and a simple calculation we see that the amount of water formed is 1.0 ± 0.1 times the amount of ozone consumed, the error bar 0.1 is coming from an estimate in the uncertainty in the QMS measurements. Thus at least 90% of the OH is converted to water before desorption. In order to calculate the lower boundary of OH residence time at 50 K, we assume that all the H/H_2 can react with OH with 100% probability as long as H/H_2 can strike an OH directly (ER mechanism), and the reaction between H/H_2 and OH has the same cross-section as O_3+H. After OH is formed and remains on the surface for a time t, the fraction of OH that is not converted to water is $p(t) = \exp(-\phi(\mathrm{H+H_2})\sigma t)$, where $\phi(\mathrm{H+H_2})$ is the sum of H and H_2 beam flux. Letting $p(t) = 0.1$ and using the values of the flux of H and H_2, the residence time is calculated to be $t = 4$ minutes. This is the minimum required average residence time for OH on surface at 50 K in order to account for the water yields. The corresponding desorption energy is then at least 143 meV (1660 K).

Dulieu et al. (2013) recently did a series of experiments to study the role of OH and OD in water formation on dust grain analogs. Experiments were done on a silicate sample kept in the range of 10 to 45 K. They deposited O_2 at 10 K and then irradiated the sample with D atoms. They observed that some water (D_2O) desorbed during the irradiation with H or D, although the signal was only two times the noise level. After irradiation they conducted a TPD and observed the desorption of O_2, D_2O and D_2O_2, which are intermediate products in the formation of water through the $H+O_2$ reaction. They did a similar experiment by depositing O_3 on the silicate surface and then by irradiating the sample with H or D at 45 K, which is higher than the temperature at which O_2 leaves the surface. They claimed that the H_2O or D_2O desorbed during irradiation and that there was no water left when they did a TPD experiment. This disagrees with our results. In our experiments we also recorded all the reaction products which may desorb upon formation. The O_2 signal increases above the background by about twice the noise level while the signal change for other species are not discernible. The difference between these two sets of experiments may be due to the different oxygen isotopes used in the experiments. In our experiments ^{18}O is used in place of the much more naturally occurring ^{16}O, so that the $H_2{}^{18}O$ (mass 20 amu) formed on the surface has a background contamination 10 times less than $H_2{}^{16}O$ (mass 20 amu) and the signal to noise ratio in our experiments is improved by at least 10 times compared with the experiments by Dulieu et al. where ^{16}O was used. In addition, Dulieu et al. compared O_3+H at 45 K with O_2/O_3+H at 10 K, the latter may have a significant condensation of $H_2{}^{16}O$ from the vacuum chamber onto the sample surface, which could be confused with the $H_2{}^{16}O$ formed on the surface, thus making the comparison less convincing.

4.5 Astrophysical implications

There has been rapid progress in the laboratory to study the various routes to formation of water on a variety of surfaces of materials of interest to the astrochemistry of the ISM. Most of the studies were concentrated on the feasibility of reaction paths on ices at low temperature. However, to predict how much water is produced in a given astrophysical environment, one needs to know the water formation rate on surfaces and whether or not water is injected in the gas-phase. In this Chapter, we explored the routes of water formation on "warm" grains. On such grains, hydrogenation of O_2, one of the channels most considered today, is no longer viable because O_2 leaves the surface of grains at around 30-35 K. At higher temperatures, the key to water formation is the radical OH. In this Chapter, we looked at the formation of water via the reaction OH/OD+H/D/H_2/D_2 on a silicate surface at 50 K. OH/OD was obtained by O_3 hydrogenation/deuteration. We measured the cross-section for O_3+H/D to be $\sigma_{\mathrm{H}} = 1.6 \pm 0.3$ Å^2 and $\sigma_{\mathrm{D}} = 0.94 \pm 0.09$ Å^2, respectively, and suggested that the mechanism of reaction is direct Eley-Rideal instead of hot-atom.

In our O_3+H/D experiments, the results show that water does not desorb immediately upon formation, a conclusion that differs from the one of Dulieu et al. (2013). Our analysis suggests that OH/OD is likely to desorb in a TPD experiment at the same temperature as water does. In this case, the energy for desorption of OH/OD is 410 meV (4760 K). However, because of the ambiguity of the detection (see Appendix of He & Vidali (2014)), we cannot exclude the possibility that the desorption energy is smaller. In any case, it is larger than 143 meV (1660 K), which is more than 400 K higher than the previously accepted value of Allen & Robinson (1977); this latter value is used in codes simulating the chemical evolution of interstellar clouds (Hasegawa et al., 1992; Stantcheva et al., 2002; Garrod et al., 2008). Therefore, this new found value of OH binding energy could extend the effective water formation temperature on dust grains to much higher than 50 K. It would be interesting to apply the new value to chemical models of water formation in both protoplanetary disks (Glassgold et al., 2009) and star-forming regions (Garrod et al., 2008).

Experimentally, more work is needed to characterize the OH residence on grain analogs and to quantitatively evaluate the relative contributions of OH+H and OH+H_2 reactions to the formation of water on warm grains. Theoretically, formation rates of water on warm grains as deduced from experiments should be compared with photodissociation, photodesorption, energetic charged particle interactions and competing reactions that would influence the overall H_2O production, desorption and destruction rates.

Chapter 5

Formation of Hydroxylamine on Dust Grains via Ammonia Oxidation

Hydroxylamine is an important precursor to glycine. Its formation is the focus of this chapter. The efficiency of the ammonia oxidation reaction $NH_3 + O \rightarrow NH_2OH$ is studied by ammonia and atomic oxygen sequential deposition TPD experiments. First, ammonia molecules are deposited onto a amorphous silicate surface. Then, the ammonia molecules are exposed to an atomic oxygen beam produced by a radio-frequency dissociation source. With various atomic oxygen doses, the amount of residual ammonia and newly formed reaction products on the surface are measured by the QMS in the TPD stage. Therefore the reaction efficiency can be estimated. The ammonia oxidation reaction is found to be efficient under our experimental conditions and could be the formation mechanism of hydroxylamine in the ISM.

5.1 Introduction

Hydroxylamine (NH_2OH) has been suggested as an important precursor to amino acids such as glycine. Both experimental and theoretical studies (Blagojevic et al., 2003; Snow et al., 2007) have shown that hydroxylamine in its protonated form can react in the gas phase with acetic and propanoic acids to yield protonated glycine (the simplest non-chiral amino acid) and protonated alanine (the second simplest and chiral amino acid). The recent discovery of glycine in cometary samples returned by the Stardust mission also suggests the formation of hydroxylamine and glycine in the ISM. As acetic acid has been observed in various environments, the detection of hydroxylamine, though unsuccessful so far (Pulliam et al., 2012), is suggested to be plausible. The existence of hydroxylamine has also been supported by various ISM models (Garrod et al., 2008; Garrod, 2013).

One question still under debate is how hydroxylamine is formed. Nishi et al. (1984) proposed that NH_2OH can be formed via UV irradiation of water and ammonia binary ice:

$$\mathrm{NH_3} + \mathrm{H_2O} + h\nu \rightarrow \mathrm{NH_2} + \mathrm{H} + \mathrm{H_2O} \rightarrow \mathrm{NH_2OH} + \mathrm{H_2} \tag{5.1}$$

A similar formation route via energetic electron irradiation of water and ammonia ice has been experimentally studied by Zheng & Kaiser (2010). This study suggests that energetic processes within ice mantles could be responsible for the NH_2OH formation. Non-energetic processes could also lead to the formation of hydroxylamine. To account for the NH_2OH formation in dark clouds, Charnley et al. (2001) suggests that in the gas phase nitrogen atoms react with OH to form NO ($N + OH \rightarrow NO + H$); NO then accretes on a grain surface to react with atomic hydrogen coming from the gas phase. After a three steps hydrogenation, NO can be converted to NH_2OH. Observations of NO both in the gas phase and on dust grains surfaces (Allamandola & Norman, 1978; Akyilmaz et al., 2007) support this formation route. In addition, NO hydrogenation has recently been studied in the laboratory by Congiu et al. (2012a); Fedoseev et al. (2012) on both submonolayer and multilayer regimes. The reaction energy barriers for the reactions from NO to NH_2OH were claimed to be negligible without a sound knowledge of the reaction rates and branching ratios of each hydrogenation step involved.

Ammonia is another important N-bearing molecule in the ISM with an observed abundance comparable to or higher than that of NO (Takano et al., 2013). Complex nitrogen chemistry is also likely to start with NH_3. In the ISM, oxygen is the third most abundant element (see Table 1.1). Most of oxygen is in the gas phase, while the rest is in H_2O, CO, and in silicates (Whittet, 2010). Much earlier, from about 1960 to mid-1980s, the NH_3+O reaction has been the subject of numerous experiments reviewed by (Cohen, 1987). They were performed at moderate temperature (450 to 850 K) in flowing and static systems (Perry, 1984) (Baulch et al., 1984) where ground state $O(^3P)$ is obtained by laser photolysis, at higher temperatures (850 to 2200 K) in flames, (Fenimore & Jones, 1961) or in shock tube experiments (Fujii et al., 1986). Even if such a reaction has never been studied at very low temperature, it has been proposed that the excited NH_3O intermediate could rearrange to give stable hydroxylamine NH_2OH (Baulch et al., 1984). In this chapter we carry out laboratory measurements to study the reaction between NH_3 and atomic oxygen on grain surface at low temperature.

5.2 Experimental

Experiments are performed in a similar experimental setup as that of Section 3.3. Ammonia molecules and atomic oxygen are deposited successively from the molecular beam line onto the amorphous silicate sample. Molecules formed on the surface are measured in the TPD stage by the QMS. Below we describe the beam flux calibration and experimental procedures.

5.2.1 Beam flux calibration

The beam fluxes are calibrated using similar techniques described in Section 2.4 and are illustrated here briefly. With the the amorphous silicate sample kept at 70 K, ammonia gas is introduced from the molecular beam line. The gas flow is set to 0.3 sccm on the mass flow controller. After ammonia exposure, the sample is cooled down to below 40 K and then heated up at 1 K/s to about 200 K to do a TPD. In both ammonia exposure stage and TPD stage, the gas phase molecules are measured using the QMS. Since ammonia fragments in the QMS ionizer, both mass 17 amu (NH_3) and 16 amu (NH_2) are measured. The fragmentation of ammonia into NH/N (mass 15/14 amu) is found to be negligible by direct beam measurements. A series of TPD experimental runs with different ammonia doses are performed. The TPD spectra are shown in Figure 5.1. We calibrate the NH_3 coverage by analyzing the shape of the TPD profile. In the submonolayer region[1], as the coverage of NH_3 increases, the TPD peak temperature should shift to lower values, because in the low coverage region molecules are likely to occupy the deep sites (higher desorption energies). As the deep sites get filled up with increasing exposure, the TPD profile and peak temperature shift to lower temperatures (see Section 6). In the multilayer region, the TPD spectra should show a common leading edge (Kolasinki, 2008), which is a typical first order desorption behavior. The trend of TPD traces shown in Figure 5.1 is in agreement with the one obtained by Bolina et al. (2005) for NH_3 desorption from a graphite surface. With the current experimental settings, 1 ML NH_3 coverage is achieved by 2 minutes exposure with 0.3 sccm gas flow. Thus the NH_3 flow is 0.5 ML/minute, or equivalently, 5×10^{14} $cm^{-2}min^{-1}$, assuming 1 ML $\sim 10^{15}$ cm^{-2}. Following the procedures as described in Section 6, the desorption energy distribution of NH_3 from amorphous silicate surface can be obtained by direct inversion of the 1 ML trace in Figure 5.1. The resulted distribution is shown in the inset of Figure 5.1. Additional TPD runs are performed at a surface temperature of 10 K, 30 K, and 50 K. They show almost identical TPD curves as the one at 70 K. This suggests that the sticking of ammonia on the silicate surface at 70 K is unity, and the desorption rate at 70 K is negligible.

In the atomic oxygen exposure, the O_2 gas flow passing through the flow controller is set to 0.1 sccm. At this flow the dissociation rate of O_2 is measured to be 42%. The calibration of oxygen flux needs to be done differently from ammonia because O_2 is volatile and the sticking is not necessarily unity. The direct beam intensities of O_2 gas at both

---

[1] Here a layer is actually an equivalent layer, since it is unclear whether ammonia would form clusters or islands on the surface. Little experimental evidence support the existence of clusters or islands.

0.3 sccm and 0.1 sccm are measured. Since it is known that 0.3 sccm corresponds to 0.5 ML/minute, the flow at 0.1 sccm can be calculated correspondingly. The O_2 flow at 0.1 sccm is about 0.34 ML/minute (3.4×10^{14} cm^{-2}minute^{-1}). When the RF is on, the beam intensities of O and O_2 are 0.29 ML/minute (2.9×10^{14} cm^{-2}minute^{-1}) and 0.20 ML/minute (2.0×10^{14} cm^{-2}minute^{-1}), respectively. With the radio frequency (RF) power on and the oxygen sent into the dissociation source, beam contamination is checked. The main contaminant is NO (mass 30 amu) due the small leak of air into the dissociation source. The NO (mass 30) signal is less than 3% of the O signal, which is trivial in the context of the experiments performed here.

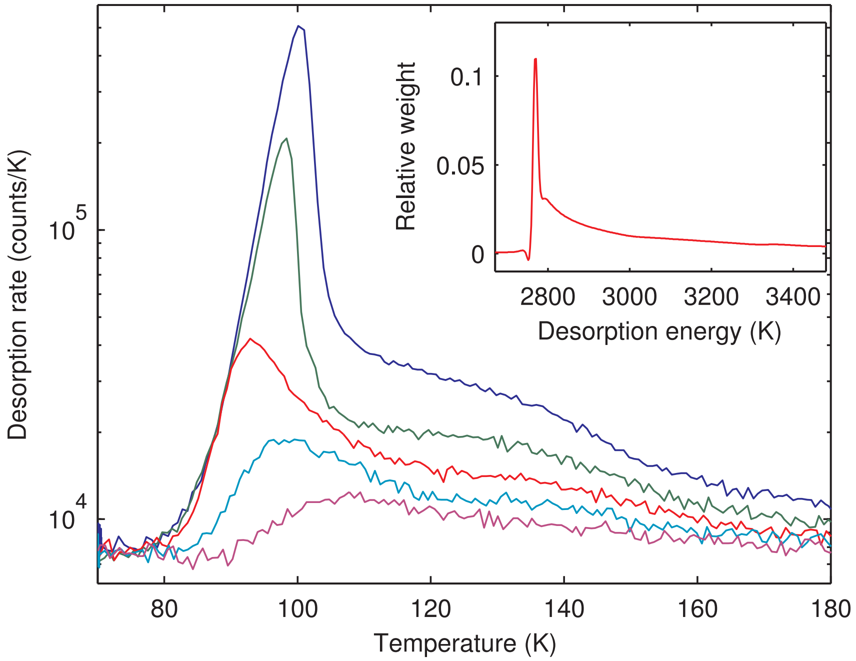

Figure 5.1: TPDs with different exposure of NH_3 at 70 K. The exposure times are from bottom to top, 0.5, 1, 2, 4, and 8 minutes, respectively. The desorption energy distribution of NH_3 calculated from the 2 minutes exposure curve (1 ML deposition) is in the inset.

5.2.2 Experimental procedures

The ammonia oxidation reactions were studied in ammonia and atomic oxygen sequential exposure TPD experiments. The surface was covered with ammonia before introducing atomic oxygen. Two ammonia coverages were used, 2 ML and 1/4 ML, representative of multilayer coverages and submonolayer coverages. After preparation of the ammonia sample, the residual ammonia in the beam line and dissociation source was cleaned by flushing the beam line several times using oxygen. This ensures that almost no ammonia was mixed with oxygen. The sample temperature in the exposure stage was chosen to be 70 K so that $O/O_2/O_3$ does not stick onto the surface while the sticking of NH_3 is unity. After the exposure stage, the surface was cooled down to below 40 K and then heated up linearly at 1 K/s to above 320 K to desorb species from the surface. The QMS recorded simultaneously the signals of various masses during both exposure and TPD stages. Figure 5.2 shows the TPD spectra of a typical experimental run.

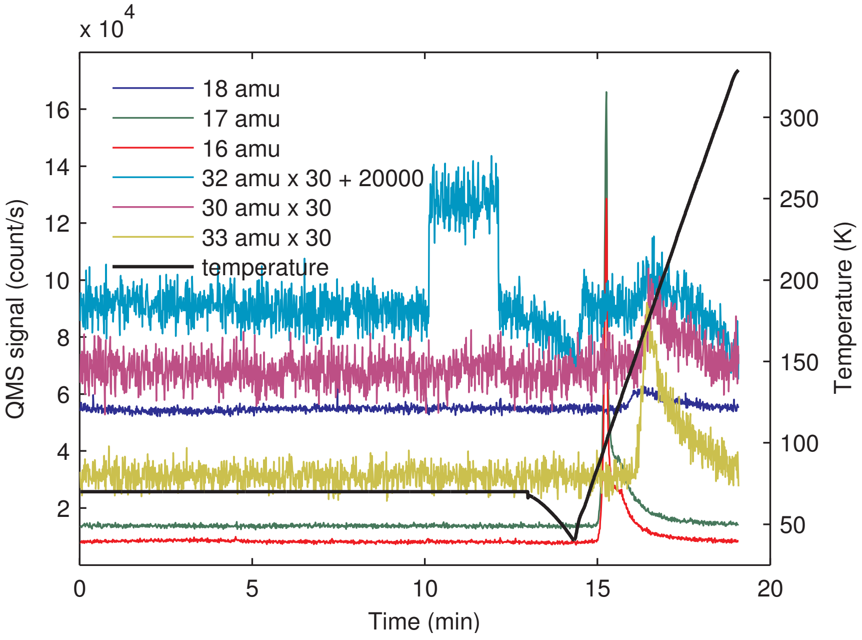

Figure 5.2: A typical TPD of a NH_3 + O sequential exposure experiment at 70 K in which the QMS records simultaneously multiple signals. The temperature ramp (black line) shows that after the exposure is terminated, the sample is cooled to 40 K before the heating is started.

5.3 Results and analysis

5.3.1 Multilayer NH_3 + O

In the NH_3 + O sequential exposure TPD experiments, mass 16, 17, 18, 30, 32, and 33 amu were measured by the QMS, see Figure 5.2. Mass 16 amu is due to the fragmentation of NH_3 in the QMS ionizer; mass 17 amu is due to NH_3 and fragmentation of H_2O; mass 32 amu is due to O_2 and fragments of O_3. Mass 30 amu could be due to NO from the beam line (but the amount is small), or fragments of NH_2OH; mass 33 amu could be due to NH_2OH. HO_2 has the same mass but it is unlikely to be there because of the lack of detection of the products it fragments into. The mass 33 amu peak centered at around 180 K is accompanied by mass 30 amu and very small signals with masses 16, 17 and 32 amu at the same temperature; this suggests that the mass 33 amu peak at 180 K is due to NH_2OH. This agrees with the TPD peak attribution in Congiu et al. (2012b) (in the range of 160-200 K, peaking at $T\sim 190$ K) obtained in an NO hydrogenation experiment and confirmed by infrared measurements (RAIRS). Mass 18 amu is due to water.

Figure 5.3 shows the mass 17 amu (NH_3) signal after depositing various doses of O on top of 2 ML (4 minutes exposure) NH_3. As the O exposure time increases, the NH_3 peak decreases and the peak position also shifts to higher temperatures. This is because the top layer of NH_3 is gradually converted to NH_2OH or other products, thus hindering the desorption of NH_3 molecules underneath. After about 6 minutes of O exposure, the first peak almost disappears, indicating the top layer of NH_3 is almost all converted to NH_2OH or other products.

In Figure 5.4 two desorption peaks, peak A and peak B, are visible. Peak A shows up at O exposure as low as 0.5 minute. This indicates that the ammonia oxidation reaction is efficient. As the O exposure increases from 0 to 4 minutes, the area of peak A increases at first, but then it decreases from 4 minutes to 16 minutes of O exposure. Peak A is followed, at larger O exposures, by peak B at $\sim$ 260 K. Notice that peak B starts to appear at 4

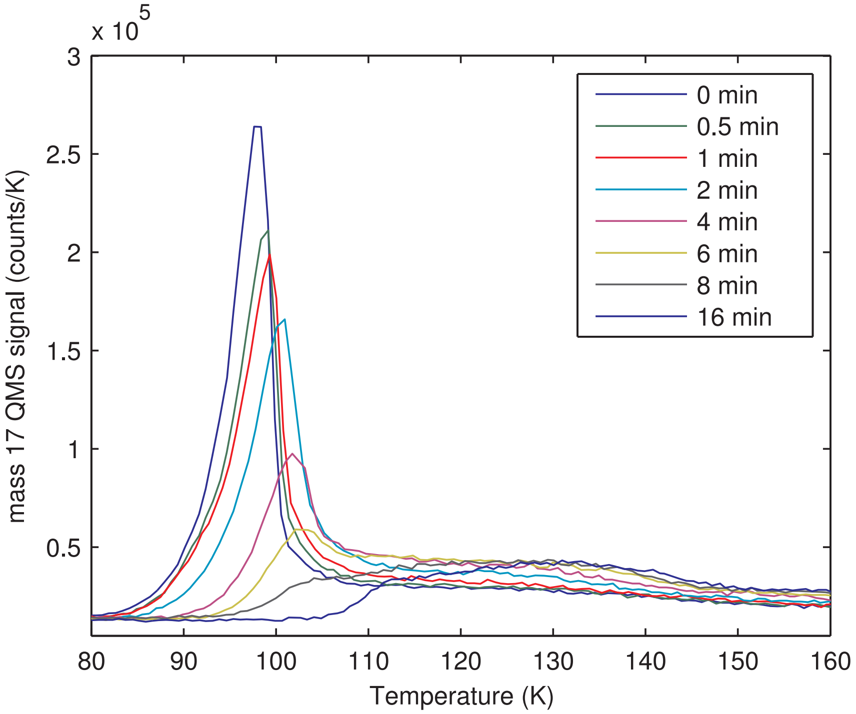

Figure 5.3: Mass 17 QMS signal of the TPD from an ice consisting of NH_3 (4 minutes) followed by exposure to various doses of O at 70 K.

minutes of O exposure time at the expense of peak A. As mentioned above, peak A falls in the temperature range of the TPD mass 33 amu peak obtained by Congiu et al. (2012b). Therefore we attribute peak A to the desorption of NH_2OH.

To find out what peak B represents, we show in Figure 5.5 a comparison of TPD traces for various masses for 2 ML of NH_3 + 8 or 16 minutes of O exposure, see left and right panels of Figure 5.5, respectively. Peak A and peak B are marked by vertical lines. In both panels of Figure 5.5, peak A (see trace of mass 33 amu) is accompanied by desorption of mass 30 amu, 17 amu, and 16 amu, while this is not true for peak B. This suggests that peak B is not due to NH_2OH. It could be the product of a fragmentation of a dimer (Del Bene, 1972) or of an oxidation product of NH_2OH. At about 280 K, there is a peak C showing up for mass 30 amu, 17 amu, and 16 amu, but only when the O dose is high (16 minutes of O exposure), see right panel of Figure 5.5. It could be due to a yet unidentified product formed in a further oxidation of NH_2OH. Peak B and peak C differs in both position and shape, therefore they

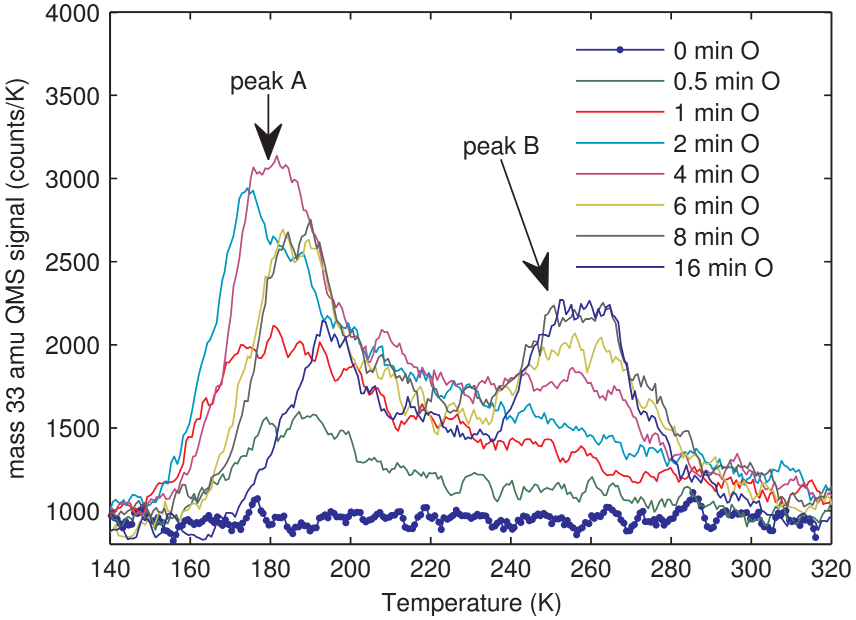

Figure 5.4: QMS mass 33 amu signal of the TPD from an ice consisting of NH_3 (4 minutes) followed by various doses of O at 70 K.

should be attributed to different species.

5.3.2 Submomolayer NH_3 + O

Experiments were also carried out at submonolayer NH_3 coverage. We exposed the sample to NH_3 for 0.5 minutes, or about 1/4 of a layer. This was followed by exposure to O. Mass 16 amu was chosen to represent the NH_3 amount because the mass 17 amu signal has a significant contribution from water fragmentation when the NH_3 signal is weak. The integration of TPD areas of mass 16 amu is shown in Figure 5.7. With O exposure from 0 minute to 2 minutes, the amount of NH_3 follows more or less an exponential decay. This is because when the O amount is small, oxidation dominates and the NH_3 destruction rate is proportional to the NH_3 amount. With a further increase in O exposure, the NH_3 decay does not follow a simple exponential decay anymore because of the possible secondary reactions. In Figure 5.7, a straight line is fitted to the $\log_e$ plot from 0 to 2 minutes. The slope is -0.46 ± 0.06 minute^{-1}. In an exponential decay, the amount of NH_3 on the surface should

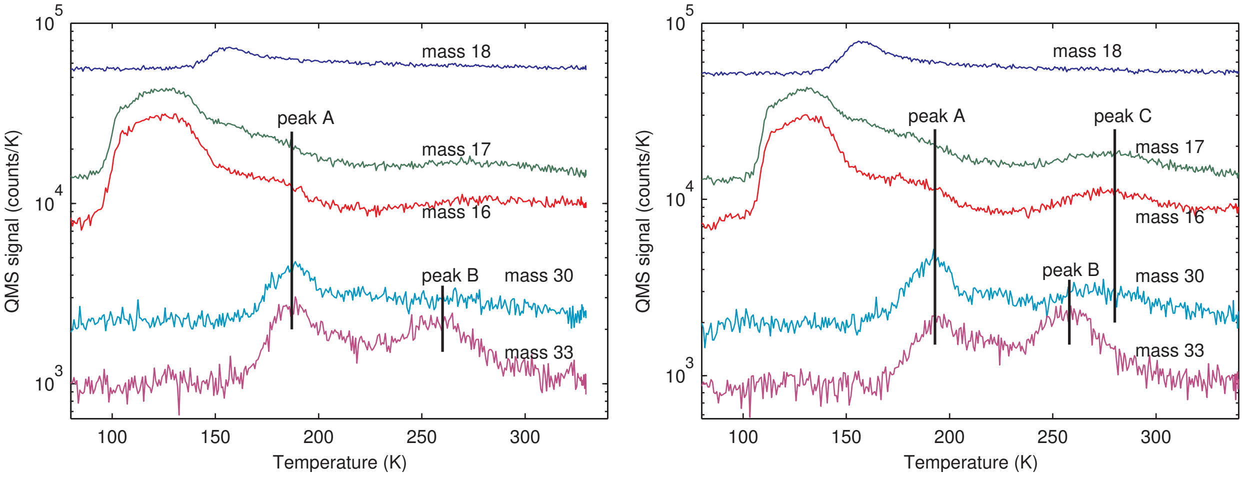

Figure 5.5: QMS signal of the TPD from 2 ML of NH_3 + 8 (left) and 16 (right) minutes of O exposure.

follow $\exp(-\sigma\phi t)$, where σ and ϕ are the reaction cross-section area and the beam flux, respectively. From it, we obtain the cross section $\sigma = -slope/\phi = (1.6 \pm 0.2) \times 10^{-15}$ cm^2 .

5.3.3 Reaction efficiency of NH_3 + O

The reactions that take place on the surface are likely to be multi-step oxidation processes. In typical ISM conditions, the atomic oxygen dose is much less then 1 ML, thus the ensuing reactions after the first step are irrelevant. Therefore we focus on the first oxidation:

$$NH_3 + O \rightarrow NH_2OH \tag{5.2}$$

When the surface is fully covered with NH_3 and the surface temperature is 70 K, the residence time of O is short, O is likely to react with NH_3 via the Eley-Rideal mechanism. Based on prior experiments (Chapter 3), at 70 K the residence time of atomic oxygen on water ice is negligible. We assume that the binding energy of oxygen on ammonia ice is close to the same value on water ice—a reasonable assumption—and the residence time of O on it is also negligible. We also assume that all the reactions take place during the exposure stage instead of the TPD stage because at 70 K the mobility of species should be relatively

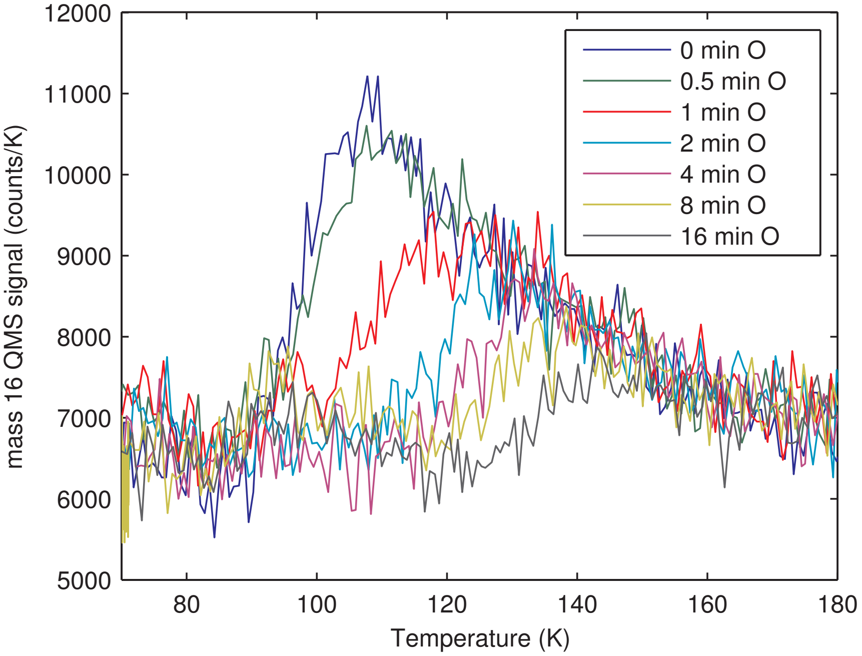

Figure 5.6: Mass 16 QMS signal in the TPD from a deposit of NH_3 (0.5 minute) + various doses of O at 70 K.

high. The degree of conversion of NH_3 can be gauged by looking at what remains of the NH_3 layers after various doses of oxygen. Figure 5.3 shows the TPD mass 17 signal (NH_3) for various doses of O. The NH_3 dose is fixed at 4 minutes, which is equivalent to about 2 ML. As the O exposure time increases, the NH_3 peak decreases, and the peak position also shifts to higher temperatures. This is likely because the top layer of NH_3 is gradually converted to NH_2OH or other products thus preventing NH_3 molecules underneath to desorb. After about 6 minutes of O exposure, the first peak almost disappears, indicating the top layer of NH_3 is almost all converted to NH_2OH or other products. Thus it takes at most 6 minutes of O (1.74 ML) to convert 1 ML of NH_3. Here we assumed that each oxygen atom that lands on the surface participates in a reaction, i.e., the sticking of O is unity. If this is not the case, then it would take even less atomic oxygen to convert NH_3. However, we only assumed ER reaction mechanism; if we also include LH mechanism, there is an additional uncertainty due to the unknown O diffusion energy barrier. If the reaction energy barrier is smaller than the diffusion energy barrier, one will not be able to tell the reaction energy

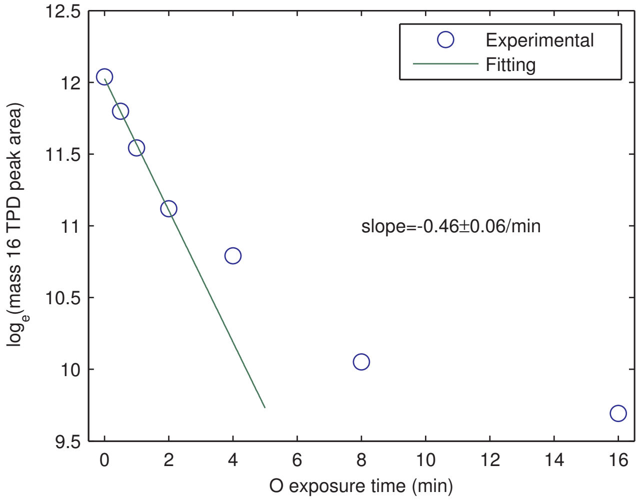

Figure 5.7: Integrated TPD signs mass 16 amu from a deposit of NH_3 (0.5 minutes or 1/4 of a ML) + various exposures of O at 70 K.

barrier. Therefore, a loose upper boundary of the reaction barrier could be the same as the O diffusion energy barrier. The O diffusion energy barrier has not been measured in the laboratory. More efforts are needed to study it.

5.3.4 Control experiments

Control experiments were carried out to verify whether ammonia react with molecular oxygen or ozone. We exposed the ammonia layers to O_2 and found no mass 33 or 30 amu peaks in the TPD, signifying that there has been no conversion of ammonia to hydroxylamine in the presence of molecular oxygen. We also checked the reactivity of ozone with ammonia. Ozone was prepared on a clean silicate following the procedure described in Chapter 3; then, 2 ML of ammonia were deposited on it. Again, there was no mass 33 or 30 amu peaks in the following TPD. See Figure 5.8 for the comparison.

5.4 Discussions

The grain surface formation route $NH_3 + O \rightarrow NH_2OH$ does not have a significant reaction energy barrier, thus it could be the dominant mechanism for hydroxylamine formation. The

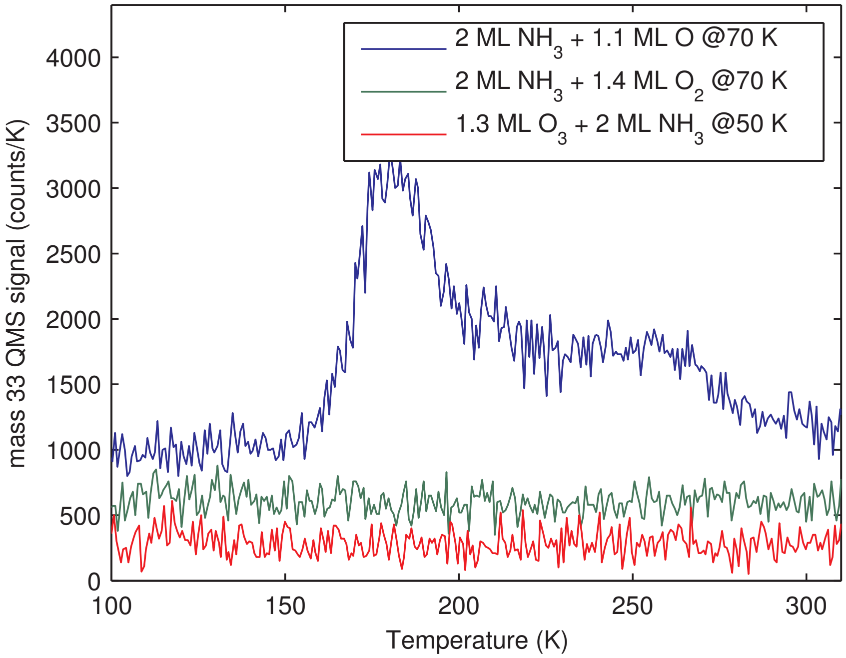

Figure 5.8: Mass 33 QMS signal in the TPD from NH_3 + O_2 and O_3 + NH_3 deposited at 70 K compared with that of NH_3 + O at 50 K. Curves are offset for clarity.

formation of hydroxylamine via ammonia oxidation is a single step reaction while in the NO hydrogenation route it takes three successive hydrogenation steps to form hydroxylamine. In the tenuous ISM condition, NH_3 oxidation should be more relevant. In addition, when the grain surface temperature is higher than about 20 K, the residence time of atomic hydrogen on the grain surface becomes short while atomic oxygen still has a very long residence time. Thus, the ammonia oxidation reaction covers a wider grain surface temperature range. Some unanswered questions still need further work. For instance, the secondary oxidation reactions are still unknown. Very long exposure times and preferably co-exposure of O and NH_3 from two beam lines, as well as infrared spectroscopy are necessary to study to secondary reactions. In addition, in the above, the sticking of O at 70 K is assumed to be unity. However, there is no experimental support for this assumption. A better understanding of O sticking as well as diffusion on ISM dust grain surfaces is important for any oxygen related grain surface reactions.

Gas-grain modeling taking into account the NH_3 oxidation reaction is under way in collaboration with Rob Garrod of Cornell University. The model is updated from the Ohio State University gas-grain model [2]. In this model, the temperature of dust grains and gas is fixed at 10 K, and the gas density is taken to be about 2×10^4 cm^{-3}, which represent a typical dense molecular cloud condition. Time dependent abundances of hundreds of species, both in gas phase and on grain surfaces, are obtained by solving coupled differential equations. Better picture of the hydroxylamine formation process should become available once the ammonia oxidation reaction described in this chapter is taken into account in simulation of chemical processes in dense clouds..

5.5 Conclusions

Hydroxylamine is an astrobiologically important molecule. The formation of it in the ISM is related to the exogenous origin of prebiotic molecules. The formation of it is proposed to be on dust grain surfaces. In this chapter, we studied the formation of hydroxylamine via the oxidation of ammonia at both multilayer and submonolayer coverages. The formation of hydroxylamine is found to be efficient at ISM relevant conditions. Compared to the recently studied NO hydrogenation route, the ammonia oxidation route could be more efficient, especially when the grain surface is at a higher temperature.

---

[2] http://www.physics.ohio-state.edu/~eric/research.html

Chapter 6

Diffusion-Desorption Rate Equation Model

Desorption and diffusion are two of the most important processes on interstellar grain surfaces; knowledge of them is critical for the understanding of chemical reaction networks in the interstellar medium (ISM). However, lack of information on desorption and diffusion is preventing further progress in astrochemistry. To obtain the desorption energy distribution of molecules from surfaces of ISM-related materials, one usually carries out adsorption-desorption temperature programmed desorption (TPD) experiments and uses rate equation models to extract desorption energy distributions. However, the often-used rate equation models fail to adequately take into account diffusion processes and thus are only valid in situations where adsorption is strongly localized. As adsorption-desorption experiments show, adsorbate molecules tend to occupy deep adsorption sites before occupying shallow ones; a diffusion process must be involved. Thus, it is necessary to include a diffusion term in the model that takes into account the morphology of the surface as obtained from analyses

---

This chapter is adapted from the following published paper with modifications:
Jiao He and Gianfranco Vidali. "Application of a diffusion–desorption rate equation model in astrochemistry." Faraday Discussions (2014).

of TPD experiments.

When molecules are deposited onto a non-uniform surface, those in the shallow adsorption sites have a higher possibility to jump out and move on the surface until they get trapped in another deep site. At the end, molecules should be found predominantly in deep sites instead of shallow sites. To model this re-distribution process, diffusion energy barrier distribution has to be included in the model. We use a rate equation model that includes a diffusion term to account for both the diffusion and desorption processes on the surface. Experimental data of CO desorption from the MgO(100) surface and of D_2 desorption from amorphous solid water ice are used as examples to show how a diffusion-desorption rate equation model explains the redistribution of adsorbate molecules among different adsorption sites. We extract from TPD profiles distributions of desorption energies and diffusion energy barriers for CO from MgO(100). These examples are contrasted with a system where adsorption is strongly localizes—HD from an amorphous silicate surface. Suggestions for experimental investigations are provided.

6.1 Introduction

The kinetics of interstellar related species on dust grain surfaces are known to play an important role in astrochemistry. Astrochemical modeling shows that the abundances of molecules such as H_2, H_2O and CO_2 can't be explained by gas phase reactions alone, and surface reactions must be involved (Williams, 2005; Garrod et al., 2008; Vidali, 2013). Desorption and diffusion are the two most important processes on surfaces, and they determine the rates of surface reactions. In recent years, there has been a considerable body of work on the surface kinetics of interstellar medium (ISM) - related species. Katz et al. (1999) used rate equations to extract desorption and diffusion energy barriers for atomic hydrogen from the data on formation of molecular hydrogen of Pirronello et al. (1997a,b) on polycrystalline olivine and amorphous carbon surfaces. Cazaux & Tielens (2004) came up with a similar model that included the possibility of diffusion via tunneling and the possibility of an atom dropping in a chemisorption site. Iqbal et al. (2012) studied the formation of molecular hydrogen over a wider range of surface temperatures using a kinetic Monte Carlo simulation to simulate the formation of molecular hydrogen in regions, such as PDRs (photodissociation regions), where grains are at a temperature higher than in diffuse and dense clouds. Amiaud et al. (2006, 2007) conducted D_2 adsorption-desorption experiments on both porous and non-porous amorphous water ices, then used a rate equation model and a direct inversion method to obtain desorption energy barriers. Noble et al. (2012) did experiments on the desorption of CO, O_2 and CO_2 from non-porous water ice, crystalline water ice and silicate surfaces, and used a Polanyi-Wigner equation to find the parameters governing desorption behaviors. He et al. (2011) used multiple desorption energy levels to simulate the adsorption-desorption experiments of D_2 on both single crystalline and amorphous silicate surfaces, and obtained semi-continuous desorption energy distributions. Desorption energies for a variety of ices, including ice mixtures, are summarized by Burke & Brown (2010). All of these investigations assumed either non-hopping between different desorption sites or adlayer equilibration (Sundaresan & Kaza, 1985). Thus, only the desorption energy can be obtained.

The diffusion of radicals is an obvious important step in the formation of molecules in or on ices. Because of its abundance and low mass, diffusion of H atoms is the most important process. H diffusion in CO ice leads to the formation of H_2CO and CH_3OH (Watanabe & Kouchi, 2002; Hidaka et al., 2004; Watanabe & Kouchi, 2008; Fuchs et al., 2009). H diffusion in N_2 leads to ammonia formation (Hidaka et al., 2011) and H diffusion in O_2 ices leads to the formation of water (Ioppolo et al., 2008; Miyauchi et al., 2008). In general, the formation of molecules on surfaces requires diffusion to take place, such as in the case of water formation via the deposition of H, O and O_2 on water ice (Oba et al., 2009; Dulieu et al., 2010) and on bare amorphous silicates (Jing et al., 2011, 2012). Similarly, the formation of molecules due to energetic particles or radiation involves the migration of super thermal radicals (Kaiser et al., 1999). Except in the investigation of D_2 formation by the bombardment of CD_4 ice with 5 keV electrons where rate equations were used to obtain the diffusion energy barrier for deuterium atoms (He et al., 2010), the analyses of these and other reactions do not contain estimates of diffusion energy barriers or diffusion coefficients.

The diffusion of larger molecules can also take place in or on ices and on bare surfaces. Mispelaer et al. (2013) studied the diffusion of CO, HNCO, H_2CO and NH_3 in amorphous ice using infrared spectroscopy, while He et al. (2014) investigated the formation of ozone via the diffusion of molecular and atomic oxygen on a bare amorphous silicate surface. Zubkov et al. (2007) studied the diffusion of nitrogen in amorphous solid water, and Roser et al. studied the formation of CO_2 via the migration of O in a water-ice capped CO ice (Roser et al., 2001). Because diffusion is more difficult to study than desorption, both experimentally and theoretically, much less information about diffusion on surfaces of interstellar dust analogs is available than that of desorption. It is often assumed that the energy barrier for thermal diffusion E_{diff} is a fraction of the desorption energy E_{des}, $E_{\text{diff}} = \alpha E_{\text{des}}$, where α is taken to be a constant value typically between around 0.3 for weakly adsorbed systems on well ordered surfaces (Antczak & Ehrlich, 2005) , and 0.7-0.8 on disordered or amorphous surfaces (Katz et al., 1999; Perets et al., 2005, 2007). Simulations of ISM chemistry that include surface reactions have used such a wide range of values as well (Stantcheva et al., 2002; Le Bourlot et al., 2012; Iqbal et al., 2012).

In any case, this relation $E_{\text{diff}} = \alpha E_{\text{des}}$ is an over-simplification. Since the diffusion energy barrier is in the exponential term of Polanyi-Wigner equation, a slight change in α could affect the diffusion rate by orders of magnitude, resulting in unrealistic reaction rates. Surface diffusion occurs both by quantum tunneling and by thermally activated hopping. Quantum tunneling is efficient for very light adsorbed species such as atomic (Watanabe & Kouchi, 2008) and molecular hydrogen (Oba et al., 2012) , but the efficiency decreases dramatically as the mass of ad-species increases. Furthermore, quantum tunneling depends on both the energy barrier and the separation to the site that the particle is tunneling into. It typically decreases dramatically for disordered or amorphous surfaces. Hama et al. (2012) studied the diffusion of hydrogen atoms on the surface of amorphous water ice, using a combination of photon-stimulated desorption and REMPI (Resonance Enhanced MultiPhoton Ionization) and found that hydrogen becomes trapped at deep sites, confirming the indirect evidence obtained in the study of H_2 formation on silicates and amorphous carbon (Pirronello et al., 1997b, 1999; Katz et al., 1999) and on amorphous silicates (Perets et al., 2007). For ad-species other than hydrogen, thermal diffusion is the dominant diffusion mechanism and will be the focus of this chapter.

The remaining of this chapter is organized as follows. In the next section the rate equation model as in its widely used form is introduced. In Section 6.3 the diffusion-desorption rate equation model is presented, and in Section 6.4 it is applied to the systems CO on MgO(100) (Dohnálek et al., 2001), D_2 on non-porous water ice (Amiaud et al., 2007), and HD on amorphous silicate surface, followed by a discussion of the limitations and suggestions for experimental investigations. Section 6.5 summarizes this chapter.

6.2 Rate equation model

The rate equations introduced in Section 1.7 assumes all surface sites are identical. In reality, however, a surface consists of different adsorption sites, and to better describe the desorption behavior a continuous desorption energy distribution $f(E_{\mathrm{des}})$ is required. We modify the rate equation as:

$$\int f(E_{\mathrm{des}})\ \mathrm{d}E_{\mathrm{des}} = 1 \tag{6.1}$$

$$\frac{\mathrm{d}\theta(E_{\mathrm{des}},t)}{dt} = flux(t)(1-\theta(E_{\mathrm{des}},t)) - \nu\theta(E_{\mathrm{des}},t)\exp\left(-\frac{E_{\mathrm{des}}}{k_{\mathrm{B}}T(t)}\right) \tag{6.2}$$

$$R(t) = \int\left(flux(t)\theta(E_{\mathrm{des}},t) + \nu\theta(E_{\mathrm{des}},t)\exp\left(-\frac{E_{\mathrm{des}}}{k_{\mathrm{B}}T(t)}\right)\right) f(E_{\mathrm{des}})\ \mathrm{d}E_{\mathrm{des}} \tag{6.3}$$

Equation (6.1) gives the desorption energy distribution, equation (6.2) gives the coverage as a function of time for different sites, the $(1 - \theta(E_{\mathrm{des}}, t))$ is the rejection term to avoid multiple occupancy of the same site. For molecules that can build up ices on the surface, the rejection term is not necessary. To describe multi-monolayer coverage systems, a different form of the rate equation is needed, but is not the focus of this work. For molecules that have a very low desorption energy from themselves, such as hydrogen desorption from hydrogen, if the surface temperature is not low enough, the saturation coverage is about or less than one monolayer, and a rejection term is convenient for dealing with such systems. In equation (6.3), $R(t)$ is the total number of particles that come off the surface, which equals the desorption rate plus reflection/rejection of the incoming flux. $R(t)$ should be proportional to the signal measured by the mass spectrometer. The integration in equation (6.1) and equation (6.3) is over the whole desorption energy spectrum.

This set of equations forms the basis for interpretation of most adsorption-desorption experiments. The more energy levels used in the modeling, the smoother the energy distribution becomes. In He et al. (2011) more than 50 energy levels were used to fit the TPD spectra; a semi-continuous desorption energy distribution was obtained for both amorphous and single crystalline silicates. To obtain a continuous desorption energy distribution, some groups used a direct inversion method based on first order desorption to extract information from TPD spectra (Vidali & Li, 2010); a more detailed analysis can be found in Barrie (2008). These analyses are based on first order desorption without diffusion. We show below that diffusion is necessary to explain the experimental data.

In some systems, however, it is found that the desorption energy is coverage dependent; as coverage increases from 0 to 1 ML, the TPD peak shifts to lower temperatures, as shown in Dohnálek et al. (2001) and Amiaud et al. (2007) (referred to as Dohnálek2001 and Amiaud2007 hereafter). There are two different explanations for the temperature shift. One is adsorbate lateral interactions, the other is hopping between different adsorption sites. For the former, lattice-gas modeling has been used to simulate the effect of lateral interactions on TPD shapes (Sundaresan & Kaza, 1985; Tovbin, 1990; Meng & Weinberg, 1997), and fitting with TPD traces can be obtained. However, in the ISM the coverage of ad-species on grain surfaces is typically very small (much smaller than 1 ML). In low coverage experiments that find applications in astrochemistry, the morphology and hopping between different adsorption sites of the surface contribute more to the desorption than lateral interactions. Therefore, in this chapter we focus on the effects of hopping and ignore lateral interactions. In the exposure stage, particles tend to occupy deeper adsorption sites before they occupy the shallower sites. The intrinsic physical process underlying this phenomenon is surface diffusion. When adsorbate particles are in the shallow sites, the diffusion energy barrier is also low. Particles escape from the shallow adsorption sites and move on the surface until they reach deeper sites where the diffusion energy barrier is high enough that they are trapped.

In analysis of TPD experimental data of CO desorption from MgO, Dohnálek2001 used an inversion method to extract the continuous coverage dependent desorption energy distribution, and the extracted spectrum can reproduce experimental traces very well. It should be noted that the direct inversion method is only applicable to the equilibrium diffusion state, in which the mobility of particles on a surface is so fast that particles are already in an equilibrium state before desorption begins. By using the direct inversion method Dohnálek2001 and Amiaud2007 implicitly assume high mobility of adsorbate particles. The effect of limited mobility of ad-species was discussed by Šurda & Karasova (1981), but, to best of our knowledge, this work has not been used in astrochemistry. The next section introduces the diffusion-desorption rate equation that was inspired by the work of Šurda & Karasova (1981).

6.3 The diffusion-desorption rate equation model

An adsorption-desorption experiment involves both desorption and diffusion processes. Hereby, the desorption rate and diffusion rate both depend on the substrate surface temperature. Below, we assume that both obey an Arrhenius-like expression. The desorption rate for sites with desorption energy $E_{\rm des}$ can be expressed as $\nu\theta(E_{\rm des}, t)\exp\left(-\frac{E_{\rm des}}{k_{\rm B}T(t)}\right)$; similarly the diffusion rate is $\nu_{\rm diff}\theta(E_{\rm des}, t)\exp\left(-\frac{E_{\rm diff}}{k_{\rm B}T(t)}\right)$, where $E_{\rm diff}$ is the diffusion energy barrier for those sites with desorption energy $E_{\rm des}$. There is a positive relation between $E_{\rm des}$ and $E_{\rm diff}$, i.e., sites with higher desorption energy also have higher diffusion energy barriers. A distinction is made between the two pre-factors $\nu_{\rm diff}$ and ν, since they correspond to different physical processes and could have different values. Diffusion consists of two subprocesses: 1) particles hop out of adsorption sites and go to a transition state; 2) particles in the transition state go back to the adsorption sites. There is a redistribution in the second subprocess depending on the availability of adsorption sites. If a particle can go on top of another in the same adsorption site, particles in transition states will be redistributed evenly among all adsorption sites. Otherwise, if a particle cannot go on top of another, the particle in the transition state will be redistributed evenly among all *empty* sites; hereafter we assume the latter case.

The desorption energy is a continuous distribution. Let us assume it can be represented by a single Gaussian distribution. As is shown in Figure 6.1, the diffusion energy barrier $E_{\rm diff}$ is the difference between the desorption energy $E_{\rm des}$ and the energy at the transition state $E_{\rm tr}$, $E_{\rm diff} = E_{\rm des} - E_{\rm tr}$. Suppose that $E_{\rm tr}$ follows also a Gaussian distribution, then we express these two distributions as

$$f(E_{\rm des}) = \frac{1}{\sigma_{\rm des}\sqrt{2\pi}}\exp\left(-\frac{(E_{\rm des} - \overline{E_{\rm des}})^2}{2\sigma_{\rm des}^2}\right) \tag{6.4}$$

$$f(E_{\rm tr}) = \frac{1}{\sigma_{\rm tr}\sqrt{2\pi}}\exp\left(-\frac{(E_{\rm tr} - \overline{E_{\rm tr}})^2}{2\sigma_{\rm tr}^2}\right) \tag{6.5}$$

Assuming that these two distributions are independent, then $E_{\rm diff}$ is also a Gaussian distribution, with $\overline{E_{\rm diff}} = \overline{E_{\rm des}} - \overline{E_{\rm tr}}$ and $\sigma_{\rm diff} = \sqrt{\sigma_{\rm des}^2 + \sigma_{\rm tr}^2}$. If we further assume that $\overline{E_{\rm diff}}$ is not far from $\overline{E_{\rm des}}$—it has been suggested $E_{\rm diff} \sim 0.5\text{-}0.7\ E_{\rm des}$ (Katz et al., 1999; Perets et al., 2007; Yıldız et al., 2013), then $\sigma_{\rm tr}^2$ should be much smaller than $\sigma_{\rm des}^2$; we assume $\sigma_{\rm diff} = \sqrt{\sigma_{\rm des}^2 + \sigma_{\rm tr}^2} \approx \sigma_{\rm des}$, which means that $E_{\rm diff}$ can be approximated by $E_{\rm diff} =$

$E_{\mathrm{des}} - \overline{E_{\mathrm{tr}}} = E_{\mathrm{des}} - \Delta E$. A more general expression would be $E_{\mathrm{diff}} = \alpha(E_{\mathrm{des}} - \Delta E)$.

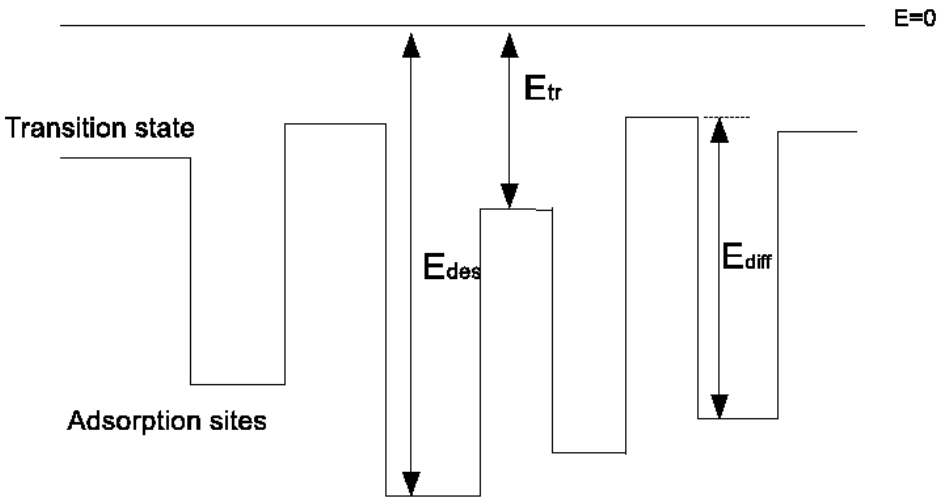

Figure 6.1: Diagram of surface adsorption sites and transition states.

Now equation (6.2) should be modified as follows:

$$\begin{aligned}\frac{\mathrm{d}\theta(E_{\mathrm{des}},t)}{dt} = \quad & \underbrace{flux(t)(1-\theta(E_{\mathrm{des}},t))}_{\text{term 1}} - \underbrace{\nu\theta(E_{\mathrm{des}},t)\exp\left(-\frac{E_{\mathrm{des}}}{k_{\mathrm{B}}T(t)}\right)}_{\text{term 2}} - \\ & \underbrace{\nu_{\mathrm{diff}}\theta(E_{\mathrm{des}},t)\exp\left(-\frac{\alpha(E_{\mathrm{des}}-\Delta E)}{k_{\mathrm{B}}T(t)}\right)}_{\text{term 3}} + \\ & \underbrace{\frac{1-\theta(E_{\mathrm{des}},t)}{1-\Theta(t)}\int \nu_{\mathrm{diff}}\theta(E'_{\mathrm{des}},t)\exp\left(-\frac{\alpha(E'_{\mathrm{des}}-\Delta E)}{k_{\mathrm{B}}T(t)}\right) f(E'_{\mathrm{des}})\,\mathrm{d}E'_{\mathrm{des}}}_{\text{term 4}}\end{aligned} \tag{6.6}$$

$$\Theta(t) = \int \theta(E_{\mathrm{des}},t) f(E_{\mathrm{des}})\,\mathrm{d}E_{\mathrm{des}} \tag{6.7}$$

equation (6.1) and equation (6.3) are unchanged. In equation (6.6), term 1 is the flux term (assuming particles cannot go on top of each other), term 2 is the desorption term, term 3 is the diffusion term that describes particles going to transition states, term 4 is the redistribution term from the transition states (assuming particles can only go to empty sites), and the factor $(1-\theta(E_{\rm des},t))/(1-\Theta(t))$ accounts for the redistribution of particles in transition states among empty adsorption sites. In equation (6.7), $\Theta(t)$ is the overall coverage. Note that integration of terms 3 and 4 over the whole energy spectrum gives zero; this means that in diffusion processes the total particle number is conserved, which should hold true for the model to be correct since diffusion alone won't change the total number of particles on the surface. The diffusion term is no longer a first order term. In fact it behaves like a second order term. Thus the modified rate equation model is a candidate to interpret coverage dependent desorptions. A comparison with the complete model in Li et al. (2010) (referred to as Li2010 hereafter) is worth mentioning here. It can be shown that in the low coverage limit, this model is equivalent to equation (5) in Li2010; however, at coverage approaching 1 ML they differ. In Li2010 it is assumed that at a coverage close to 1 ML the diffusion rate is close to 0; however in this chapter we assume the probability that particles jump out from adsorption sites to transition sites is independent of coverage, which leads to the exchange of particles among adsorption sites and a faster redistribution. The calculated diffusion rate is thus faster in this work than in Li2010.

6.4 Simulations and discussion

6.4.1 CO on MgO(100)

Below we illustrate how to utilize the rate equation model to extract the adsorption-diffusion energy parameters. The experimental data are taken from Dohnálek2001, where a detailed description of the experiment can be found. A highly ordered MgO(100) surface kept at 22 K was exposed to different doses of CO gas in ultra-high vacuum. The MgO(100) film was grown epitaxially on an Mo(100) substrate at 600 K by evaporation of Mg metal in an O_2 atmosphere. The dose of CO was calculated by integration of TPD traces to be θ=(0.09, 0.16, 0.23, 0.32, 0.42, 0.48, 0.58, 0.71, 0.90, 1.00, 1.14, 1.27) ML. Below we only discuss the submonolayer range, omitting the last two coverages. After exposure, the thin film surface was subjected to a linear heating ramp of $\beta = \mathrm{d}T/\mathrm{d}t = 0.6$ K/sec to desorb the CO molecules. The TPD traces are shown in Figure 6.2. We begin with the direct inversion of equation (1.13); the coverage dependent desorption energy can be calculated for each TPD trace as follows:

$$E(\theta) = -k_{\mathrm{B}}T\ln\left(-\frac{\beta}{\nu\theta}\frac{\mathrm{d}\theta}{\mathrm{d}T}\right) \tag{6.8}$$

The resulting desorption energy distribution $f(E_{\mathrm{des}})$ obtained from inverting the 1 ML curve is shown in Figure 6.3.

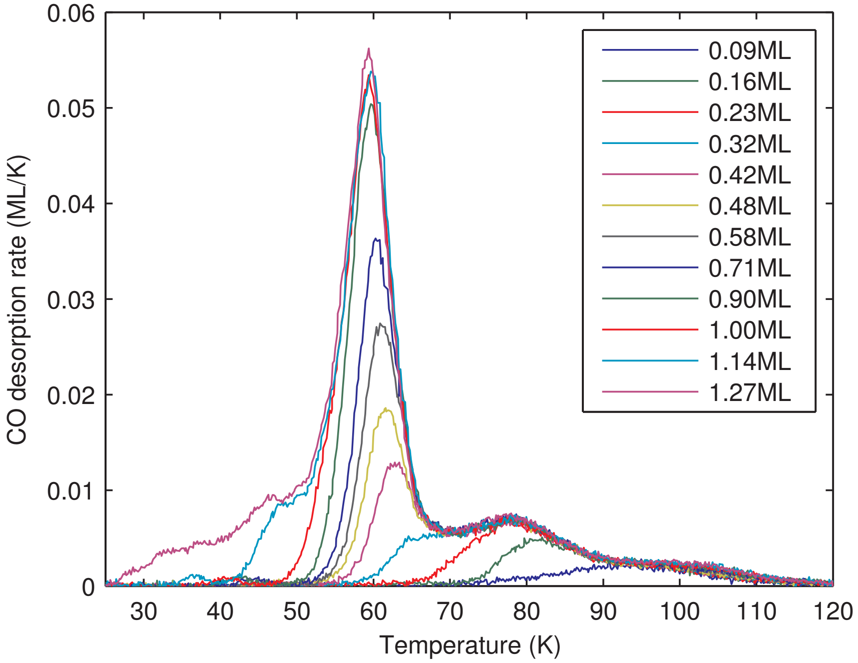

Figure 6.2: CO TPD spectra for monolayer and submonolayer coverages of CO/MgO(100) (θ = 0.09, 0.16, 0.23, 0.32, 0.42, 0.48, 0.58, 0.71, 0.90, 1.00, 1.14, 1.27). Replotted from Dohnálek et al. (2001).

In Dohnálek2001, TPD traces for different initial coverages are inverted and different pre-exponential factors are tried until convergence is achieved among the inverted distributions from different initial coverages. They found $\nu = 10^{15}$ sec^{-1}. In our opinion this value should be revised. Nordholm (1985) found that abnormally large pre-exponential factors might come from dispersion in the desorption energy. Thus, to determine the pre-exponential factor using convergence might be incorrect. ν is a fundamental factor that depends on both the substrate and the adsorbate, and its value is better to be determined by ab-initio calculations. We are not aware of such calculations for the present system. Therefore, we prefer to use the widely accepted value $\nu = 10^{12}$ sec^{-1}. For ν_{diff} there is even less information available, and we use the same value as ν for simplicity.

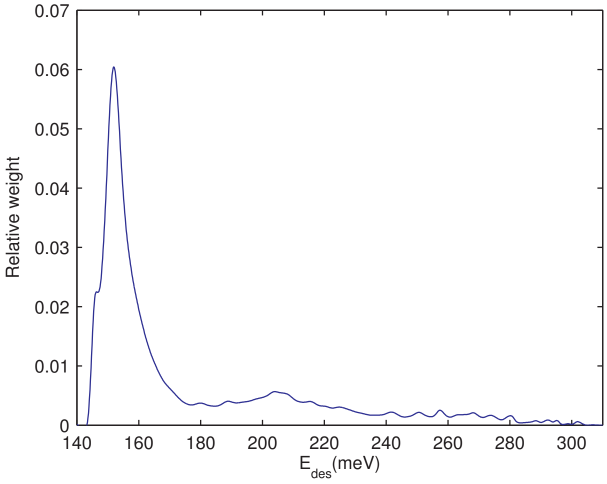

Figure 6.3: Desorption energy barrier distribution for CO on MgO(100) obtained using data of Dohnálek et al. (2001)

In equation (6.6) if one lets the diffusion terms equal to zero, then the diffusion-desorption rate equation is a rate equation for non-hopping ad-species. This should become a first order desorption. The simulated TPD traces are shown in Figure 6.4, which is a typical first order TPD spectra, as expected. Next, we set the desorption term and the flux term equal to 0, i.e., we assume no incoming flux and no desorption, and focus on the diffusion process. We start from an initial coverage of 0.3 ML for all desorption sites with $\Delta E = 30$ meV, $\nu_{\text{diff}} = 10^{12}$ sec^{-1}, and then monitor the redistribution process during warm-up. Figure 6.5 shows the fractional occupation distribution at temperature 22 K, 40 K, 45 K, 50 K, 55 K, 60 K, 65 K, 70 K and 75 K. As is shown in the figure, at 22 K and 40 K, the surface has a uniform coverage of 0.3 ML. When the surface temperature rises to 45 K, molecules in shallow sites ($E_{\text{des}} < 150$ meV) become active and begin to diffuse, distributing themselves evenly among deeper sites that have not been occupied yet. As temperature rises further, deeper sites come into play and molecules in them begin to diffuse. After the temperature

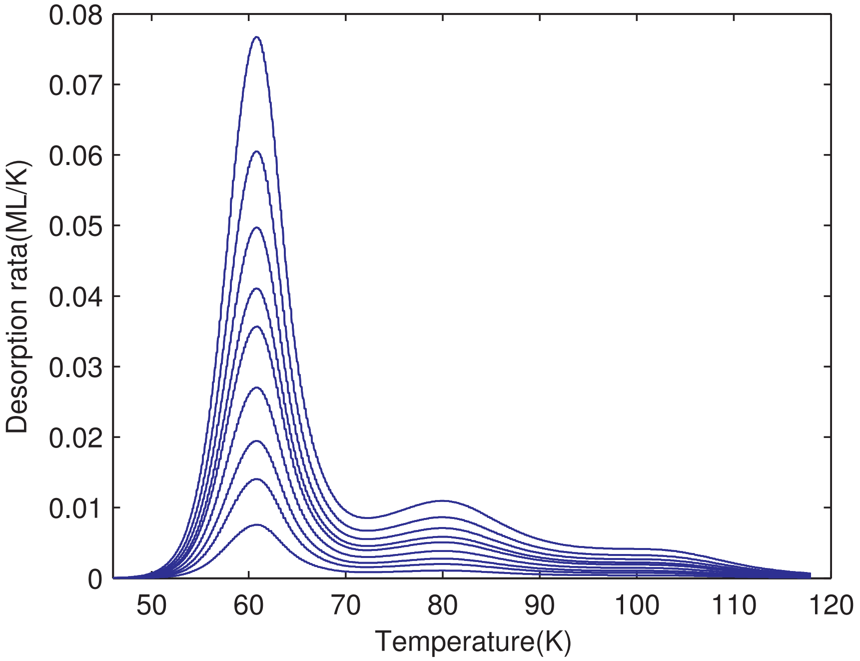

Figure 6.4: Simulation of TPD spectra for different initial coverages using the desorption energy distribution obtained from direct inversion of CO on MgO(100) TPD spectra of Dohnálek et al. (2001), see Figure 6.3.

reaches a point where the deepest sites are fully occupied (about 65 K in this case), the distribution does not change any more as we increase the temperature further. This means that when the diffusion rate is high enough, the coverage distribution does not change as the diffusion rate is further increased. In the fast diffusion case, one cannot get the absolute value of the diffusion energy barrier, only a lower bound is obtainable, or, equivalently, a lower bound for ΔE. What one sees in a TPD is that molecules occupy deeper sites before they go to shallower sites, and the TPD trailing edges for different initial coverages should converge. This justifies the use of the direct inversion method, since the direct inversion method assumes that molecules automatically occupy the deepest sites available on the surface. On the other hand, if the diffusion rate is limited, ad-species start to desorb and leave the surface before an diffusion equilibrium state is achieved (Šurda & Karasova, 1981). If one plots the weighted overall desorption rate and diffusion rate as a function of temperature, the two traces might overlap each other. If the overlapping is small, i.e., the desorption starts after most molecules have begun to diffuse, the assumption of fast

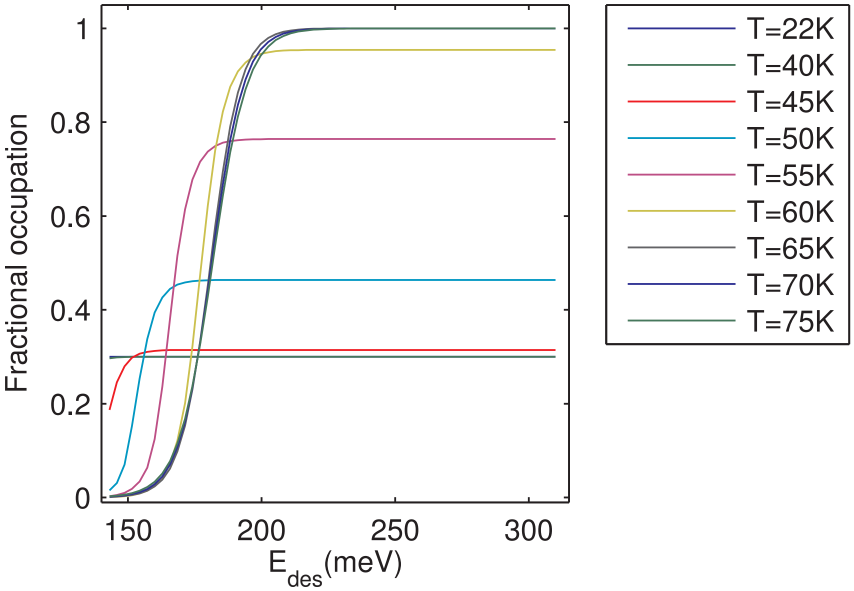

Figure 6.5: Fractional occupation of adsorption sites at different temperatures: 22 K, 40 K, 45 K, 50 K, 55 K, 60 K, 65 K, 70 K and 75 K. No desorption is assumed and only the diffusion process is simulated. The initial coverage and ΔE are 0.3 ML and 30 meV, respectively. As the temperature increases, molecules move from shallow adsorption sites to deeper ones.

diffusion holds true. However, if the two traces overlap significantly, an diffusion equilibrium state cannot be obtained before desorption begins, and the direct inversion method is less applicable. In this latter case, the diffusion-desorption rate equation model should be used instead.

Now we show how to obtain the E_{diff} distribution or, equivalently, the value (or range) of ΔE. We try different values of ΔE in equation (6.6) and simulate TPD for different initial values of the coverage until we find the value that best fits the experimental data. The results are shown in Figure 6.6. It can be seen from the simulation results that when ΔE is small the TPD traces are similar to first order desorption with high localization. As ΔE increases, the gaps between trailing edges decrease. When ΔE is greater than 30 meV, there are almost no gaps, and the shape of TPD traces does not change as the ΔE value is increased further. Thus we only get a lower boundary for ΔE in the case of fast diffusion. This is consistent with our previous argument about equilibrium diffusion state.

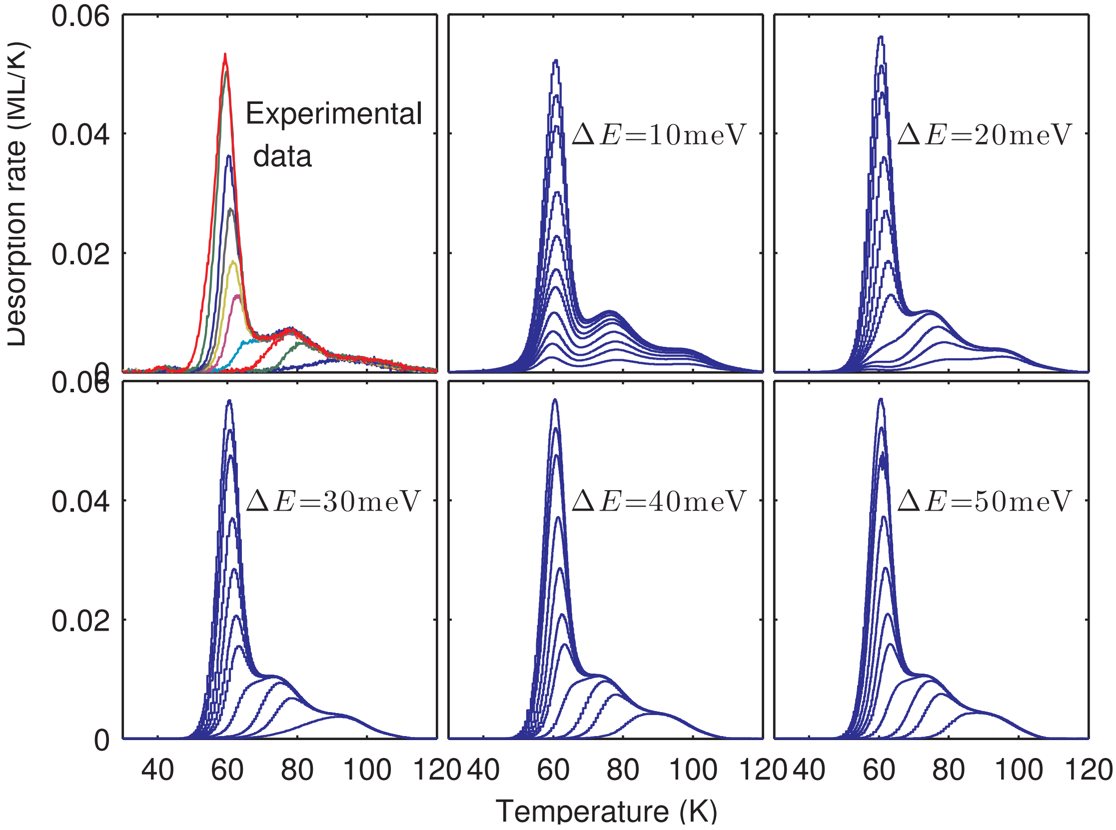

Figure 6.6: Simulation of Dohnálek et al. (2001) experimental data using different ΔE values, based on the diffusion-desorption rate equation model. The experimental data are shown in the first panel.

6.4.2 H_2/D_2 adsorption-desorption

H_2/D_2 plays an important role in interstellar chemistry. Much work has been done on the desorption of H_2/D_2 from dust grain surfaces (He et al., 2011; Amiaud et al., 2006, 2007). Typically, the desorption energies of H_2/D_2 from dust grain surfaces are so low that even at surface temperatures as low as 10 K the sticking coefficient is not unity. In addition, there might exist shallow adsorption sites which are always empty. Deep sites are the ones that contribute. One such example is reported in Amiaud et al. (2007). In this work, water ice films were grown on a copper surface using a microchannel array doser. The morphology was checked to be non-porous amorphous by N_2 adsorption/desorption TPD experiments (Kimmel et al., 2001). The sample was kept at 10 K and exposed to various doses of D_2.

After exposure, a TPD was carried out with a heating rate of 10 K/minute. The TPD spectra are shown in Figure 6.7. The saturation coverage is about 0.55 exposed monolayer (EML), which is equivalent to about 0.15 ML according to the calibration in Amiaud et al. (2007). This means that only the 15% deepest sites are occupied at 10 K. Following the same direct inversion procedure as discussed above, a desorption energy barrier distribution E_{des} can be obtained. However, the obtained distribution represents only deep adsorption sites since the shallow sites are not occupied. One cannot obtain the full distribution unless the exposure temperature is low enough so that desorption from the shallower sites is negligible during exposure.

The question arises whether useful information about diffusion can be extracted in instances when the data doesn't give the complete distribution of adsorption energy sites. This is the case when the surface temperature is not low enough and a full layer of an adsorbate cannot be built. To make some progress on this point, we rephrase the question as how an unknown distribution of the shallow sites affects the TPD traces. Since the shallow sites are always empty, the exact distribution might not matter and we can use a guessed shallow-site distribution. We now create two model distributions sharing the same distribution of deep sites but with a different shallow sites distribution, as shown in Figure 6.8. The exposure temperature in the model is chosen as 10 K and the maximum exposure time is such that the coverage is about half a monolayer. The effective exposure rate (flux times sticking coefficient) is 0.01 ML/s; exposure duration is 5 seconds to 50 seconds in 5 seconds increments. ΔE value is set to be 10 meV. A heating rate of 10 K/minute is applied 100 seconds after exposure; this gives enough time for molecules in the shallow sites to desorb or move into the deep sites. The simulated TPD spectra are shown in Figure 6.9 and Figure 6.10. It can be seen that the distribution of the shallow sites affects only the high coverage traces, but overall there is not a significant change in the TPD spectra. Had we chosen a lower saturation coverage, such as a quarter of a layer, there would have been hardly any differences in the TPD traces. Thus, one should be able to use a guessed desorption energy distribution for the unknown shallow sites without affecting significantly the TPD traces in the low coverage range.

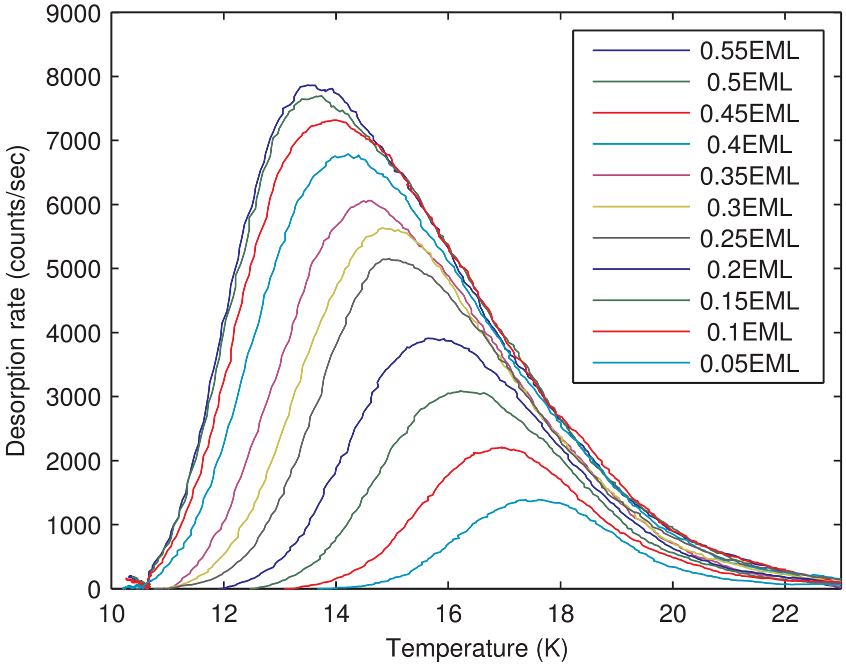

Figure 6.7: TPD spectra for D_2 adsorption-desorption from non-porous amorphous water ice; the surface temperature during exposure with D_2 is 10 K. Data from Amiaud et al. (2007)

6.4.3 HD on an amorphous silicate

Here we analyze the HD desorption from an amorphous silicate surface. The sample was prepared by Dr. Brucato (then at the Osservatorio Astronomico di Capodimonte Naples) by laser ablation of targets in an oxygen atmosphere. The experimental setup and measuring methods are similar to the ones described in Perets et al. (2007). To summarize: an amorphous silicate ($FeMgSiO_4$) sample was kept at 10.5 K and exposed to an HD beam flux for 30 seconds, 1 minute, 2 minutes, 4 minutes and 8 minutes. Coverages was estimated to be are well below 1 ML (Perets et al., 2007). After exposure, the surface was warmed up by cutting off the liquid helium flow. A reproducible heating curve is achieved for different TPD runs. The TPD traces are shown in Figure 6.11. Applying the direct inversion method to the

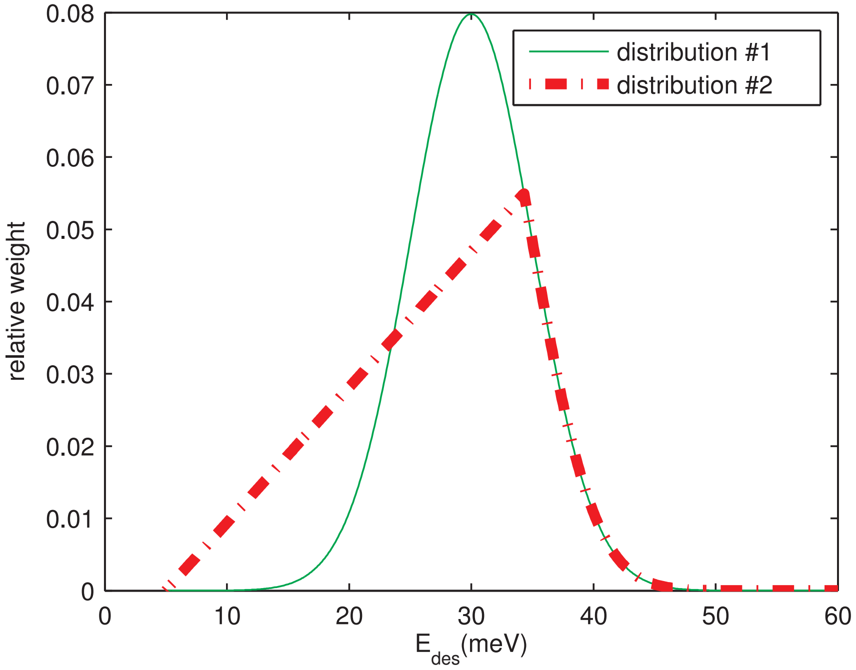

Figure 6.8: Two model desorption energy distribution sharing the same tail.

trace of 4 minutes exposure, which is typical, we obtain the desorption energy distribution shown in Figure 6.12. The TPD spectra are typical of first order desorption without hopping (Kolasinki, 2008); this indicates that the diffusion energy barriers are similar or even higher than the desorption energies so that diffusion does not take place before desorption.

6.4.4 Limitations and suggestions for experimental investigations

As we have seen in the first example, although we are able to obtain good fits for the adsorption-desorption TPD profiles, we can get only a lower limit to ΔE. Furthermore, we considered only thermally activated diffusion since there are more experimental data available. Based on our analyses, we suggest steps in future investigations that could facilitate the extraction of important parameters. In experimental investigations, efforts should be made to push the film in a far from equilibrium state to separate the trailing edges. This is done with flash desorption in many surface science studies (Kolasinki, 2008) but it poses technical challenges for surfaces kept at liquid helium temperature. It would be advantageous to study

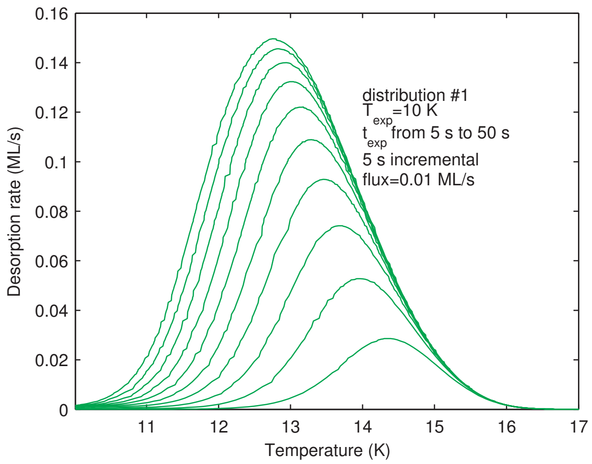

Figure 6.9: Simulated TPD spectra using the desorption energy distribution #1 in Figure 6.8

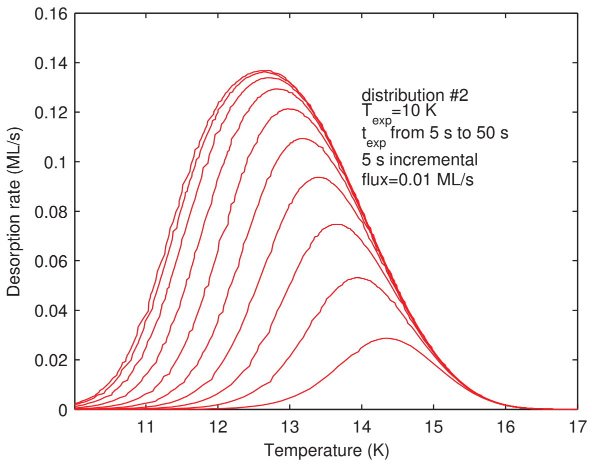

Figure 6.10: Simulated TPD spectra using the desorption energy distribution #2 in Figure 6.8

films at very low coverages, since the differences in TPD traces with different ΔE are most significant when coverages are low, as can be seen in Figure 6.6. Furthermore, special care needs to be paid to the pumping speed, background noise and desorption from parts other than the sample, since these affect the TPD traces, especially the tailing edges.

6.5 Conclusions

In this chapter we discussed the limitation of the often-used rate equation model when simulating adsorption-desorption TPD experimental profiles, and introduced a diffusion-desorption rate equation model to take into account the diffusion processes. Desorption and diffusion energy barrier distributions are obtained for CO on MgO(100). We then presented a system, HD desorption from an amorphous silicate, where there is hardly any evidence of diffusion. We also investigated what can be learned of the adsorption/desorption/diffusion processes, if data for only a partial layer is available. These distributions, or information obtained from them, can be used in models of the chemical evolution of ISM environments. For example, Herbst & Cuppen (2006) and Iqbal et al. (2012) have taken into consideration in their kinetic Monte Carlo models the morphology of the surface in the formation of molecular

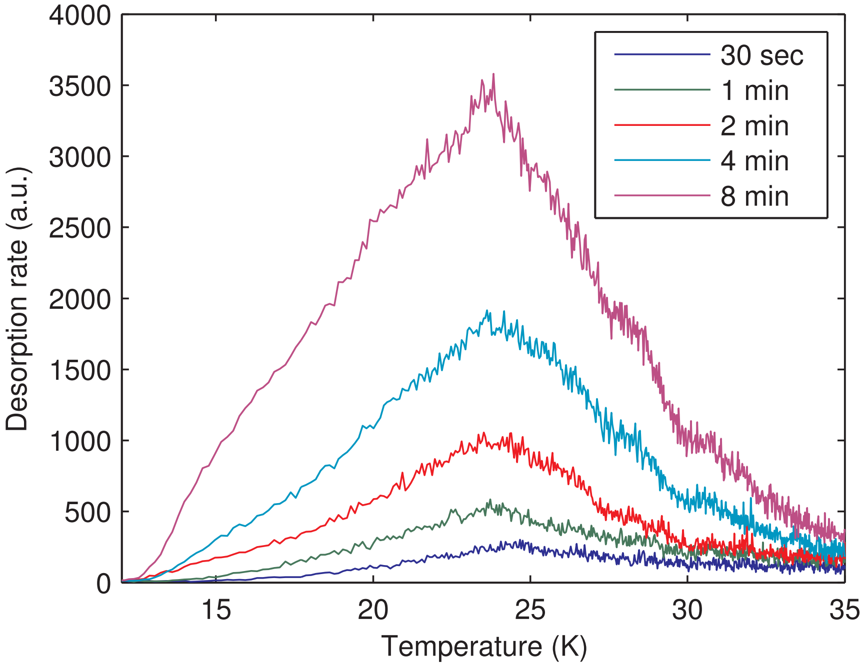

Figure 6.11: HD desorption from amorphous silicate ($FeMgSiO_4$) surface. The exposure doses are 30 sec, 1 minute, 2 minutes, 4 minutes and 8 minutes. The surface temperature during exposure with HD is 10.5 K.

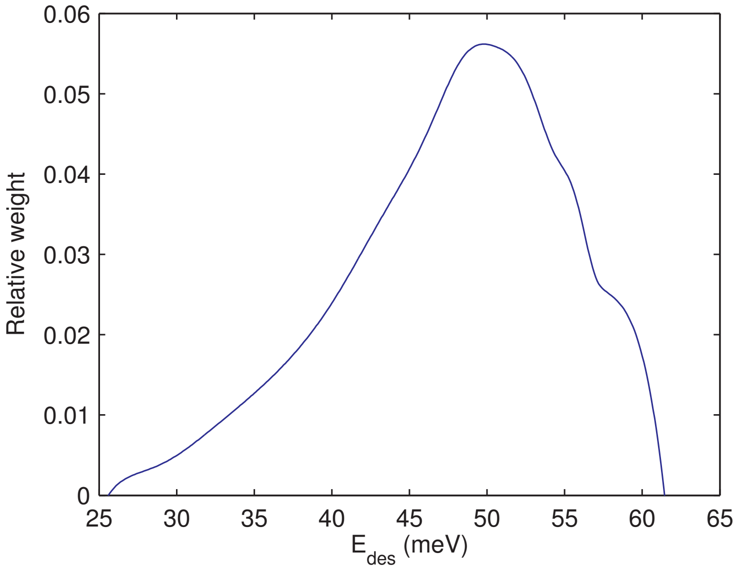

Figure 6.12: HD desorption energy distribution obtained from direct inversion of the TPD spectra in Figure 6.11.

hydrogen on surfaces. At that time, little or no information was available on diffusion energy barriers and on the distribution of the adsorption of energy sites besides little more than rules of thumb. Now we have shown that by using existing TPD data it is possible to tease out important information on the energetics of adsorption/desorption and diffusion. Furthermore, we have made suggestions for future experimental investigations so analyses of this data will yield more detailed information on these important processes that are at the heart of molecule formation on interstellar dust grains.

Bibliography

Akyilmaz, M., Flower, D. R., Hily-Blant, P., Pineau des Forêts, G., & Walmsley, C. M. 2007, A&A, 462, 221

Allamandola, L., & Norman, C. 1978, A&A, 63, L23

Allen, M., & Robinson, G. W. 1977, ApJ, 212, 396

Amiaud, L., Dulieu, F., Fillion, J.-H., Momeni, a., & Lemaire, J. L. 2007, J. Chem. Phys., 127, 144709

Amiaud, L., Fillion, J. H., Baouche, S., et al. 2006, J. Chem. Phys., 124, 94702

Antczak, G., & Ehrlich, G. 2005, Surf. Sci., 589, 52

Bacmann, A., Taquet, V., Faure, A., Kahane, C., & Ceccarelli, C. 2012, A&A, 541, L12

Baragiola, R., Atteberry, C., Bahr, D., & Jakas, M. 1999, Nucl. Instruments Methods Phys. Res. Sect. B Beam Interact. with Mater. Atoms, 157, 233

Barrie, P. J. 2008, Phys. Chem. Chem. Phys., 10, 1688

Baulch, D. L., Campbell, I. M., & Hainsworth, R. 1984, J. Chem. Soc. Faraday Trans. 1 Phys. Chem. Condens. Phases, 80, 2525

Bennett, C. J., & Kaiser, R. I. 2005, ApJ, 635, 1362

Bisschop, S. E., Fraser, H. J., Öberg, K. I., van Dishoeck, E. F., & Schlemmer, S. 2006, A&A, 449, 1297

Blagojevic, V., Petrie, S., & Bohme, D. K. 2003, MNRAS, 339, L7

Bolina, A. S., Wolff, A. J., & Brown, W. A. 2005, J. Chem. Phys., 122

Brack, A. 1999, Adv. Sp. Res., 24, 417

Burke, D. J., & Brown, W. a. 2010, Phys. Chem. Chem. Phys., 12, 5947

Caselli, P., Hasegawa, T. I., & Herbst, E. 1998, ApJ, 495, 309

Caselli, P., Walmsley, C. M., Zucconi, A., et al. 2002, ApJ, 565, 344

Cazaux, S., & Tielens, A. G. G. M. 2004, ApJ, 604, 222

Charnley, S. B., Rodgers, S. D., & Ehrenfreund, P. 2001, A&A, 378, 1024

Cohen, N. 1987, Int. J. Chem. Kinet., 19, 319

Collings, M. P., Anderson, M. A., Chen, R., et al. 2004, MNRAS, 354, 1133

Congiu, E., Fedoseev, G., Ioppolo, S., et al. 2012a, ApJ, 750, L12

—. 2012b, ApJL, 750, L12

Cooper, G., Kimmich, N., Belisle, W., et al. 2001, Nature, 414, 879

Cuppen, H. M., Ioppolo, S., Romanzin, C., & Linnartz, H. 2010, Phys. Chem. Chem. Phys., 12, 12077

Del Bene, J. E. 1972, J. Chem. Phys., 57

Djouadi, Z., Robert, F., Le Sergeant d'Hendecourt, L., et al. 2011, A&A, 531, A96

Dohnálek, Z., Kimmel, G. a., Joyce, S. a., et al. 2001, J. Phys. Chem. B, 105, 3747

Du, F., Parise, B., & Bergman, P. 2012, A&A, 538, A91

Dulieu, F., Amiaud, L., Congiu, E., et al. 2010, A&A, 512, A30

Dulieu, F., Congiu, E., Noble, J., et al. 2013, Sci. Rep., 3, 1338

Ennis, C. P., Bennett, C. J., & Kaiser, R. I. 2011, Phys. Chem. Chem. Phys., 13, 9469

Fedoseev, G., Ioppolo, S., Lamberts, T., et al. 2012, J. Chem. Phys., 137, 54714

Fenimore, C. P., & Jones, G. W. 1961, J. Phys. Chem., 65, 298

Fuchs, G. W., Cuppen, H. M., Ioppolo, S., et al. 2009, A&A, 505, 629

Fujii, N., Chiba, K., Uchida, S., & Miyama, H. 1986, Chem. Phys. Lett., 127, 141

Garrod, R. T. 2013, ApJ, 765, 60

Garrod, R. T., & Pauly, T. 2011, ApJ, 735, 15

Garrod, R. T., Weaver, S. L. W., & Herbst, E. 2008, ApJ, 682, 283

Glassgold, A. E., & Langer, W. D. 1974, ApJ, 193, 73

Glassgold, A. E., Meijerink, R., & Najita, J. R. 2009, ApJ, 701, 142

Glavin, D. P., & Bada, J. L. 2001, Astrobiology, 1, 259

Goldsmith, P. F., Melnick, G. J., Bergin, E. A., et al. 2000, ApJ, 539, L123

Goldsmith, P. F., Liseau, R., Bell, T. A., et al. 2011, ApJ, 737, 96

Hama, T., Kuwahata, K., Watanabe, N., et al. 2012, ApJ, 757, 185

Hama, T., & Watanabe, N. 2013, Chem. Rev., 113, 8783

Hasegawa, T. I., Herbst, E., & Leukng, C. M. 1992, ApJS, 82, 167

He, J., Frank, P., & Vidali, G. 2011, Phys. Chem. Chem. Phys., 13, 15803

He, J., Gao, K., Vidali, G., Bennett, C. J., & Kaiser, R. I. 2010, ApJ, 721, 1656

He, J., Jing, D., & Vidali, G. 2014, Phys. Chem. Chem. Phys.

He, J., & Vidali, G. 2014, ApJ, 788, 50

Herbst, E., & Cuppen, H. M. 2006, Proc. Natl. Acad. Sci. U. S. A., 103, 12257

Herbst, E., & van Dishoeck, E. F. 2009, Annu. Rev. Astron. Astrophys., 47, 427

Hidaka, H., Watanabe, M., Kouchi, A., & Watanabe, N. 2011, Phys. Chem. Chem. Phys., 13, 15798

Hidaka, H., Watanabe, N., Shiraki, T., Nagaoka, A., & Kouchi, A. 2004, ApJ, 614, 1124

Hincelin, U., Wakelam, V., Hersant, F., et al. 2011, A&A, 530, A61

Hogerheijde, M. R., Bergin, E. A., Brinch, C., et al. 2011, Science, 334, 338

Hollenbach, D., Kaufman, M. J., Bergin, E. A., & Melnick, G. J. 2009, ApJ, 690, 1497

Hollenbach, D., Kaufman, M. J., Neufeld, D., Wolfire, M., & Goicoechea, J. R. 2012, ApJ, 754, 105

Hornekaer, L., Baurichter, a., Petrunin, V. V., et al. 2005, J. Chem. Phys., 122, 124701

Ioppolo, S., Cuppen, H. M., Romanzin, C., van Dishoeck, E. F., & Linnartz, H. 2008, ApJ, 686, 1474

Iqbal, W., Acharyya, K., & Herbst, E. 2012, ApJ, 751, 58

Jenkins, E. B. 2009, ApJ, 700, 1299

Jensen, A. G., Rachford, B. L., & Snow, T. P. 2005, ApJ, 619, 891

Jing, D., He, J., Bonini, M., Brucato, J. R., & Vidali, G. 2013, J. Phys. Chem. A, 117, 3009

Jing, D., He, J., Brucato, J., et al. 2011, ApJ, 741, L9

Jing, D., He, J., Brucato, J. J. R., et al. 2012, ApJ, 756, 98

Jing, D., He, J., Brucato, J. R., et al. 2014, ApJ, 780, 113

Kaiser, R. I., Eich, G., Gabrysch, A., & Roessler, K. 1999, A&A, 344, 340

Karlsson, R., Sandqvist, A., Hjalmarson, A., et al. 2013, A&A, 554, A141

Katz, N., Furman, I., Biham, O., Pirronello, V., & Vidali, G. 1999, ApJ, 522, 305

Kimmel, G. A., Stevenson, K. P., Dohnálek, Z., Smith, R. S., & Kay, B. D. 2001, J. Chem. Phys., 114, 5284

Kolasinki, K. W. 2008, Surface science : Foundations of catalysis and nanoscience (Wiley: Hoboken, N.J.)

Kristensen, L. E., & van Dishoeck, E. F. 2011, Astron. Nachrichten, 332, 475

Kuan, Y.-J., Charnley, S. B., Huang, H.-C., Tseng, W.-L., & Kisiel, Z. 2003, ApJ, 593, 848

Lamberts, T., Cuppen, H. M., Ioppolo, S., & Linnartz, H. 2013, Phys. Chem. Chem. Phys., 15, 8287

Larsson, B., Liseau, R., Pagani, L., et al. 2007, A&A, 466, 999

Le Bourlot, J., Le Petit, F., Pinto, C., Roueff, E., & Roy, F. 2012, A&A, 541, A76

Li, L., Zhao, H., Vidali, G., et al. 2010, J. Phys. Chem. A, 114, 10575

Liseau, R., Goldsmith, P. F. F., Larsson, B., et al. 2012, A&A, 541, A73

Mathis, J. S., Rumpl, W., & Nordsieck, K. H. 1977, ApJ, 217, 425

McKellar, A. 1940, Publ. Astron. Soc. Pacific, 52, 187

Melnick, G. J., Tolls, V., Goldsmith, P. F., et al. 2012, ApJ, 752, 26

Meng, B., & Weinberg, W. W. H. 1997, Surf. Sci., 374, 443

Miller, S. L. 1953, Science, 117, 528

Mispelaer, F., Theulé, P., Aouididi, H., et al. 2013, A&A, 555, A13

Miyauchi, N., Hidaka, H., Chigai, T., et al. 2008, Chem. Phys. Lett., 456, 27

Mokrane, H., Chaabouni, H., Accolla, M., et al. 2009, ApJ, 705, L195

Mottram, J. C., van Dishoeck, E. F., Schmalzl, M., et al. 2013, A&A, 558, A126

Neufeld, D. A., Lepp, S., & Melnick, G. J. 1995, ApJS, 100, 132

Neufeld, D. A., Goicoechea, J. R., Sonnentrucker, P., et al. 2010, A&A, 521, L10

Nishi, N., Shinohara, H., & Okuyama, T. 1984, J. Chem. Phys., 80, 3898

Noble, J. A., Congiu, E., Dulieu, F., & Fraser, H. J. 2012, MNRAS, 421, 768

Nordholm, S. 1985, Chem. Phys., 98, 367

Oba, Y., Miyauchi, N., Hidaka, H., et al. 2009, ApJ, 701, 464

Oba, Y., Watanabe, N., Hama, T., et al. 2012, ApJ, 749, 67

Oba, Y., Watanabe, N., Kouchi, A., Hama, T., & Pirronello, V. 2011, Phys. Chem. Chem. Phys., 13, 15792

Perets, H. B., Biham, O., Manico, G., et al. 2005, ApJ, 627, 850

Perets, H. B., Lederhendler, A., Biham, O., et al. 2007, ApJ, 661, L163

Perry, R. A. 1984, Chem. Phys. Lett., 106, 223

Pirronello, V., Biham, O., Liu, C., Shen, L., & Vidali, G. 1997a, ApJ, 483, L131

Pirronello, V., Liu, C., Roser, J. E., & Vidali, G. 1999, A&A, 344, 681

Pirronello, V., Liu, C., Shen, L., & Vidali, G. 1997b, ApJ, 475, L69

Pulliam, R. L., McGuire, B. a., & Remijan, A. J. 2012, ApJ, 751, 1

Raut, U., & Baragiola, R. a. 2011, ApJ, 737, L14

Roberts, H., & Herbst, E. 2002, A&A, 395, 233

Romanzin, C., Ioppolo, S., Cuppen, H. M., van Dishoeck, E. F., & Linnartz, H. 2011, J. Chem. Phys., 134, 084504

Roser, J. E. 2004, PhD thesis, Syracuse University, New York, USA

Roser, J. E., Vidali, G., Manicò, G., & Pirronello, V. 2001, ApJ, 555, L61

Sandford, S. A., & Walker, R. M. 1985, ApJ, 291, 838

Slevin, J. 1981, Rev. Sci. Instrum., 52, 1780

Snow, J. L., Orlova, G., Blagojevic, V., & Bohme, D. K. 2007, J. Am. Chem. Soc., 129, 9910

Snow, T. P., & McCall, B. J. 2006, Annu. Rev. Astron. Astrophys., 44, 367

Snyder, L. E., Lovas, F. J., Hollis, J. M., et al. 2005, ApJ, 619, 914

Stantcheva, T., Shematovich, V. I., & Herbst, E. 2002, A&A, 391, 1069

Stebbins, J., Huffer, C. M., & Whitford, A. E. 1939, ApJ, 90, 209

Sundaresan, S., & Kaza, K. R. 1985, Surf. Sci., 160, 103

Swings, P., & Rosenfeld, L. 1937, ApJ, 86, 483

Takano, S., Takano, T., Nakai, N., Kawaguchi, K., & Schilke, P. 2013, A&A, 552, A34

Tielens, A. A., & Hagen, W. 1982, A&A, 114, 245

Tielens, A. G. G. M. 2013, Rev. Mod. Phys., 85, 1021

Tovbin, Y. K. 1990, Prog. Surf. Sci., 34, 1

Trumpler, R. J. 1930a, Publ. Astron. Soc. Pacific, 42, pp. 214

—. 1930b, Lick Obs. Bull., 14, 154

—. 1930c, Publ. Astron. Soc. Pacific, 42, 267

van Dishoeck, E. F. 2014, Faraday Discuss., 168, 9

van Dishoeck, E. F., & Black, J. H. 1986, ApJS, 62, 109

van Dishoeck, E. F. E. F., Herbst, E., & Neufeld, D. A. D. a. 2013, Chem. Rev., 113, 9043

Vidali, G. 2013, J. Low Temp. Phys., 170, 1

Vidali, G., & Li, L. 2010, J. Phys. Condens. Matter, 22, 304012

Šurda, A., & Karasova, I. 1981, Surf. Sci., 109, 605

Ward, M. D., Hogg, I. a., & Price, S. D. 2012, MNRAS, 425, 1264

Watanabe, N., & Kouchi, A. 2002, ApJ, 571, 173

—. 2008, Prog. Surf. Sci., 83, 439

Westphal, A. J., Stroud, R. M., Bechtel, H. A., et al. 2014, Science, 345, 786

Whittet, D. C. B. 2010, ApJ, 710, 1009

Williams, D. a. 2005, J. Phys. Conf. Ser., 6, 1

Xie, H.-b., Ding, Y.-h., & Sun, C.-c. 2006, ApJ, 3, 573

Yates, J. T. 1985, The Thermal Desorption of Adsorbed Species, ed. R. Park, Vol. 22 (New York: Academic Press), 425

Yıldız, U. A., Acharyya, K., Goldsmith, P. F., et al. 2013, A&A, 558, A58

Zahid, H. J., Geller, M. J., Kewley, L. J., et al. 2013, ApJ, 771, L19

Zheng, W., & Kaiser, R. I. 2010, J. Phys. Chem. A, 114, 5251

Zubkov, T., Smith, R. S., Engstrom, T. R., & Kay, B. D. 2007, J. Chem. Phys., 127, 184707

VITA

I was born on July 30th, 1987 in a small village of Hunan province in China, and spent the first 18 years of my life in Hunan. In 2005, I went to college in Nanjing University, where I studied physics as my major. Four years later, I was offered a scholarship to study abroad in the United States in Syracuse University as a graduate student of physics. In 2014, I defended my PhD thesis and now I am working at University of Hawaii at Manoa, Chemistry Department as a postdoctoral researcher.